2015

Isolation, Culture, Differentiation of Cells and Biomolecule Detection in Microfluidics

Bu Wang
Lehigh University

Isolation, Culture, Differentiation of Cells and Biomolecule Detection in Microfluidics

by

Bu Wang

Presented to the Graduate and Research Committee

of Lehigh University

in Candidacy for the Degree of

Doctor of Philosophy

in

Materials Science and Engineering

Lehigh University

May, 2015

Approved and recommended for acceptance as a dissertation in partial fulfillment of the requirements for the degree of Doctor of Philosophy.

Student: Bu Wang

Dissertation Title: Isolation, Culture, Differentiation of Cells and Biomolecule Detection in Microfluidics

_____

Date

_____

Xuanhong Cheng, Dissertation Director, Chair

_____

Accepted Date

Committee Members:

_____

James Gilchrist

_____

Sabrina Jedlicka

_____

Daniel Ou-Yang

_____

Xiaohui (Frank) Zhang

Acknowledgement

Thesis Committee

Prof. Xuanhong Cheng: For inspiring creativity, critical thinking and hard work that I needed to fully develop as an independent capable researcher. Also for the continual support of my research and belief in my capability during various challenges.

Prof. Sabrina Jedlicka: For mentoring in the Neural Stem Cell research and teaching me to better utilize resources for research.

Prof. James Gilchrist: For guidance in the Cell Capture research, Molecular Detection research and numerous summer projects. Also for advice and guidance that led me into academic research.

Prof. Ou-Yang: For generously allowing me to work in his lab, sharing his knowledge of optical Physics in Molecular Detection research and advice on job hunting.

Prof. Xiaohui (Frank) Zhang: For generously sharing his knowledge of BioEngineering and advice on carrying research projects to completion.

Collaborators and Mentors

Dr. Susan Perry, Dr. Alexander Weldon, Dr. Pisist Kumnorkaew, Dr. Steven Ming-Tzo Wei, Dr. Jinxin Fu, Emily Geishecker and Meghan Casey: For generously sharing knowledge of their area of expertise.

Family and Friends

Yarong Dong and Dr. Chuan Wang: My amazing family who have been encouraging and supporting me to always be curious, to push boundaries without fear and to explore with hope.

Anthony Reinen: For being my rock and my lighthouse.

Dr. Yihe Huang, Dr. Zhichao Hu, Xue Xia, Dr. Yi Hu, Ivania Figueroa and Dr. Peng Cheng: For inspiring discussions, brilliant new ideas and being the friends I could ever ask for.

I dedicate this dissertation, and my future career, to bringing health to those in need.

Contents

List of Figures

List of Tables

Abstract

In recent years, microfluidics has been developed into a great tool for research and practical applications. Microfluidic systems are usually tens to hundreds of microns in size, enabling small volumes fluids handling. It has been applied in many disciplines, including chemistry, biology and medicine. Many advantages of microfluidics stem directly from the reduction in size and also the ability to integrate with microsensors and microactuators. The advantages include low reagent and sample volumes, compatibility with highly parallel experiments, ability to better simulate the natural physiology environment, ability to isolate factors of the cellular microenvironment and to spatially and temporally control individual experimental parameter, and low cost.

This dissertation focuses on developing and optimizing appropriate microfluidics for *in vitro* cell analysis system with patient's body fluids as input and information on patient's health state as output. The steps include isolating cells of interest from patient's sample, maintaining cell culture, differentiating cells and analyzing the molecules secreted by cells. This dissertation has achieved 1) enhancement of cell isolation efficiency of Jurkat cells by creating nanotopography in flatbed immunoaffinity microfluidics; 2) systematically developed maintenance and differentiation protocols in microfluidics for C17.2 NSCs; and 3) enhanced immunoaffinity detection of cell secretion molecules using

biotin as a model by introducing a combination of thermophoresis and convection induced by a mild temperature gradient in microfluidics.

With successful demonstration and optimization of these microfluidic functions, it is hoped an easy, portable, low cost POC (point of care) microfluidic system can be developed and made available for health monitoring and/or disease diagnostics.

Chapter 1

Introduction

1.1 Introduction to *In Vitro* Cell Analysis

Cells, as the basic structural, functional, and biological building block of a human body, carry tremendous information on the genetic make-up, the health and metabolic state of the individual it is taken from. *In vivo* cell analysis offers the advantage of direct observation of cells in their physiological environment, but can be very challenging to implement. On the other hand *in vitro* studies often need careful extrapolation of data to relate back to the state of the individual, but it has the advantage to isolate cells from their complex environment and study cellular responses to the individual components.

In vitro cell analysis can also be done on the whole cell level, the organelle level and the molecular level. Analysis on the whole cell level monitors the physical, thermal, electrical, mechanical and optical properties of individual cells and whole cell activities such as ion currents in and out of the cell membrane, [1] cell migration, [2] and cell division. [3] Organelles in each cell have vital functions, the analysis of which is also important. For example, energy production from mitochondria mediates apoptosis, [4] the proper function of Golgi complex and the caveolae membrane system are essential for endocytosis and

exocytosis, [5] and centrioles regulates spatial arrangement of the cellular structures and cell. [6] *In vitro* cell analysis can also be done on the molecular level. In this case, proteins, DNA, RNA and small molecules such as metabolites are isolated from the cells and detected biochemically: for example, co-immunoprecipitation, protein affinity purification, western blotting and two hybrid screening are methods often used in protein analysis; sequencing, hybridization and PCR (polymerase chain reaction) are commonly used for identification of nucleic acids; small molecules such sugar, ions, amino acids, peptides and superoxides are analyzed by corresponding assays centering around the analytes' chemical and physical properties.

The information from *in vitro* cell analysis not only provide fundamental understanding of cell biology, but also frequently used for disease prognosis, diagnosis and monitoring. For example, *in vitro* analysis to characterize T-helper type I cells and inflammatory macrophages in transgenic mice after experimental autoimmune encephalomyelitis revealed that the perceived central role for Interleukin -12 in autoimmune inflammation has been misinterpreted and that Interleukin -23, and not Interleukin -12, is the critical factor in this response. [7] *In vitro* analysis of peptide and peptide receptor expression of cells has been extensively documented and used as targets for cancer diagnostics over the

year. Examples include vascular somatostatin receptors for human colonic carcinomas; VIP/PACAP receptors for lung, stomach, colon, rectum, breast, prostate, pancreatic ducts, liver, and urinary bladder cancer; and Bombesin and GRP peptides for gastrointestinal tract, lung, prostate, and breast cancer. [8] After isolation from patient's blood, T cells can be analyzed, activated and expanded *in vitro* before being re-injected into the patient. T cells with this type of *in vitro* treatment have potent antitumor effects and can establish memory in patients with advanced leukemia, indicating its potentially significant role in cancer therapeutics. [9]

1.2 Overview of Cell Isolation in Microfluidics

Microfluidics is a powerful research tool with practical applications that emphasize the design of systems on micron scale in which small volumes of fluids will be handled. It has been applied in many disciplines, including chemistry, biology and medicine. [10–14] Microfluidics offers many significant advantages in biological studies, stemming directly from the reduction in size. The advantages include low reagent and sample volumes, compatibility with highly parallel experiments, ability to better simulate the natural physiology environment, ability to isolate factors of the cellular microenvironment and to precisely control individual experimental parameter, and low cost.

Isolating cells of interest from biological sample is a major step for *in vitro* analysis. It can be achieved using physical or biochemical methods. Biochemical methods rely on surface protein expression while physical methods utilize properties such as cell size, density, and migration behavior. Biochemical methods are specific while physical methods are able to isolate cell populations to study without prior knowledge of the biomarkers. Traditional methods often have limitations that can be compensated by microfluidics: inadequate separation by gradient centrifugation can be eliminated by the precise streamline control offered by laminar flow in microfluidics; mixed cell population from adhesion separation can be further separated by fine tuning chemical and physical properties in microfluidics; expensive and labor-intensive methods, such as FACS (fluorescence-activated cell sorting) can incorporated into microfluidics that is low cost and requires minimal handling. Here an overview of current methods is provided.

Biochemical methods: Immunoaffinity cell capture relies on antibody-antigen reaction between cellular surface and the capture substrate, which gives it the advantage of high specificity and high purity of cells captured. [15] The disadvantage is this capture process is often irreversible. The configurations frequently used in this methods are: flatbed and bead-based microfluidics.

Flatbed immunoaffinity capture: Cells can be isolated on flatbed microfluidic devices coated with the corresponding antibody for its expressed surface proteins. [16] Adding structural features including nanobeads, nanofibers and nanopillars can significantly increase the capture efficiency of the flatbed devices.[17–19]

Bead-based immunoaffinity capture: Superparamagnetic polystyrene spherical beads coated with antibody can be mixed with cell samples in a solution. Once the beads adhere to the cells of interest, they can be pulled down by magnetic field while the unattached cells can be washed off. [20]

Physical methods: Cells can be isolated according to their physical properties such as size, dielectric property, their refractive index and their intrinsic magnetic properties. These methods have the advantages of minimal requirement on knowledge of biomarker expression and the ability to release cells reversibly for further analysis while bare the disadvantage of non-specificity.

Size-based capture: Size-based cell capture isolates cells according to their physical dimension, which gives it the disadvantage of nonspecificity, but it can be useful in isolating uncharacterized cells with no prior knowledge of their biochemical characteristics. This is particularly useful in the case of blood cell isolation, given the size

of white blood cells, red blood cells and plasma content are drastically different. A microfluidics with a continuous flow diffusive filter has been designed for depletion of leukocytes from blood with >97% leukapheresis rate, providing a cheaper faster alternative to centrifugation and fiber mesh filtration. [21]

Flow-based capture: Flow-based cell capture takes advantage of the low Reynolds number fluid flow associated with the imposition of certain geometries or parallel fluid flows of different flow rates to passively sort or segregate target cells. [22] This method sorts cells by their physical dimension and is non-specific. For example, spiral microfluidic devices can be used to sort cells according to their sizes. The inertial forces coupled with the Dean rotational force due to the curvilinear microchannel geometry cause cells to occupy a single equilibrium position near the inner microchannel wall. The position at which cells equilibrate is dependent on the ratio of the inertial lift to Dean drag forces, therefore cells of different sizes will accumulate at specific locations at the outlet. [23]

Cell sorting based on other properties of cells can also be achieved, such as Dielectrophoresis-based isolation, [24] optical tweezer isolation [25] and native magnetic properties-based sorting. [26] These methods do not often require immune labeling of the

cells, but rely on physical properties of cells such as their dielectric property when subjected to a non-uniform electric field, their refractive index and their intrinsic magnetic properties.

1.3 Overview of Cell Culture and Cell Differentiation in Microfluidics

Traditional cell culture and cell differentiation are often carried out in flat-surface petri dishes or cell culture flasks that suffer from non-uniformity of surface properties, inhomogeneity of chemical compositions in media, lack of 3D structures that mimic the physiological environment and lack of temporal control. Microfluidics are used to provide more precise spatial and temporal control of the physical and biochemical environments around cells. The resulting cell responses shed light about fundamental cell biology in healthy and pathological states. On the physical control front, shear stress, tensile stress, substrate stiffness, and fiber alignment are all parameters of interest. For example, microfluidic devices with a low shear rate cyclic flow that mimics the mechanical, structural, absorptive, and transport properties of the human gut has been developed for transport, absorption, and toxicity studies, giving great value for drug testing as well as development of novel intestinal disease model. [27] Computer integrated air-liquid two-phase microfluidic systems have been developed to enable on-chip

engineering of human airway epithelia and precise reproduction of physiologic or pathologic liquid plug flows found in the respiratory system to study cellular-level lung injury under flow conditions that cause symptoms characteristic of a wide range of pulmonary diseases. [28] Other than shear stress, substrate stiffness is also an effective tool for regulating cell behaviors such as locomotion, proliferation and differentiation. Microfluidics with polydimethylsiloxane (PDMS) stiffness gradients have been created to study osteogenic differentiation of rat mesenchymal stem cells to develop better implant materials and tissue engineering scaffolds. [29]

Chemical environment also plays a significant role in regulating biological and pathological processes, such as chemotaxis and embryogenesis can be easily manipulated in microfluidics to study cell growth, differentiation, migration, and apoptosis. [30] Microfluidics with stable and well-defined conflicting gradients of IL-8 and LTB4 have been used to staudy neutrophil chemotaxis. [31] Multiplexing of simultaneous chemical stimulation can be readily achieved using microfluidics: a continuous gradient of a growth factor (GF) mixture containing epidermal growth factor (EGF), fibroblast growth factor 2 (FGF2) and platelet-derived growth factor (PDGF) has been generated by continuous flow in microfluidics to study the differentiation of human NSCs (hNSCs)

from the developing cerebral cortex into astrocytes offering guidance for a wide range of basic and applied studies on human NSCs. [32] Temporal chemical gradient can also be easily manipulated in microfluidics: a microfluidic device that mimics the exponential clearance curve of chemicals in the human body has been used to study the toxicant response of fibroblast cells. [33]

While microfluidic cell culture offers advantages such as flexibility in the design of microfluidic devices, the ability to more closely mimic a cell's natural microenvironment, parallelization, on-chip analysis or direct coupling to downstream analytical chemistry platforms, low reagent consumption and low cost, transferring our knowledge of macroscopic cell culture to microfluidic cell culture requires careful examination. Changes in device material, surface coating, and cell number per unit surface area or per unit media volume may all affect the outcome of otherwise standard protocols. [34] Parameters of long standing research interest include, but not limited to surface treatment (UV, oxygen plasma), [35] surface cell adhesion molecule coating, [36] oxygen transport, [34] osmolarity, [37] pH, [37] nutrient consumption and medium turnover rate. [38,39] Current research methods often involve adjusting the culture parameters in microfluidic and

compare cellular behavior as such migration, viability, metabolic state and toxicity status to those in macroscopic culture. [34]

Stem cell differentiation is essential for the development of any organism. It also occurs in adulthood as adult stem cells divide and create fully differentiated daughter cells during tissue repair and during normal cell turnover. It is an area of active research, in which microfluidics finds itself particularly useful due to its precise control of the microenvironment.

Stem cell differentiation can be initiated by many physical and chemical compositions of the microenvironment, including shear stress, surface structure, growth factor concentration and exposure to cytokine, all of which are controllable in microfluidic devices with spatial and temporal resolution mimicking in vivo environment. Kapur *et al.* analyzed the role of several signaling pathways in the fluid flow shear stress-induced proliferation and differentiation of normal human osteoblasts. [40] Chung *et al.* cultured human neural stem cells from the developing cerebral cortex in a microfluidic device constantly generating a gradient of a growth factor mixture containing epidermal growth factor (EGF), fibroblast growth factor 2 (FGF2) and platelet-derived growth factor (PDGF) to show graded differentiation results proportional to growth factor

concentration.[32] Park *et al.* cultured neural progenitors derived from human embryonic stem cells in a microfluidic system generating continuous cytokine gradients (sonic hedgehog, fibroblast growth factor 8, and bone morphogenetic protein 4) to show opposing effects of agonist (sonic hedgehog) and antagonist (bone morphogenetic protein 4) on neural differentiation.[41] Yim *et al.* used both retinoic acid and PDMS nanotypography to study the differentiation of human mesenchymal stem cells into neural lineage. [42] They found a combination of nanotopography and biochemical cues such as retinoic acid further enhanced the upregulation of neural marker expressions, but nanotopography showed a stronger effect compared to retinoic acid alone on unpatterned surface. [42] Yang *et al.* cultured C17.2 mouse neural stem cells on electrospinned nano/micro scale poly(l-lactic acid) aligned fibers. [43] They were able to align the direction of cell elongation and its neurite outgrowth to the direction of PLLA fibers. They also found out the rate of neural differentiation was higher for PLLA nanofibers than that of micro fibers and it was independent of the fiber alignment. [43]

1.4 Detection of Cell Secretion

Cells secret many protein molecules including regulatory molecules such as hormones and neurotransmitters, digestive enzymes, antibodies, mucus and structural proteins such

as collagen. The secretome profile is often assayed to interrogate cell function. Popular detection methods based on the signal they analyze are introduced here.

Fluorescence detection: Fluorescent material emits light upon absorbing light of a shorter wavelength and higher energy. The major advantage of fluorescence detection is simplicity and high sensitivity, while potential pH sensitivity and susceptibility to photobleaching over time are their disadvantages. [44] Adapting traditional fluorescence detection methods such as ELISA (enzyme-linked immunosorbent assay) and FACS (fluorescence-activated cell sorting) in microfluidics help to enhance their capability by lowering sample volume requirement, enhancing detection sensitivity, eliminating expensive equipment and lengthy procedures, and enabling real-time detection. It has been shown the amount of fluorescence protein expression in single *E. coli* cells can be quantitatively measured using droplet microfluidics. [45] With the development of brighter and more stable fluorescent labeling such as quantum dots and more sophisticated method such as FRET (Förster resonance energy transfer), even real-time analysis of single molecule can be realized. [46]

Chemiluminescence detection: This method relies on the emission of energy in the form of light (with limited emission of heat) as the result of a chemical reaction. It requires no

excitation instrumentation, even though emission is generally low. [44] Traditional methods suffer from poor detection sensitivity due to low emission; on the other hand, microfluidics offers a more stable environment and therefore a lower background noise, which helps to improve the detection sensitivity. [47] Applications include detection of human serum albumin or immunosuppressive acidic protein as a cancer marker in human serum for cancer diagnostics, [48] allergen screening and near-patient diagnostic immunoassays. [49]

Surface plasmon resonance (SPR): SPR is capable of real-time highly sensitive label-free analysis of mass change in close proximity. It relies on the change in resonant oscillation of conduction electrons brought by mass change at the interface between a negative and positive permittivity material stimulated by incident light. Due to the high sensitivity and close proximity of SPR, integration with microfluidics greatly enhances its performance by providing a precisely controlled environment with minimal fluctuations. Performance immunoassays include IgG, [50] cardiac marker B-type natriuretic peptide, [51] porcine circovirus type 2 [52] and interleukin-8 analysis, [53] just to name a few.

Resonance-frequency mass sensing: Cantilevers and quartz crystal micro-balance are two techniques relying on a change in resonant frequency to detect a mass change. It offers

high sensitivity, high specificity and simplicity to operate. However, traditional bulk methods are difficult to implement in fluidics due to damping, viscosity effects and thermal fluctuations, [44] which can be minimized in microfluidics.

Conductance detection: Nanowires can be used to detect molecular binding on its surface that changes the wire's conductance. The small dimension of this method limits its use to small scale studies such as in microfluidic. They offer the advantage of low volumes, real-time sensing, a very high sensitivity and great multiplexing capability. [54] However, their complicated fabrication and patterning procedures and requirement for electronic components makes them a rather expensive choice.

Label-free detection methods capable of direct quantification of the analyte without labels eliminates the need for tags, dyes or specialized reagents or engineered cells, reducing the resources and procedures required for assay development and minimizing liabilities created by the use of labels. Primary labels can be added to the analyte to assist detection. Adding label offers the advantages of high sensitity, specificity and ability to simultaneously analyze multiple cellular properties by different tags. Commonly used labels can be fluorescent, colorimetric or radioactive. A signal amplification step can be added to the labeling process by introducing a sandwiched assay: primary labels specific

to the analyte are added to surface immobilized analyte of unknown concentration, then a secondary label that detects the primary label is used to quantify the amount of primary tags which in turn quantifies the amount of analyte. The secondary labels can be tagged with fluorescence, colors or radioactive isotopes themselves or they can trigger reactions that produce signals such as chemiluminescence, wavelength shift or color intensity change. The advantages of using a sandwiched assay are ability to simultaneously detect different analyte in multiple-target assays and increased detection sensitivity from signal amplification. A summary of detection methods and the number of labels they often use is listed here.

Table 1.1: Popular detection methods and the number of labels often used

Popular detection methods	Number of labels often used
Fluorescence detection	1, 2
Chemiluminescence detection	0, 1, 2
Surface plasmon resonance	0, 1
Resonance-frequency mass sensing	0, 1
Conductance detection	0

1.5 Summary

In this dissertation, research will be conducted in areas of *in vitro* isolation, culture, differentiation of cells and biomolecule detection in microfluidics. The aims for each chapter are 1) providing background in each area; 2) enhancing cell isolation efficiency by creating nanotopography in flatbed immunoaffinity microfluidics using Jurkat model system; 3) systematically developing maintenance and differentiation protocols in microfluidics using C17.2 NSCs; 4) enhancing immunoaffinity detection by introducing a mild temperature gradient directly above the affinity substrate and 5) providing a summary of goals achieved and future outlooks.

Chapter 2

Jurkat Cell Capture in Microfluidics with Surface Nanotopography [55]

2.1 Movitation

Microfluidic cell isolation devices have recently found applications in tissue engineering, [56,57] clinical diagnosis, [58,59] and fundamental cell biology. [60,61] Immunoaffinity isolation based on specific cell surface markers attracts special attention due to its capability to distinguish cell types of similar physical properties in complex samples, for example human blood. [58,62,63] Its ease of use makes it a good candidate for point of care settings. Immunoaffinity cell capture generally takes one of two forms: target cells attach to either suspended magnetic beads, [64] or interior surfaces of a microfluidic chip. [65] Cell-antibody interactions are more accurately controlled in the latter strategy and as such it yields higher capture efficiency and purity of target cells. [58] Toner's group has designed immunoaffinity microfluidics for reliable isolation of circulating cells at concentrations as low as 5 cells/mL from whole blood with average purity higher than 50%, [58,63] which exceeds the performance of commercially available magnetic bead-based assays. These

microchips have been shown to diagnose cancer, [58] infection, [66] and inflammatory diseases [62] with minimal sample handling.

To enhance cell interactions with antibody-functionalized device walls, several groups have employed capture beds with nanotopography. Wang *et al.* fabricated nanopillars to enhance contact frequency and duration of circulating tumor cells with functionalized substrates and increased capture yield by greater than 40%. [17] The King group deposited nanobeads and nanofibers in capillary channels to isolate stem cells and tumor cells. [18,19] Capture yield increased by up to 100% in deposited versus smooth capillaries. While these studies suggest a positive effect of nanotopography on cell capture, nanopatterns studied contain either a single geometry or random structures that do not elucidate detailed relations between the two. In a separate study, Tuttle *et al.* immobilized antibodies on surface-bound nanobeads 40 to 860nm in diameter and tested their functionality by capturing antigen coated fluorescent microspheres. [67] Specific capture increased continuously with the nanobead size. The results were suggested to stem from greater amounts of immobilized antibodies and an enhancement of collective antibody functionality on rough surfaces. Additionally, the Santore group investigated affinity between microbeads and patched charge capture surfaces with varying overall charge

density and patch size. [68–70] Although these studies explored a variety of nanostructured geometries, the interaction of microbeads with rough or patterned surfaces may not translate fully to that of the cells. Built on these previous findings, in this study we carefully controlled surface nanotopography over a greater range than that previously explored and studied its influence on immunoaffinity capture of lymphocytes.

To create surfaces with reproducible and uniform nanotopography we modified smooth glass substrates by the addition of a monolayer of close-packed, uniform-sized, silica nano-beads 100 to 1150 nm in diameter. These surfaces were incorporated as the base of microfluidic channels then functionalized with CD4 antibodies in order to capture CD4+ cells from human lymphocyte culture under continuous flow. In addition to depositing nanobeads with varying diameters, numerous flow rates and altered cell mechanical properties were evaluated in order to explore the mechanisms behind cell interactions with rough functionalized substrates.

2.2 Materials and Methods

2.2.1 Preparation of Silica Nanobeads

The particles used in this studying have diameters between 100 and 1150 nm to cover the size range reported in the literature for cell capture enhancement. Silica particles within

this size range also forms stable suspensions compatible with the convective deposition process. We refer to the spheres used in this study as nanoparticles in this paper, and they are sometimes also referred to as colloidal particles and microspheres in the literature. Nanospheres 100 nm, 460 nm, and 490 nm in diameter were prepared through hydrolysis of TEOS in 200 proof ethanol with 0.2 M TEOS, 17.0 M DI water, and 0.2, 1.2, and 1.6 M NH_3 respectively. [71] 309 nm particles were prepared through similar hydrolysis of TEOS in 190 proof ethanol with 0.04 M TEOS and 2.45 M NH_3. [72] 319 nm particles were prepared with 200 proof EtOH with 0.13 M TEOS, 18.9 M DI H_2O, and 1.6 M NH_3. [72] Particles 407 nm in diameter were prepared in 190 proof ethanol with 0.29 M TEOS, 6 M DI water, and 1.9 M NH_3. [73] In all cases NH_4OH, DI water (when applicable) and ethanol were mixed initially. TEOS and ethanol, also pre-mixed, were added to the ammonia solution to start the particle synthesis reaction. Note that DI H_2O was not a unique component in some recipes—NH_4OH is NH_3 in H_2O (29% NH_3 on average and used as received).

While the upper limit of synthesizable particles through batch reactions is around 500 nm, larger particles were made by a core-shell type approach. The first method was a continuous core-shell synthesis process in which seeds were first prepared by the addition

of 1 mL TEOS and 4 mL 200 proof ethanol to 46 mL 200 proof ethanol and 9.0 mL NH_4OH (29%). After two hours an additional 5 mL TEOS/20 mL ethanol solution was fed continuously at 0.1 ml/min to yield 700nm SiO_2 microspheres. [72] In a separate semi-batch process, 500 nm seeds were grown to 928 and 1150 nm in diameters. Here hydrolysis similar to the batch processes presented earlier was carried out as 4.25 g TEOS ([TEOS] = 0.2 M) and 35.88 g 200 proof EtOH were added to 13.63 g EtOH, 24.88 g DI H_2O ([DI H_2O] = 17.0 M), 7.03 g NH_4OH ([NH_3] = 1.2 M), and 300 µl 500nm SiO_2/EtOH (46% v/v). [71] This yielded 928 nm SiO_2 microspheres. An additional 4.25 g TEOS in 35.88 g EtOH added one day later formed an additional shell atop the 928 nm SiO_2 microspheres and brought the final diameter to 1150 nm.

All experiments were carried out at room temperature in sealed vessels under moderate stirring. Post-synthesis, the particles were centrifuged and washed with ethanol and DI H_2O a minimum of three times each. Centrifugation times were based on the terminal particle settling velocity in order to remove both excess reagents and any smaller secondary constituents formed as byproducts in our reactions. For deposition, particles were suspended in DI H_2O and brought to an appropriate volume fraction based on their size (see **Table 2.1**). Note that changes in chemical suppliers and product lots from those

suppliers yielded small size variations in particles synthesized. However, with consistent reagents particle growth was highly linear and scalable.

Table 2.1: Concentration and optimal deposition speed of nanobeads used in this study

Size of silica beads (±1 SD)	Concentration (v/v in DI-water)	Optimal speed
100 ± 10nm	12.84%	3 μm/s
309 ± 30nm	12.84%	6 μm/s
319 ± 17nm	11.80%	33 μm/s
407 ± 23nm	10.84%	10 μm/s
460 ± 20nm	26.50%	21 μm/s
490 ± 20nm	25.90%	58 μm/s
700 ± 24nm	32.40%	17 μm/s
928 ± 16nm	15.20%	42 μm/s
1150 ± 24nm	12.50%	67 μm/s

2.2.2 Preparation of Close-Packed Silica-Nanobead Substrates

Close-packed silica-nanobead substrates were prepared through convective deposition following the method reported by Kumnorkaew. [74] Plain glass microslides were used as deposition blades and substrates. Deposition substrates were cleaned in piranha solution (sulfuric acid and hydrogen peroxide at 3:1 volume ratio) for over 1 hour, thoroughly

rinsed with deionized (DI) water and then stored in DI water until needed. The ends of the deposition blades were hydrophobically treated by coating with parafilm.

A schematic of the convective deposition setup is shown in **Figure 2.1**. The deposition blade angle was positioned at 45 degrees above the substrate as calibrated with a digital camera. Ten microliters of SiO_2/DI H_2O suspension was injected between the substrate and blade with a micropipette. The substrate was then linearly translated at the appropriate speed, as governed by specific suspension evaporative flux, for monolayer deposition.

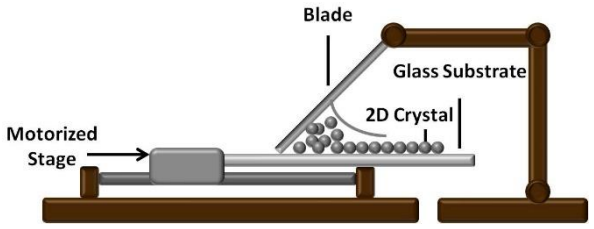

Figure 2.1: Experimental setup for nanobead deposition. Silica nanobeads from 100 to 1150 nm in diameter, synthesized through TEOS hydrolysis, were deposited into close-packed monolayers to control substrate nanotopography. A linear motor was used to translate the substrate. The hydrophobically-treated glass blade was positioned at a 45 degree angle with respect to the substrate and 10 µL SiO_2 nanobead/DI H_2O suspension was pipetted into the space between. The beads packed into a 2D crystals as the bulk suspension dragged across the glass substrate and the solvent (DI H_2O) evaporated.

Reprinted with permission from *Effect of Surface Nanotopography on Immunoaffinity Cell Capture in Microfluidic Devices*. [55] Copyright (2011) American Chemical Society.

Substrates covered with a smooth layer of TEOS were prepared as a control with identical surface chemistry but minimal roughness (root mean squared surface roughness < 2.0 nm). Clean glass sides (root mean squared surface roughness < 3.0 nm) were soaked in an ethanol solution with TEOS for 15 minutes. Subsequently the slides were thoroughly washed with ethanol and blown dry with nitrogen.

2.2.3 Device Preparation

The nanoparticle-coated substrates were patterned in a 3 mm x 3 mm square region for cell capture. Beads outside the square capture region were removed with a clean room adhesive tape. A microchannel was then bonded atop the substrate to enclose both the nanosphere pattern and a bare glass control region.

Polydimethylsiloxane (PDMS) microchannels were prepared by pouring a 10:1 mixture of silicone elastomer base and silicone elastomer curing agent onto an SU8 mold patterned on a silicon wafer. Simple straight channels with dimensions 14 mm x 4 mm x 50 μm (L x W x H) were fabricated. PDMS was degassed and cured at 70 ℃ and the microdevices were cut out. Fluid inlets and outlets were drilled using a syringe needle.

Nanobead-deposited substrates and microchannels were activated by oxygen plasma, then carefully aligned and heated for 5-10 minutes at 70 ℃ to produce permanent bonding. An image of a typical assembled device is presented in **Figure 2.2**.

After assembly the interior walls of the device, including the nanobead-deposited area and a bare glass region, were functionalized using a previously published method. [66] A 4% (v/v) solution of 3-mercaptopropyl trimethoxysilane in ethanol was injected into the device and allowed to incubate for 1hr at room temperature. Next the device was incubated with 0.01 μmol/ml GMBS in ethanol for 1 hour at room temperature. NeutrAvidin was then immobilized to GMBS by incubating chamber surfaces with a 10 μg/ml NeutrAvidin solution in PBS (phosphate buffered saline) for at least 1 hour at 4 °C. Finally, 10 μg/ml of biotinylated antibody solution in PBS containing 1% (w/v) BSA was injected to react at room temperature for at least 15 minutes before cell capture experiments were performed.

2.2.4 Cell Culture and Live Cell Capture

Jurkat cells (human lymphocytes) were maintained following the ATCC protocol at a cell concentration of 10^5 cells/mL to 10^6 cells/mL using RPMI-1640 media supplemented with 10%(v/v) FBS and 1%(v/v) pen-strep. Cells were centrifuged and resuspended at

10^6 cells/mL in culture media prior to cell capture experiments. Cell suspension was delivered into the device using a syringe pump at constant flow rates of 2μL/min, 5μL/min, or 8μL/min for 15 minutes. These flow rates are within the optimal window for CD4+ T cell capture, as found in prior work. [66] The sample injection time was chosen to ensure that target cells were not depleted from the suspension prior to reaching the downstream capture area. The numbers of cells captured in the patterned and bare glass regions in a given channel (**Figure 2.2**, Device 1) were counted using a bright field microscope. The counts on bare glass served as an internal control to account for slight batch to batch variations in testing conditions.

As bare glass slides have slightly different chemistry versus silica beads synthesized by TEOS hydrolysis, [75] we also prepared smooth TEOS coatings on glass substrates as samples with minimal roughness (Device 2). The normalized cell capture efficiency, η, were obtained by taking the ratio of cell counts on silica beads versus that on smooth TEOS coatings using the following formula:

$$\eta(R) = \frac{n_{nb}(D)}{n_{bg1}} \times \frac{n_{bg2}}{n_{TEOS}}$$

where $n_{nb}(D)$ is the number of cells captured on nanobeads in the patterned region in Device 1, n_{bg1} and n_{bg2} are counts of cells captured on bare glass region within Device 1

and Device 2 respectively, and n_{TEOS} is the cell count from smooth TEOS-treated regions in Device 2.

2.2.5 Capture of Fixed Cells

In order to test cells with altered mechanical properties, cells were centrifuged and re-suspended in 1% glutaraldehyde in PBS (v/v) for 30 min. This glutaraldehyde fixation process crosslinks proteins in the cell membrane and thus increases its modulus. The fixed cells were centrifuged, washed in PBS, and then resuspended in culture media at a concentration of 10^6 cells/mL for capture. In a separate experiment, Jurkat cells were fixed with 1% glutaraldehyde in PBS for 30 min and then stained with Hoechst 33258 (0.5mg/ml in PBS) for 10min. After rinsing, the fixed and stained cells were mixed with untreated live Jurkat cells at a 1:1 ratio in culture media with a total cell concentration of 10^6 cells/mL. This cell mixture was also used for cell capture at selected bead size and flow rates. To test if glutaraldehyde fixation affected antibody-antigen binding, the same cell mixture was used for capture experiments in microchannels bonded to antibody functionalized bare glass. The number of each cell type captured within the same imaging areas was counted and the two quantities compared.

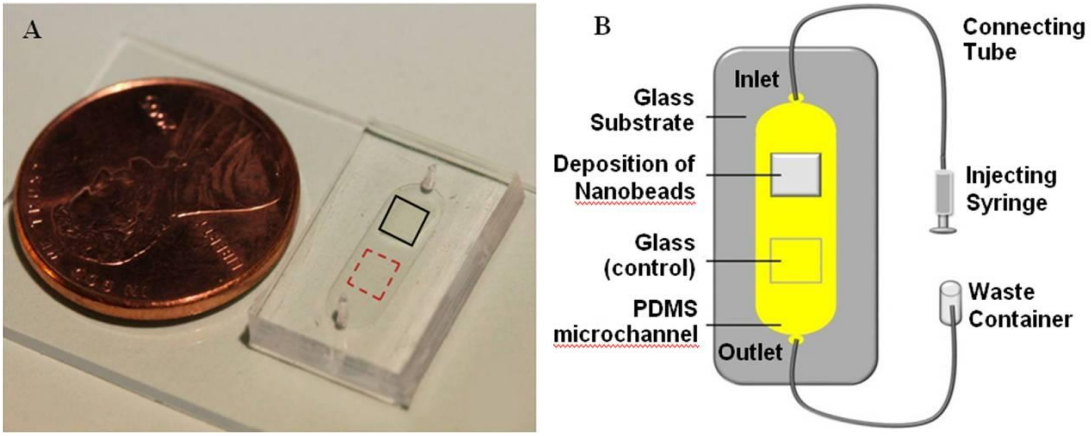

Figure 2.2: The cell capture microchip used in this study. *(A)* Photograph of a microchannel formed by oxygen plasma activation and bonding of PDMS, with an imprinted microchannel, to the glass substrate, with nanoparticle-patterned and bare glass regions. The deposited nanobead pattern (cloudy region in the black square) and a control region of bare glass (red dashed square) were enclosed in the same microchannel. The entire substrate was further functionalized with a CD4 antibody for CD4+ T cell capture from Jurkat cell cultures. *(B)* A schematic showing nanobead-covered and control glass regions within the same channel. Reprinted with permission from *Effect of Surface Nanotopography on Immunoaffinity Cell Capture in Microfluidic Devices*. [55] Copyright (2011) American Chemical Society.

2.2.6 COMSOL Simulation

Flow above a layer of close-packed beads was simulated in COMSOL Multiphysics 4.0(COMSOL Inc., Burlington, MA). Assuming a 2D crystal structure, we carry out the

simulation within a periodic cell of a hexagonal array of 1 μm spheres. A constant velocity is imposed on the layer three particle diameters from the substrate in order to investigate the near-field disturbance. The fluid is Newtonian and a volumetric flow rate of 2 μL/min renders a very small Reynold's number (Re << 1). Therefore flow near the walls is self-similar and scales with bead size.

2.2.7 Imaging and Statistical Analysis

Antibody immobilized cells on smooth glass substrate were imaged using a confocal laser scanning microscope (Visitech international, model VTeye). The cells were stained by 0.16 mM Rhodamine B in the normal culture media for 10 minutes and imaged without further washing. The z-stack images were taken using 100x magnification and expressed as a 3D image with ImageJ.

AFM measurements were carried out on a Nanoscale V AFM in tapping mode to characterize 100, 490, and 1150 nm individual particle roughnesses as well as the roughness of TEOS-coated and bare glass. Gwyddion was used for data analysis and visualization. Individual particle roughness values are documented as Root Mean Squared (RMS) Roughness. SEM measurements were performed on all nanobead depositions with Iridium coating using a Hitachi 4300 instrument (Japan). The diameter

and packing of nanobeads are documented in the images.

All cell captured experiments were repeated in at least 5 independent devices, except for Figure 7, where the experiments were repeated in at least 3 independent devices. The data were analyzed using two-tailed t tests. Two *p* values were calculated for the data points presented in **Figure 2.4**, **Figure 2.6** and **Figure 2.7**: one from comparing the cell capture on nanobead surfaces to that on TEOS under the same flow rate; the other by comparing the cell capture on a particular sized nanobead surface to its neighboring data point of a smaller nanobead diameter. When the *p* value between two data points was less than 0.1, their difference was considered statistically significant.

2.3 Results and Discussions

2.3.1 Silica Bead Depositions

In this work close-packed silica-nanobead depositions were used to accurately control surface nano-topography in micorchannels over a broad range of experimental conditions. The influences of these layers on immunoaffinity cell isolation were studied. Since the particle surfaces, glass and TEOS directly treated glass slides are all very smooth with a root mean squared (RMS) roughness less than a few nanometers by AFM measurements, the surface roughness is mainly controlled by the radius of the particles.

The arithmetic surface roughness is defined by the following equation: [76]

$$R_a = \sqrt{\frac{1}{n}\sum_{i=1}^{i=n} Yi^2}$$

Where R_a is the arithmetic surface roughness, n is the number of points along the top surfaces, and Yi is the vertical distance of the ith point from the mean surface height. For close-packed nanobead depositions, R_a can be further expressed as:

$$R_a = \sqrt{\frac{1}{n}\sum_{i=1}^{i=n}\left(\int_{\theta=0}^{\theta=\pi/2} Rcos\theta\right)^2} \text{ = radius of nanobeads}$$

We used convective deposition to create ordered nanobead monolayers atop glass substrates. While humidity, particle size, suspension volume fraction, substrate speed, and blade angle were all found to influence the packing quality of nanoparticles, [74] preliminary work showed that solely varying deposition speed was sufficient to obtain hexagonally close-packed nanobead arrays. The beads were deposited from suspensions at 10.84%-32.40% volume fractions in water. Close-packed morphologies of the deposited layers were verified with scanning electron microscopy (SEM). Optimized deposition speeds for each particle size are summarized in **Table 2.1**. The corresponding nanoparticle layer morphologies are presented in **Figure 2.3**. The size range of nanobeads was chosen because they are on the same order of magnitude as the size of nano-structures on cell membrane, which was suggested to enhance cell capture in previous

work. [17]

Even though the size of the nanobeads used in our study covers a broad range, the increased surface area for cell capture actually remains the same for all sizes and is independent of nanobead diameter as long as the beads have similar packing structure. This can be shown by the following calculation:

$$\text{Total area for cell capture after nanobead depositon} = \frac{Af}{\pi R^2} 2\pi R^2 = \frac{A\pi}{\sqrt{3}}$$

Where *A* is the surface area on the substrate covered by beads, *f* is the fraction of the substrate covered by beads, which is $\frac{\pi}{2\sqrt{3}}$ for 2D hexagonal close-packing, and *R* is the radius of the nanobead. The capture surface area on the nanobead-covered substrates is ~1.8 times of that on a flat substrate, such as TEOS.

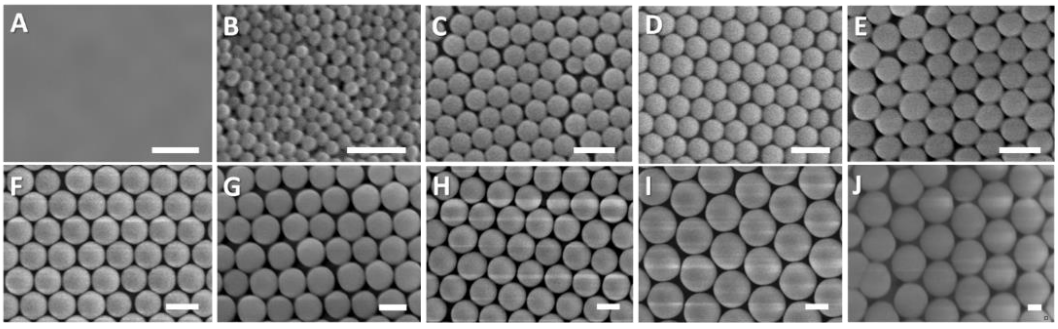

Figure 2.3: Scanning electron microscope images of close-packed particle arrays with diameters of (*B)* 100 nm, (*C)* 309 nm, (*D)* 319 nm, (*E)* 407 nm, (*F)* 460 nm, (*G)* 490 nm, (*H)* 700 nm, (*I)* 928 nm and (*J)* 1150 nm. Image (*A)* shows a glass surface coated with a smooth layer of TEOS. All scale bars = 500nm. Standard deviations of the particle sizes

are summarized in **Table 2.1**. Reprinted with permission from *Effect of Surface Nanotopography on Immunoaffinity Cell Capture in Microfluidic Devices*. [55] Copyright (2011) American Chemical Society.

2.3.2 Live Cell Capture on Silica-Nanobead Substrates

Next the silica nanobead deposited substrates were enclosed within PDMS microchannels and functionalized with CD4 antibodies to capture CD4+ T cells under continuous flow. Three different flow rates, 2, 5 and 8 μl/min, covering the optimal range for CD4+ T cell capture, were evaluated. [66] Jurkat cells, a human T lymphocyte cell line, were used for capture experiments and 23.8% of the cells were found to be CD4+ as by flow cytometry analysis. The total number of captured cells was enumerated as specific capture since the surface chemistry has been shown to yield greater than 95% purity. [66] The number of cells captured on the silica nanobead deposition was normalized to that on a functionalized smooth TEOS surface (approximating a continuous array of infinitely small silica beads) using the formula shown in the *Experimental Section*. This normalization minimizes the effects of any run-to-run non-uniformity and allows direct comparison of capture efficiencies with different surface nanotopography.

Figure 2.4A shows a typical image of cells captured on the nanopatterned surface.

Typically, ~50 cells/mm^2 were captured with 15 minutes sample delivery. Reversing the flow direction did not affect capture results, indicating that the capture difference in the up- and downstream regions was not due to target cell depletion. **Figures 2.4B-2.4D** show that nanopatterned surfaces generally improve capture efficiency versus smooth substrates, however, the two do not have a monotonic relationship. Statistically significant data sets are highlighted. Data points with * have a statistically different cell capture compared with the capture on TEOS under the same flow rate with $p < 0.1$. Data points in red circles have statistically different cell capture as compared to their preceding neighbor (neighboring data set of a smaller nanobead size) with $p < 0.1$. The cell capture efficiency profile strongly depends on flow rate. At 2 μl/min (wall shear stress of 5.5×10^{-5}N/m^2) the capture efficiency increases nearly continuously from 100%, the normalization value on smooth TEOS (control) to 160% on roughened surfaces with the largest beads (1150nm). Interestingly the capture efficiency dips on surfaces coated with 700 nm particles to the level of the control, smooth TEOS, samples. At 5μl/min (wall shear stress of 1.385×10^{-4}N/m^2) the cell capture efficiency first climbs with increased surface roughness, and gradually decreases as bead size further increases. An outlier to this trend is a significant decrease in capture efficiency with a 407 nm bead-patterned

substrate—this yielded only 60% capture as compared with the smooth TEOS surface. The 8 μl/min (wall shear stress of $2.215 \times 10^{-4} N/m^2$) trend follows the 5 μl/min capture profile. The cell capture efficiency nearly doubles for the smallest deposited particles then decreases with nanobeads greater than 700 nm in diameter. The capture profile shows two significant dips at 407 and 490 nm where the capture efficiencies are comparable to those on smooth surfaces. Thus cell capture on rough surfaces is not only dependent on surface topography but also on wall shear stress.

The complex capture profiles are not expected to result from increased surface area after nanobead deposition. The difference between TEOS and nanobead surfaces are likely due to surface area increase (an 80% increase in surface area with nanobead deposition), but difference on the various beads are not (surface area is independent of nanobead size under hexagonal close-packing). It is also unlikely a result of surface chemistry or antibody density as different-sized beads were synthesized under the same TEOS hydrolysis reaction with only reaction time and reagent concentration varying. In addition, under static incubation cell capture was comparable on patterned substrates of various bead sizes and smooth TEOS (data not shown); this also suggests comparable surface chemistry among the different roughness conditions.

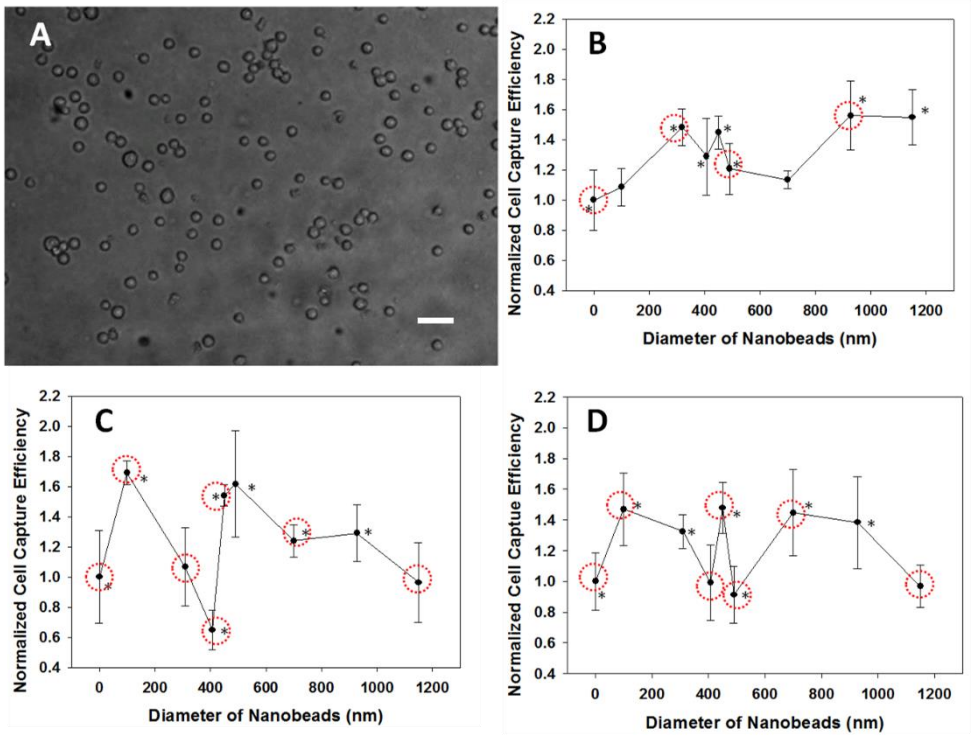

Figure 2.4: (*A)* Bright field image showing CD4+ cells captured on a surface patterned with 928nm beads under 5 µl/min sample flow (scale bar = 50µm). (B)-(D) Normalized capture efficiency on nanobead-covered substrates. Cell suspension flow rates were *(B)* 2 µl/min, *(C)* 5 µl/min, and *(D)* 8 µl/min. The numbers of cells captured on the silica nanobead surfaces were normalized to those on smooth TEOS-coated surfaces (approximating a particle layer of infinitely small particles) for direct comparison of capture efficiencies. Error bars show one standard deviation in 5-10 trials. Data points labeled with * have a statistically different cell capture compared with the capture on

TEOS with $p < 0.1$, while data points in red circles have a statically different cell capture compared to its preceding neighbor (neighboring data set of a smaller nanobead size) with $p < 0.1$. Reprinted with permission from *Effect of Surface Nanotopography on Immunoaffinity Cell Capture in Microfluidic Devices*. [55] Copyright (2011) American Chemical Society.

Cell capture on rough surfaces under continuous flow could be influenced by cell movement near substrates, shear induced deformation, and increased capture surface area as proposed previously. Inertial migration of flowing cells, however, should not be a main contributor to the complex capture patterns as the Reynold's number Re is much smaller than 1 under all flow conditions. Numerical simulation (**Figure 2.5**) confirms that the flow is essentially undisturbed at heights roughly two bead-diameter from the bottom substrate. Even the largest particles deposited here (1150 nm in diameter) are much smaller than Jurkat cells (7-20 μm in diameter [77]) captured. As a result, cell movement under these near Stokes flow conditions should not significantly undulate with surface topography or lead to any abrupt changes to cell migration at the dipping points in the capture efficiency curves. In addition, in these dilute cellular suspensions, multibody hydrodynamic interactions are also minimal. The only nonlinear behavior in this near-

wall interaction is the elasticity of the cellular membrane. We thus hypothesize that mechanical deformation of cells on the cellular and sub-cellular level is the key factor contributing to the complex capture profiles observed.

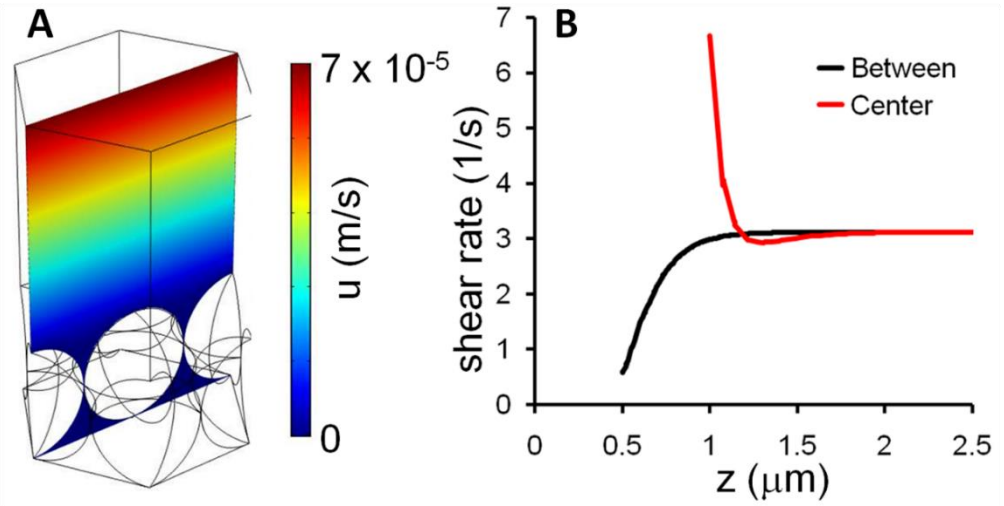

Figure 2.5: (*A)* Fluid velocity profile at a cross-section parallel to the flow direction simulated by COMSOL. Velocities and shear rates correspond to 2 μL/min. Not far from the beads the flow profile nears Poiseuille conditions and is essentially undisturbed by the bead patterns. The shear rate along the z-direction above the bead center and above the two bead contact point at various height points were computed and shown in *(B)*. Greater than two bead diameter from the glass surface, velocity differences between the two points are effectively zero and the flow is no longer disturbed by the imposed roughness. Reprinted with permission from *Effect of Surface Nanotopography on Immunoaffinity Cell Capture in Microfluidic Devices*. [55] Copyright (2011) American Chemical Society.

2.3.3 Capture of Glutaraldehyde Fixed Cells on Silica-Nanobead Substrates

To evaluate the hypothesis that cell mechanical properties influence their capture, Jurkat cells were fixed with 1% glutaraldehyde and used in capture experiments under 5 μl/min flow. Glutaraldehyde crosslinks amine groups and thus can increase the Young's modulus of cells by greater than an order of magnitude. [78] **Figure 2.6** shows the normalized capture efficiency of fixed cells: capture efficiency increases slightly for the smallest nanobead layers then gradually decreases. With fixed cells no dip in cell capture efficiency is seen and the surface topography effects are greatly dampened as no statically significant difference was found no matter when neighboring data points were compared or when the capture on nanobeads were compared to that on flat TEOS.

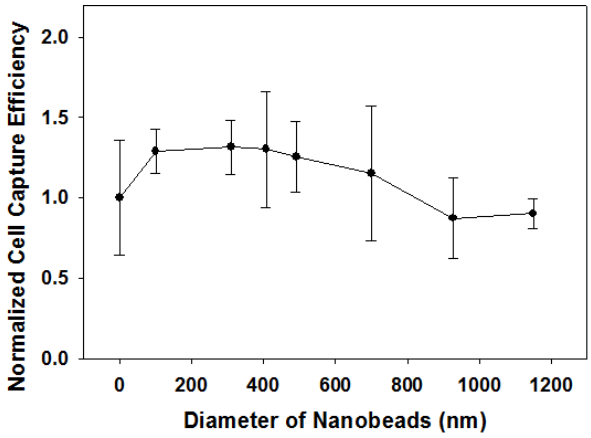

Figure 2.6: Capture of glutaraldehyde-fixed Jurkat cells from culture media onto nanobead-patterned substrates at 5μl/min. Numbers of cells captured on nanobeads were normalized to those captured on flat TEOS-coated surfaces. The error bars represent one

standard deviation as calculated from greater than four repeats of each condition. *p* value was found to be greater than 0.126 for every data point, either comparing with capture efficiency on TEOS or its preceding neighbor, indicating that capture on the various surfaces was not significantly different. Reprinted with permission from *Effect of Surface Nanotopography on Immunoaffinity Cell Capture in Microfluidic Devices*. [55] Copyright (2011) American Chemical Society.

To further verify the different capture between live and fixed cell, live (triangles in **Figure 2.7**) and fixed (dots) Jurkat cells were mixed at a 1:1 ratio for capture on 490nm beads under 5 μl/min (empty symbols) and 8 μl/min flow (solid symbols). As shown in **Figure 2.7**, the normalized capture efficient is consistent with the results in **Figure 2.4** and **Figure 2.6** using live or fixed cells alone under the respective conditions. In addition, capture of glutaraldehyde-fixed cells is much less sensitive to change in surface roughness: under 5 μl/min flow, the *p*-value is 0.7597 when comparing capture of fixed cells on 490 nm bead monolayers to that on smooth TEOS, while there is a significant difference for live cell capture on the two surfaces ($p = 0.0002$). Live cell capture is also highly sensitive to the flow rate, showing by the significant difference of capture efficiency at the two tested flow rates ($p = 0.00518$).

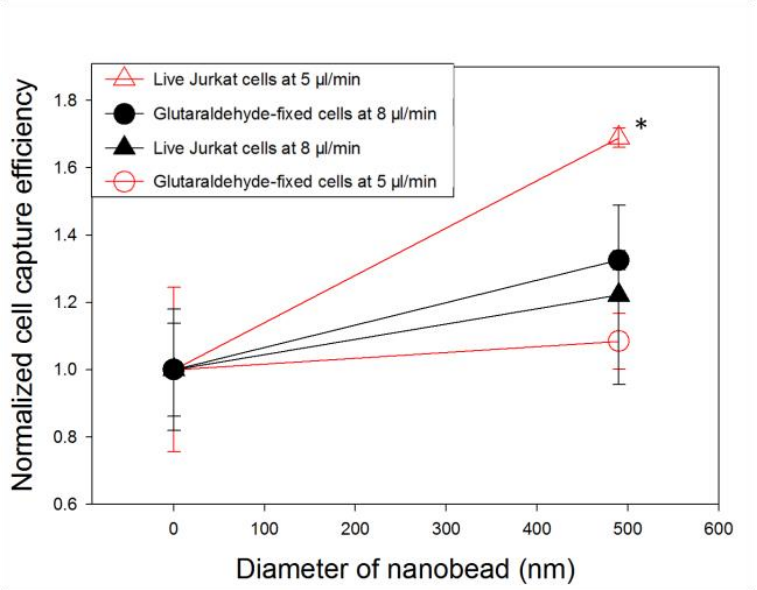

Figure 2.7: Capture of glutaraldehyde-fixed and live Jurkat cell mixture (1:1 ratio) from culture media onto 490 nm nanobead-patterned substrates at 5µl/min and 8µl/min. Numbers of cells captured on nanobeads were normalized to those captured on flat TEOS-coated surfaces. The error bars represent one standard deviation as calculated from greater than three repeats under each condition. Data point labeled with * have a statistically different cell capture compared with the capture on TEOS with $p < 0.1$. Reprinted with permission from *Effect of Surface Nanotopography on Immunoaffinity Cell Capture in Microfluidic Devices*. [55] Copyright (2011) American Chemical Society.

To test if glutaraldehyde fixation interferes with antibody-antigen binding chemistry, we

fixed Jurkat cells with glutaraldehyde and then stained the nuclei with Hoechst 33258. Afterwards, fixed and stained Jurkat cells were mixed with live cells at a 1:1 ratio. The cell mixture was manually injected into a PDMS microchannel bonded to functionalized bare glass and incubated under static conditions for 15 minutes. The device was rinsed and captured cells were counted. **Figure 2.8** shows a representative image. Average cell counts from multiple devices and imaging areas show that identical numbers of fixed and untreated cells were captured. This suggests that the different capture profiles of live and fixed cells are not due to altered antibody-antigen interactions.

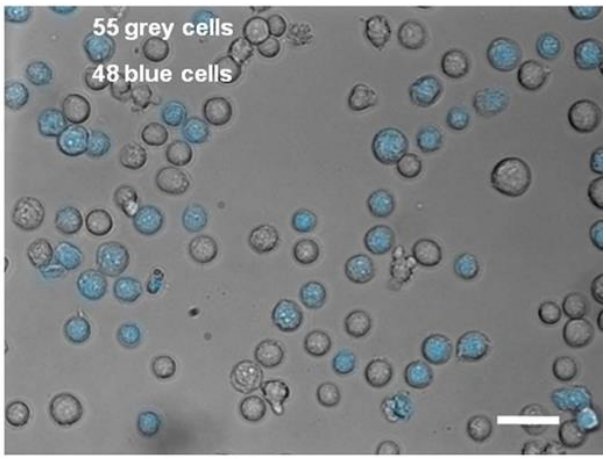

Figure 2.8: Representative bright field image showing the capture of glutaraldehyde-fixed (blue) and live (grey) Jurkat cells mixed 1:1 in culture media on antibody-functionalized bare glass substrates under static incubation. Average cell counts from multiple devices and imaging areas show that identical numbers of fixed and untreated

cells were captured. This indicates that the fixation procedure does not interfere with antibody-antigen recognition. Scale bar = 50μm. Reprinted with permission from *Effect of Surface Nanotopography on Immunoaffinity Cell Capture in Microfluidic Devices*. [55] Copyright (2011) American Chemical Society.

A direct outcome of glutaradehyde fixation is significant enhancement of cell moduli. [78] Live CD4+ cells have a flexible membrane undulating even in static culture medium. The varying levels of shear deformation under different flow rates are expected to influence the interaction area between cells and antibody-coated substrates. Although shear deformation on the cellular level may contribute to the flow rate dependent capture, it does not fully explain cell interaction with nanotopography, which is an order of magnitude smaller than cell dimension in our study.

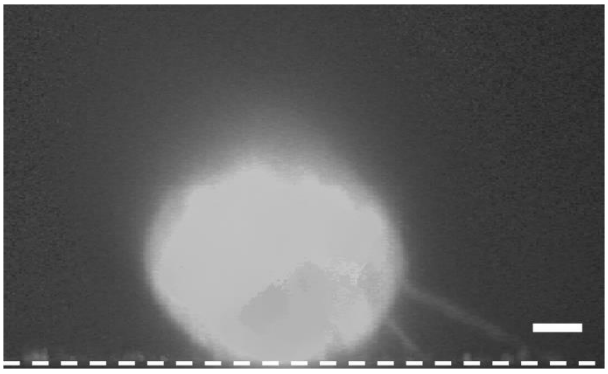

Figure 2.9: A confocal Z-stack image showing tethers from a Rhodamine B stained

Jurkat cell to an antibody functionalized smooth glass substrate (scale bar = 2 μm). After cell capture from continuous flow on an antibody treated smooth glass slide, the flow was stopped and confocal images were acquired. The fluid flowed from the right to the left for cell capture and the substrate locates at the bottom of the image indicated by a dash line. The fuzziness of the membrane away from the substrate is a result of spontaneous membrane fluctuation. Reprinted with permission from *Effect of Surface Nanotopography on Immunoaffinity Cell Capture in Microfluidic Devices*. [55] Copyright (2011) American Chemical Society.

Instead, a more plausible explanation of the capture dependence on surface nano-features and wall shear stress may arise from protruding nano-structures on the cell membrane. The predominant features on the surface of human lymphocytes are microvilli that consist of bundles of cross-linked actin filaments. [79] CD4 receptors, the target antigen in this study, are preferentially located on the microvilli ends. [80] Indeed, we observed cell extensions a few hundred nanometers in diameter tethered to antibody functionalized substrates (**Figure 2.9**), indicating interactions between membrane nanostructures and the capture bed. With a dimension of 300 to 400 nm in length, ~100 nm in width, and a spatial distribution of ~4/μm, [79] microvilli are comparable in size to the nanobeads used

in this study. This comparable dimension scale suggests a physical complementarity between certain substrate nanotopographies and the cell surface in addition to specific antibody-antigen interactions. Complementary interactions have been reported with nanopillars to enhance the capture yield of circulating tumor cells. [17] Optimal capture yield occurs with 6 μm or longer nanopillars which are on the same length scale as the protrusion lengths of tumor cells. [17] In our system, while the amount of immobilized antibody increases continuously with the nanobead diameter, [67] the physical complementarity has a non-monotonic dependence on the nanoparticle size. The interplay of the two factors may strongly contribute to the complex capture profiles on the nanostructured surfaces. Interestingly the tethers observed in **Figure 2.9** are much longer than the length of microvilli measured on unattached lymphocytes. [79] These long extensions may be a result of microvilli being stretched after initial tethering. The diameter of these extensions is also slightly thicker than those measured by AFM or SEM, [79] likely due to optical diffraction. Since microvilli are susceptible to shear forces, highly dynamic and deformable to help cells contact and bind to patterned substrates, [81,82] they can experience different shear deformation and contribute to the flow dependence of the cell capture. While fixed cells also present microvilli, [79] their lack of dynamics and

weak response to shear forces makes capture of fixed cells much less sensitive to the surface topography.

2.4 Conclusions

Close-packed silica bead layers provide a powerful tool to systematically control surface roughness and enhance immunoaffinity cell capture under continuous flow. Interestingly, complicated cell capture efficiency profiles were observed across several flow rates and surface nanotopographies. Hardening cells through glutaraldehyde fixation significantly dampened this dependence. The non-monotonic relationships between the capture efficiency and surface roughness under various flow rates are likely results of complementarity and shear deformation of nano-protrusions on the cell membrane. In future studies, we plan to extend the length scale and investigate the influence of substrate microstructures on cell capture. This relationship between surface topography and cell capture efficiency, once established, will enable more rational design of cell capture devices.

Chapter 3

Short Term Culture, Long Term Culture and Neural Differentiation of Neural Stem Cell Line C17.2 in Microfluidics [39]

3.1 Motivation

Neural stem cells (NSCs) have recently attracted significant interest for their promise in treating neurodegenerative disorders, such as Alzheimer's disease, ischemia and Parkinson's disease. [83–92] Despite progress in neuronal cell differentiation and transplantation of NSCs, future success will require further understanding of the neuronal cell differentiation mechanisms. [84,86,87,89,91,93–101] Microfluidics has recently been shown to be a powerful tool in stem cell research, due to the advantage of precise control of individual environmental cues, single cell analysis, real-time measurement and easy integration with electrical stimulation. [41,102–118] Concentration gradients of cytokine or growth hormone have been created in microfluidic devices to quantitatively study chemical and biological cues that initiate or facilitate neuronal cell differentiation. [32,41,119–121] Microfluidics have also been used to introduce mechanical or topographical stimulation for the analysis of non-chemical cues on neuronal cell differentiation. [122,123]

However, transferring NSC research from traditional petri dish to microfluidics requires careful optimization of the chemical and physical culture conditions in microfluidics. The use of microfluidics in NSC research also presents an issue with regard to dynamic nutrient concentration. As the culture volume is miniaturized, nutrient consumption from cell metabolism is much more pronounced than conventional bulk culture, while it is well established that NSCs are extremely sensitive to serum depletion. *In vivo* neuronal cell differentiation of NSCs occurs when there is a shortage of blood and oxygen supply, as studied in disease models like ischemia. [86,96,97,124–129] For *in vitro* cultures, serum withdrawal is often used to induce neuronal differentiation of NSC. [130–132] Based on the available knowledge up to date, we hypothesize that NSCs could undergo neuronal cell differentiation even in the regular NSC culture media if the volume of media available is limited, which after cell metabolism quickly becomes nutrient depleted. Shear stress also has a significant impact in stem cell differentiation. Many publications show that shear stress determines cell fate or helps to enhance differentiation in different types of stem cells, [133–137] including neural stem cells.[138] While it is desirable to induce differentiation through controlled biological, chemical and physical cues, spontaneous differentiation

needs to be characterized to guide microfluidic design and avoid its interference with mechanistic studies.

Here in this chapter, we optimized the chemical and physical conditions to culture C17.2 NSCs in microfluidics through short term culture and then used microfluidic devices to control the amount of culture medium available and characterized the phenotype of C17.2 NSCs over three weeks in standard culture medium to analyze its long term culture and differentiation. C17.2 is an immortalized mouse neural progenitor cell line established by retroviral-mediated transduction of the avian *myc* oncogene into mitotic progenitor cells of neonatal mouse cerebellum, and an important model system in studies of neural regeneration. [92–94,130–132,139–144] C17.2 NSCs have shown the ability to successfully integrate into the central nervous system of animals used as disease models for Parkinson's, stroke and Alzheimer's. [91–94] Both *in vivo* and *in vitro* studies also demonstrate that C17.2 NSCs undergo neuronal cell differentiation under nutrient depletion, [92,94,130–132,141] which makes them an appropriate cellular model for this work. A medium factor (*MF*) was used as a quantitative measure of available medium to each cell per unit time. The *MF* was defined as the volume of culture medium normalized to the total number of cells at seeding and the feeding period. It was controlled using

microchannels of various heights, since it is otherwise difficult to reduce the height of culture media to below one millimeter in conventional bulk culture, considering the meniscus. Another strategy to control *MF* was to vary the feeding frequency, with higher frequency making more fresh medium available to each cell over time. Cell morphology and quantified immunocytochemistry results were examined to verify the correlation between the resulting differentiated cell population and the *MF*. Critical thresholds of *MF* to maintain the stem cell characteristics were identified. The range of consumption rate of serum molecules involved in the process is also discussed here.

3.2 Materials and Methods

3.2.1 Cell Culture

Immortalized murine neural progenitor cells C17.2 (established cell line [92–94,130–132,139–144] as a generous gift to the Jedlicka Lab from Dr. Evan Snyder, of the Sanford-Burnham Medical Research Institute) were grown on 100 mm polystyrene tissue culture dishes (BioLite, Fisher Scientific) at 37 ℃ in 5% CO2 in air. The culture medium consisted of high glucose Dulbecco's modified Eagle medium (DMEM) (HyClone, Fisher Scientific) supplemented with 10% fetal bovine serum (HyClone, Fisher Scientific), 5% horse serum (TCS Biosciences) and 2 mM L-glutamine (MP Biomedicals).

3.2.2 Microfluidic Device Fabrication

Polydimethylsiloxane (PDMS) microchannels were prepared following the standard soft lithography protocol. Two types of molds were used in this study: SU8 was patterned on silicon wafers for devices with 50 µm and 250 µm heights; micromachined steel molds were used for devices with 500 µm, 1 mm and 2 mm heights. All devices had the same footprint of 1 cm × 4 mm (L × W). A 10:1 mixture of silicone elastomer base and silicone elastomer curing agent (Sylgard 184 silicone elastomer kit, Dow Corning Corporation) was poured onto the molds, degassed, cured at 65-75 ℃ and the microdevices were cut out. Fluid inlets and outlets were drilled using a syringe needle. Microchannels were then autoclaved at 121 ^{o}C for 1 hour. Afterwards, glass bottomed petri dishes (FluoroDish, World Precision Instruments) and the PDMS microchannels were activated by oxygen plasma, carefully aligned and heated for 5-10 minutes at 65-75 ℃ to produce permanent bonding. The control (a standard microwell culture) and one packaged microfluidic device are shown in **Figure 3.1**.

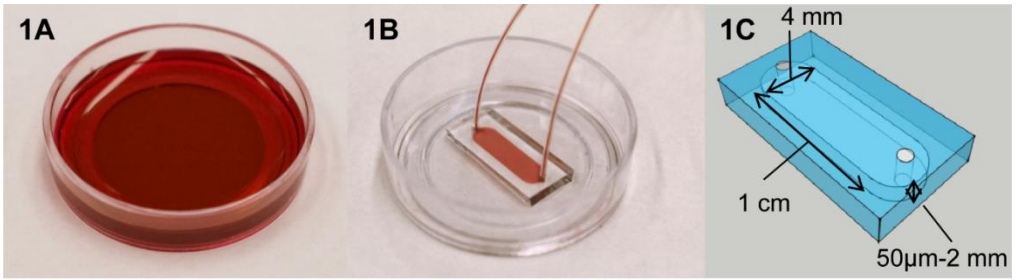

Figure 3.1: A control and PDMS bonded FluoroDish for cell culture. (A) A standard bulk culture on FluoroDish was used as the control. (B-C) PDMS microchannels with a footprint of 1 cm × 4 mm (L × W) and various heights (50 μm, 250 μm, 500 μm, 1 mm and 2 mm) were permanently bonded to FluoroDish to control the amount of medium available to cells. The microchannels were autoclaved prior to bonding and cell culture. Reprinted with permission from *Maintenance and neuronal cell differentiation of neural stem cells C17.2 correlated to medium availability sets design criteria in microfluidic systems*. [39] Copyright: © 2014 Wang et al.

3.2.3 Short Term C17.2 NSC Culture with Different Substrate Chemistry

A number of substrate materials commonly used in microfluidic systems and two standard coating methods were tested to identify the substrate for the optimum adhesion of C17.2. Glass bottomed petri dish (35mm cell culture fluorodish, World Precision Instruments) was used as purchased. Cover glass slides (Fisherbrand microscope cover glass, Fisher Scienctific) were autoclaved at 134^{o}C for 1 hr before coating and usage. PDMS substrates were made by pouring 1.1g of 10:1 mixture of silicone elastomer base and silicone elastomer curing agent into each well of a 6-well plate. After PDMS

substrates were cured at 65 ^{o}C -75 ^{o}C, they were cut out and treated by either UV light overnight or autoclaving at 134^{o}C for 1 hr before coating.

Autoclaved cover glass, UV-treated PDMS and autoclaved PDMS were coated with either collagen or poly-L-lysine to enhance cell adhesion. Collagen (rat tail type I collagen, BD Biosciences) was diluted to 0.1mg/ml by 30% ethanol in deionized water, added to the substrates, treated by UV light overnight and washed 3 times with PBS before use. Poly-L-lysine (MP Biomedicals) was diluted to 0.1mg/ml by PBS, left on substrates for 1 hr, washed with PBS 3 times, let dry for 2 hrs and washed with PBS 3 times again before use.

To test cell adhesion on different substrates, C17.2 cells were treated by trypsin (Hyclone trypsin 0.25%, Fisher Scientific) and seeded onto substrates at 25,000 cells/cm^2 surface density. After 1 day, 3 images were taken from each sample to examine cell adhesion. Image Processing and Analysis in Jave (ImageJ, National Institutes of Health) was used to count the number of pixels covered by cells and the total pixels in an image. The percentage of area covered by cells (the number of pixels covered by cells divided by the total pixels in an image) after 1 day of culture was used to quantify cell adhesion on

different substrates. The substrate with best cell adhesion results was used in further experiments.

3.2.4 Short Term C17.2 NSC Culture in Microchannels with Different Physical Environment

To test cell adhesion and proliferation under different flow patterns, C17.2 cells were treated by trypsin and injected into microchannel at 25,000 cells/cm^2 surface density. After 3 hrs, 3 images were taken for each sample to examine cell adhesion. Then a syringe (1ml plastic syringe, BD Biosciences) loaded with regular cell medium was connected to the microchannel through tubing (Tygon AAQ04091, Saint-Gobain). The flow rates of both continuous and periodic flows were controlled by a syringe pump (Fusion Touch400, Chemyx Inc.). Cells in the continuous flow group were subjected to a continuous flow of 1, 2, 3 and 4 μL/hr. Cells in the periodic flow group were subjected to a pulse flow of 50, 150, 250, 350, 450 and 550 μL/hr for a total volume of 5 μL every 12 hrs. Under all flow conditions, the cell medium in a microchannel was refreshed more than 2 times in 12 hrs. After 1 day, 3 images were taken for each sample to compare with images taken after 3 hrs. ImageJ was used to count the number of pixels covered by cells and the total pixels in an image. The percentage of area covered by cells in an image after

1 day of culture divided by the percentage of area covered by cells in an image after 3 hrs (normalized area cover by cells per image) was used to quantify cell adhesion and proliferation under different flow patterns.

3.2.5 Long Term C17.2 NSC Culture and Neural Differentiation in Microchannels

Trypsinized and suspended C17.2 NSCs were injected into microchannels of different heights: 50 μm, 250 μm, 500 μm, 1 mm and 2 mm. The suspension concentration was adjusted so the surface density was comparable in all devices and was ~25,000 cells/cm^2 after initial cell adhesion. After allowing the cells to adhere for 3 hours, the cells were fed periodically every 12, 24, 48 or 96 hours using a syringe pump. Flow rates were used to generate a comparable wall shear stress of 0.004 Pa in all devices. A total of 2.5 times the device volume was injected at every time interval to ensure complete medium replacement. **Table 3.1** summarizes the conditions used. The flow pattern and feeding interval combination was determined by preliminary experiments. As a control, C17.2 cells were seeded at the same surface density into a FluoroDish without any microchannel. The medium in the control was withdrawn completely and replaced every 48 hours (standard subculture feeding frequency). All devices were kept under humidified environment at 37 ℃ in 5% CO2 in air. Three samples in each condition were

immunostained after 1 week, 2 weeks and 3 weeks of culture to monitor the cell phenotype over time. At least five images were captured at random locations from each sample, thus a total of 15 images or more were analyzed under each condition.

Table 3.1: The microchannel geometries and feeding conditions used in this study.

Reprinted with permission from *Maintenance and neuronal cell differentiation of neural stem cells C17.2 correlated to medium availability sets design criteria in microfluidic systems*. [39] Copyright: © 2014 Wang et al.

Microchannel height (μm)	**Flow rate for cell feeding (μL/hr)**	**Vol. of medium (μL)**	**Feeding interval (hour)**			
50	250	5	12	24	48	-
250	6,250	25	12	24	48	-
500	25,000	50	12	24	48	-
1000	100,000	100	12	24	48	-
2000	400,000	200	-	24	48	96

3.2.6 Immunostaining

Cells were fixed in 3.7% paraformaldehyde (Sigma-Aldrich) for 15 min, permeabilized with 0.1% Triton X-100 (Fisher Scientific) in phosphate buffered saline (PBS, Fisher) for 15 min, and blocked by 1% bovine serum albumin (BSA, Sigma-Aldrich) in 0.01% Triton X-100 for 15 min at room temperature. Both primary and secondary antibodies

were diluted in 0.1% BSA and 0.001% Triton X-100 solution and then incubated with cells overnight for 8-10 hrs at 4 ℃. Primary antibodies used were Nestin (clone Rat-401, Fisher Scientific), anti-β-tubulin-III (AlexaFluor488, clone TUJ1, BD Biosciences) and anti-MAP2 antibody (AlexaFluor488, clone AP20, Chemicon). The secondary antibody for Nestin was AlexaFluor546 anti-mouse IgG_1 (Invitrogen). Finally cell nuclei were stained with 0.002 mg/ml Hoechst No. 33258 (Invitrogen) for 5 min. After rinse, 5 images were captured from each sample using phase-contrast and fluorescence microscopy (Eclipse TE2000U, Nikon). The surface area in each image was 0.15 mm^2. The average number of β-tubulin-III positive cells per mm^2 was calculated to characterize the onset of neuronal cell differentiation. MAP2 staining was carried out in selected sets of samples: 50 μm tall microchannel samples under a 48 hr feeding interval, 2 mm tall microchannel samples under a 48 hr feeding interval and fluorodish samples under a 48 hr feeding interval, to confirm the results from β-tubulin-III staining.

3.2.7 Neurite Measurement

The lengths of neurites were measured using immunostained images. Cells with positive staining by β-tubulin-III and neurite outgrowth greater than two times the size of soma were considered as neuronal cells. Neurite outgrowth from each neuronal cell was

measured by the NeuronJ plugin in ImageJ (National Institutes of Health). The average number of neuronal cells per mm^2 was used to characterize neuronal cell differentiation. The average neurite length (total neurite length divided by the number of neurites in an image) was also calculated.

3.2.8 Medium Factor (MF)

The *MF* was introduced to quantify the amount of medium available to cells over the feeding period. It was calculated by the following equation:

$$MF = \frac{V}{P \times t}$$

Where V is the volume of culture medium, P is the total number of cells at seeding, t is the time interval between two feeding events.

3.2.9 Data Analysis

All data sets in graphs are presented as average $\pm$ standard deviation from repeats in at least three independent devices. When comparing multiple samples in a group, one-way ANOVA test was used with a *p*-value of 0.05. When comparing test samples to the control, two-tailed Student's t test was used with a *p*-value of 0.05.

3.3 Results and Discussions

3.3.1 Short Term C17.2 NSC Culture with Different Substrate Chemistry

In traditional cell culture, poly-styrene is often used as the substrate because it can be readily oxidized, leaving the surface suitable for cell adhesion. [145] In microfluidics systems, PDMS and glass are often used because they can be easily packaged using oxygen plasma. When moving cells from traditional substrate to new ones, the first step is inevitably to make sure the surface is suitable for cell spreading and adhesion. While the materials themselves are important, the way they are processed and whether they are coated with cell adhesion molecules are also crucial to optimize cell adhesion. In this experiment, glass cover slides, glass bottomed petri dish and PDMS were used as substrate materials. When sterilizing glass, autoclaving was used as sterilization method (A-Glass). Both UV light (UV-PDMS) and autoclaving methods (A-PDMS) were tested on PDMS because UV light merely sterilizes PDMS while autoclaving is believed to further crosslink PDMS and evaporate solvent residues. [146,147] Two cell adhesion molecules, collagen (abbreviated as C) and poly-L-lysine (abbreviated as PLL) were also used to enhance the results.

C17.2 cells were given 1 day to adhere to substrates after seeding. The percentage of area covered by cells in an image was used to quantify cell adhesion on different substrates.

PDMS itself, whether sterilized by UV or autoclaving, showed very little promise for cell adhesion, probably due to its high hydrophobicity. Autoclaved glass showed slightly better results ($p=0.00023$ compared with UV-PDMS, $p=0.00032$ compared with autoclaved-PDMS, $p<0.1$. Comparison group is labeled with **). Both collagen and PLL coating improved cell adhesion on PDMS and glass as expected (p range from 0.000008 to 0.047, $p<0.1$). Interestingly collagen improved cell adhesion to different degrees on different materials and even on the same material with different sterilization treatment (UV-PDMS with collagen coating in **Figure. 3.1B** and autoclaved-PDMS with collagen coating in **Figure. 3.1E**, $p=0.00031$, $p<0.1$. Comparison group is labeled with ***). This is the result of complex driving forces behind the assembly of the coating molecules itself and the interaction between coating molecules and the substrate.[61, 62] Glass-bottomed petri dish had the best cell adhesion and was chosen as the substrate material to conduct further experiments (p range from 0.0001 to 0.048, $p<0.1$. Labeled with *.).

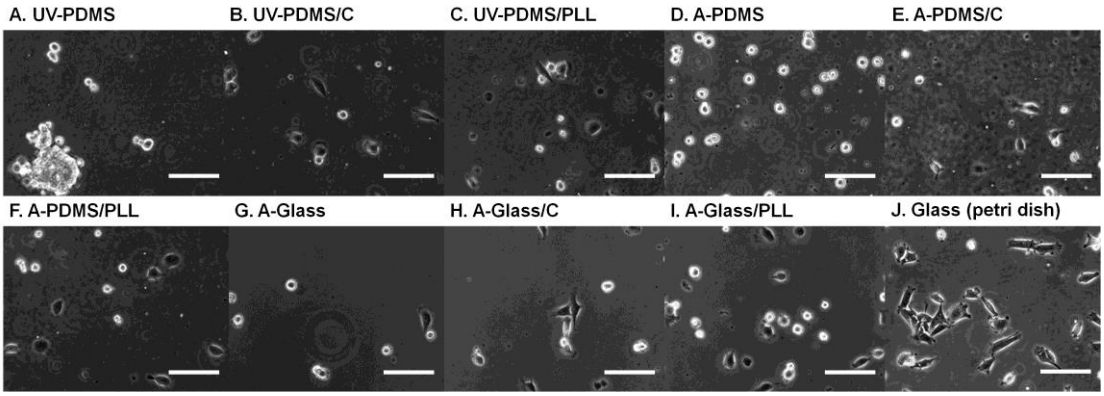

Figure 3.1. Cell morphology after adhesion on different substrates. The morphology of C17.2 cells after 3 hours of adhesion on (A) UV sterilized PDMS (UV-PDMS), (B) UV-PDMS coated with collagen (UV-PDMS/C), (C) UV-PDMS coated with poly-L-lysine (UV-PDMS/PLL), (D) autoclaved PDMS (A-PDMS), (E) autoclaved PDMS coated with collagen (A-PDMS/C), (F) autoclaved PDMS coated with poly-L-lysine (A-PDMS/PLL), (G) autoclaved glass (A-Glass), (H) autoclaved glass coated with collagen (A-Glass/C), (I) autoclaved glass coated with poly-L-lysine(A-Glass/PLL) and (J) glass bottomed petri dish (Glass petri dish). Glass bottomed petri dish had the best cell adhesion and was chosen as the substrate material for further experiments. Scale bar=100 μm.

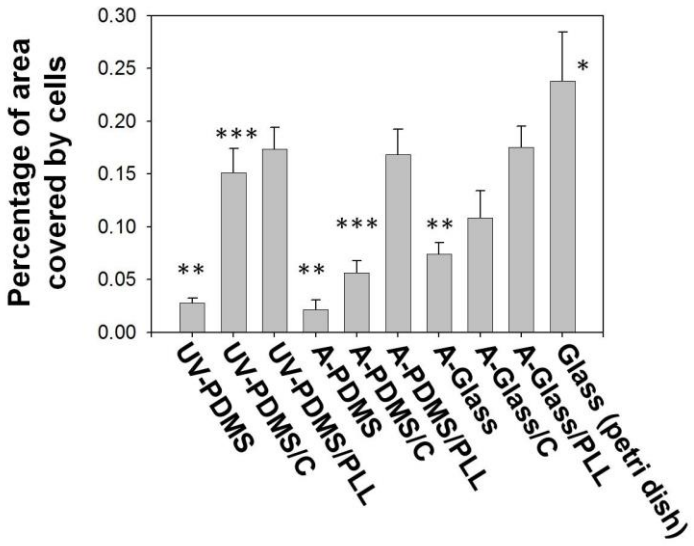

Figure 3.2: Cell adhesion on different substrates. C17.2 cell adhesion was tested on UV sterilized PDMS (UV-PDMS), UV-PDMS coated with collagen (UV-PDMS/C), UV-PDMS coated with poly-L-lysine (UV-PDMS/PLL), autoclaved PDMS (A-PDMS), autoclaved PDMS coated with collagen (A-PDMS/C), autoclaved PDMS coated with poly-L-lysine (A-PDMS/PLL), autoclaved glass (A-Glass), autoclaved glass coated with collagen (A-Glass/C), autoclaved glass coated with poly-L-lysine(A-Glass/PLL) and glass bottomed petri dish (Glass petri dish). Glass bottomed petri dish (with *) had statistically higher cell adhesion comparing to the rest ($p<0.1$) and was chosen as the substrate material for further experiments. N=4.

3.3.2 Short Term C17.2 NSC Culture in Microchannels with Continuous and Periodic Flow

Two approaches can be employed to culture cells in microfluidics: continuous flow generating low shear stress over the whole course of culture or periodic flow generating larger shear stress over a short time. Given that little has been done to culture C17.2 in microchannels, we examined both approaches. C17.2 cells were seeded into microchannel and fed with continuous flow of 1, 2, 3 and 4 μL/hr or periodic flow of 50, 150, 250, 350, 450 and 550 μL/hr for a total volume of 5 μL every 12 hrs. The percentage of area covered by cells in an image after 1 day of culture divided by the percentage of area covered by cells in an image after 3 hrs (normalized area cover by cells per image) was used to quantify cell adhesion and proliferation under different flow patterns. As shown in **Figure. 3.3** and **Figure. 3.4**, a continuous flow of 2 μL/hr and 3 μL/hr resulted in the highest cell adhesion and proliferation over a range of flow rates, while a periodic flow of 250 μL/hr was optimal for cell adhesion and proliferation. In both cases, diversion from the optimal flow rate resulted in a progressive decrease in cell adhesion and proliferation. As we compare the results from both continuous and periodic flow groups, significantly increased cell proliferation was observed in periodic flow group

under flow rates of 150, 250, 350 and 450 μL/hr compared to the best result from the continuous flow group. The flow pattern yielding the best adhesion and proliferation result, a periodic flow of 250 μL/hr, was used for later experiments.

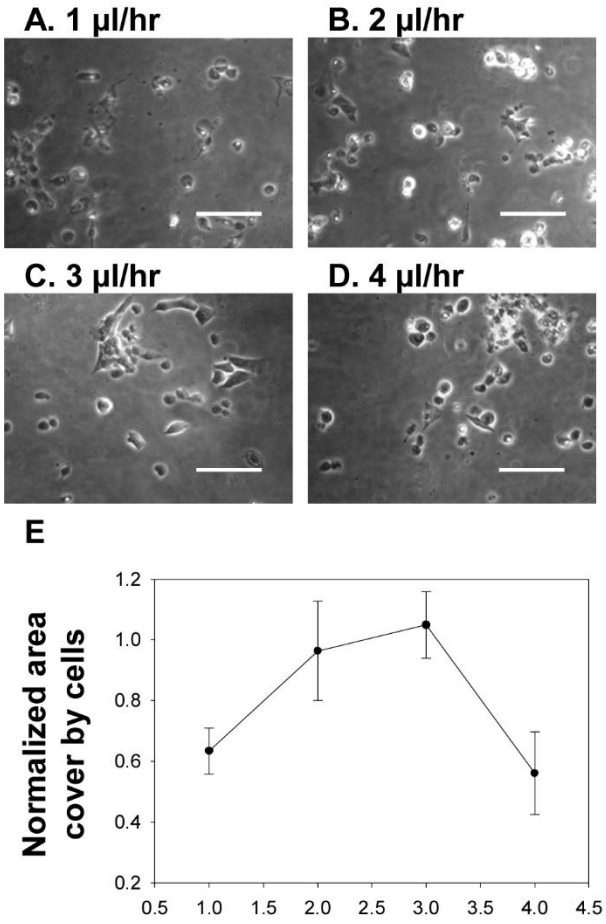

Figure 3.3: Cell adhesion and proliferation in 50 μm microchannel with continuous flow of regular stem cell culture medium. C17.2 cell adhesion and proliferation was tested in 50 μm tall microchannel with continuous flow of 1, 2, 3 and 4 μL/hour. (A-D) Cell

morphologies after 1 day of continuous flow of medium at different flow rates. (S1.E) The surface area covered by cells after 1 day of culture was normalized to that after 3 hour of static adhesion (E) to estimate the number of cells in the microchannels. Continuous medium feeding at 3 μL/hour yielded the highest number of adherent cells after 1 day of continuous flow, but little cell proliferation was observed. Scale bar=100 μm. N≥15. Reprinted with permission from *Maintenance and neuronal cell differentiation of neural stem cells C17.2 correlated to medium availability sets design criteria in microfluidic systems*. [39]

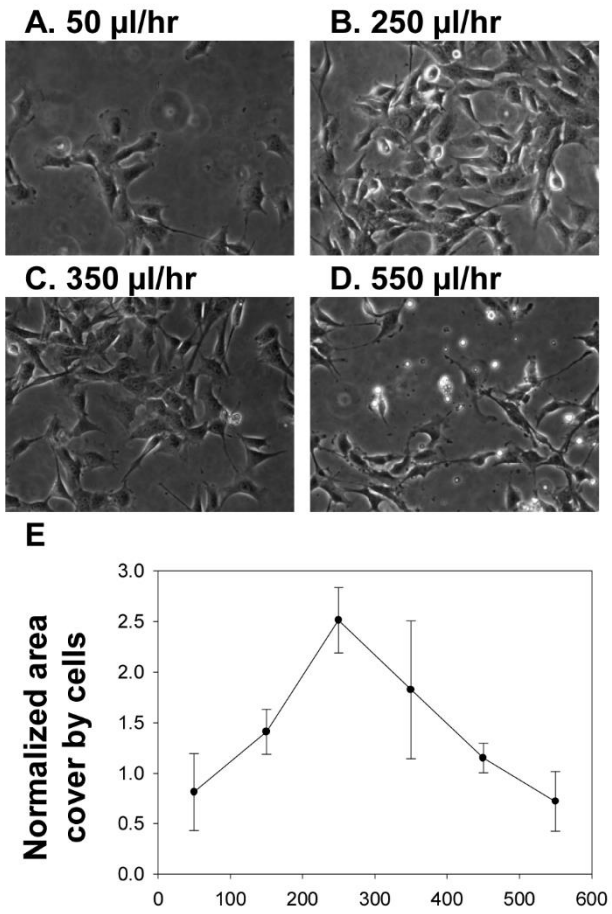

Figure 3.4: Cell adhesion and proliferation in 50 µm microchannel with periodic flow of regular stem cell culture medium. C17.2 cell adhesion and proliferation was tested in 50 µm tall microchannel with periodic flow of 50, 150, 250, 350, 450 and 550 µL/hour administered every 12 hours. (A- D) Cell morphologies after 1 day of continuous flow of medium at different flow rates. (E) The surface area covered by cells after 1 day of culture is normalized to that after 3 hour of static adhesion (E) to estimate the number of cells in the microchannels. Periodic medium feeding at 250 µL/hour every 12 hours

yielded the highest number of adherent cells and significant cell proliferation after 1 day of continuous flow. Scale bar=100 μm. N≥15. Reprinted with permission from *Maintenance and neuronal cell differentiation of neural stem cells C17.2 correlated to medium availability sets design criteria in microfluidic systems*. [39] Copyright: © 2014 Wang et al.

3.3.3 Short Term C17.2 NSC Culture in Microchannels under Different Frequencies

Different frequencies to feed C17.2 cells in 50 μm tall microchannel with a periodic flow of 250 μL/hour were examined. The percentage of area covered by cells in an image after 1 day of culture divided by the percentage of area covered by cells in an image after 3 hrs (normalized area cover by cells per image) was used to quantify cell adhesion and proliferation under different flow patterns. Cell morphologies after 1 day of continuous flow of regular stem cell culture medium at different flow rates is shown in **Figure 3.5A-D**. In **Figure 3.5E**, the surface area covered by cells after 1 day of culture was normalized to that after 3 hour of static adhesion to estimate the number of cells in the microchannels. Periodic medium feeding at 250 μL/hour administered every 12 hours yielded the highest number of adherent cells after 1 day of continuous flow. Feeding

periods less than 12 hours led to significant less adherent cells in the device. Thus, only feeding periods of 12 hours or higher were used in the work.

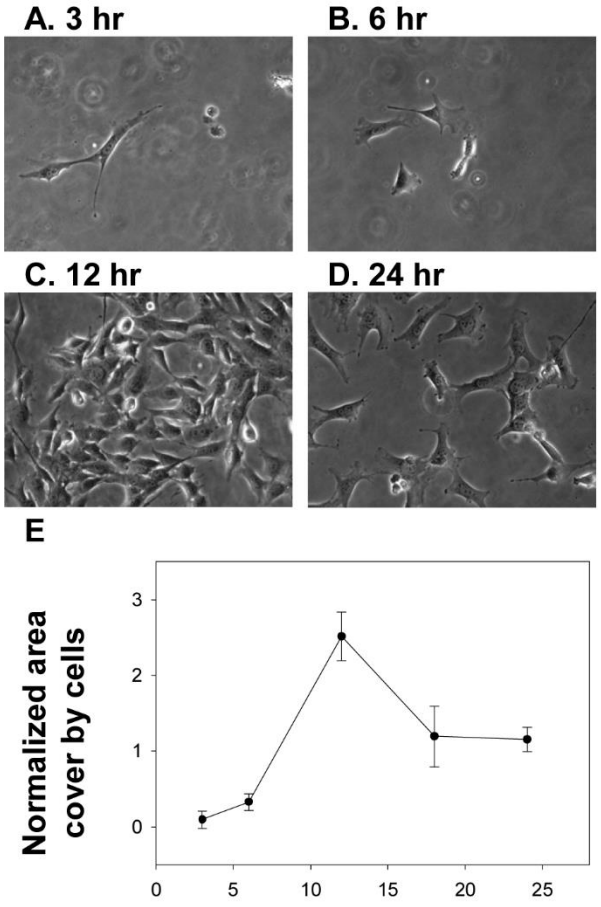

Figure 3.5: Cell adhesion and proliferation under different frequencies. C17.2 cell adhesion and proliferation was tested under different feeding frequencies in 50 μm tall microchannel with a periodic flow of 250 μL/hour. (A- D) Cell morphologies after 1 day of continuous flow of regular stem cell culture medium at different flow rates. (E) The surface area covered by cells after 1 day of culture was normalized to that after 3 hour of

static adhesion to estimate the number of cells in the microchannels. Periodic medium feeding at 250 μL/hour administered every 12 hours yielded the highest number of adherent cells after 1 day of continuous flow. Feeding periods less than 12 hours led to significant less adherent cells in the device. Thus, only feeding periods of 12 hours or higher were used in the work. Scale bar=100 μm. N≥15. Reprinted with permission from *Maintenance and neuronal cell differentiation of neural stem cells C17.2 correlated to medium availability sets design criteria in microfluidic systems*. [39] Copyright: © 2014 Wang et al.

3.3.4 Long Term C17.2 NSC Culture in Microchannels

To test if the neuronal cell differentiation can be induced by shear stress, cell population in 2000 μm microchannels was compared to that in bulk culture (**Figure 3.6**), as the *MF* factors were similar in these cases. Little morphological and biomarker change was observed over time in all samples (images not shown), demonstrating minimal neuronal cell differentiation. When the results were quantitatively analyzed, the cell population with the 24 hr feeding intervals showed lower number of β-tubulin-III positive cells compared to the control (**Figure 3.6A**) at 1 week (with * above, p=0.00004). This is possibly due to more thorough medium replacement in microfluidics as compared to

traditional pipetting in petri dishes: the channel is flushed with fresh medium 2.5 times the channel volume at every cell feeding, while in traditional petri dish culture, the old medium is suctioned up and replaced with equal volume of fresh medium once. The rest of the microfluidic samples shared comparable number of β-tubulin-III positive cells to the control (*p* values range from 0.08 to 0.9). As shown in **Figure 3.6B**, all samples had lower number of neuronal cells compared to the control in the first week (*p* values range from 0.02 to 0.04), but the difference diminished later. From **Figure 3.6C**, it was observed that the average neurite length of most samples were similar to the control except for those without noticeable neurite outgrowth (with "O" in **Figure 3.6B** and **Figure 3.6C**). The ANOVA tests for samples from the same time points demonstrated comparable density of β-tubulin-III cells and neurite length in the 2000 μm channels. The density of neuronal cells were significantly different under the various feeding intervals (brackets and * underneath the groups, $p<0.05$), but the difference was due to a reduced neuronal density than the control. The neurite length was comparable. The ** under the groups in **Figure 3.6C** and **3.6D** indicate difference due exclusively to the samples with zero positive cells. These results show that the neuronal cell differentiation cannot be

initiated by introducing shear stress generated by feeding in microfluidics over long term culture.

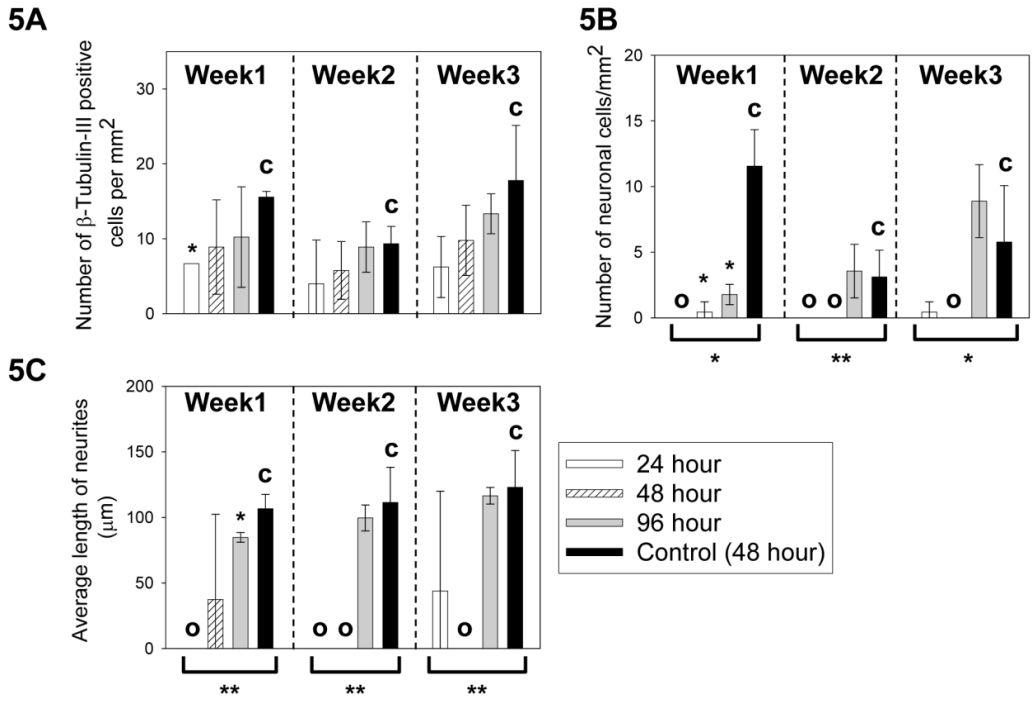

Figure 3.6: Behavior of C17.2 cells cultured in microchannels under shear stress. (A) The β-tubulin-III positive cell counts per mm^2 over time. (B) The neuronal cell counts per mm^2 over time. (C) The average neurite length per mm^2 over time. Groups lacking neuronal cells were labeled with "O". The control (with "c") was C17.2 NSCs seeded at the same surface density in FluoroDishes but without microchannels and fed every 48 hours as in standard subculture protocols. The * above the bars indicated a statistical difference between the sample and the control by two-tailed Student's t test (p <0.05).

The * below the bars indicated a statistical difference in the group by one way ANOVA (p <0.05). The ** in Figure C indicates a significant difference due exclusively to the samples with no neurite outgrowth. N≥15. Reprinted with permission from *Maintenance and neuronal cell differentiation of neural stem cells C17.2 correlated to medium availability sets design criteria in microfluidic systems*. [39] Copyright: © 2014 Wang et al.

3.3.5 C17.2 Differentiation in Microchannels with Different Heights but Fixed Feeding Frequency

First, we examined C17.2 NSCs cultured in microchannels with different heights under fixed feeding frequency. In this case, the *MF* scales linearly with the microchannel height. As a control, cells were seeded at the same surface density in FluoroDish without microchannels (with "c" in all graphs). The average medium height in the open culture is ~2 mm, calculated by the volume of medium divided by the surface area of the dish bottom, and the cells were fed every 48 hours as in standard subculture protocols.

The progression of cell morphology over time is shown in **Figure 3.7A** and the quantified immunocytochemistry results are shown in **Figure 3.7B-D**. As shown in **Figure 3.7A**, groups with lower *MF* values (50 μm, 250 μm and 500 μm microchannels) began to have morphological change consistent with neuronal cell differentiation after 1

week. This trend became dominant after 2 weeks with the 50 μm microchannel yielding almost a pure population of cells with neurite outgrowth and positive β-tubulin-III staining. On the other hand, Nestin staining (red) weakened on the elongated cells, and became nearly undetectable in the 50um group in week 2, also suggesting neuronal cell differentiation. When the images were analyzed quantitatively, the cell populations in 50 μm, 250 μm and 500 μm microchannels were found to show significantly higher number of β-tubulin-III positive cells compared to the control (with * above the bars, *p* values range from 0.00001 to 0.04) over the entire experimental course of 3 weeks (**Figure 3.7B**). The β-tubulin-III positive cell number continued to grow over time, demonstrating an overall tendency towards the neuronal cell differentiation fate. However, neuronal cells (defined here as β-tubulin-III positive cells with neurite length longer than two times that of soma) peaked around 2 weeks and degenerated afterwards (**Figure 3.7A** and **Figure 3.7C**), as seen by reduction of the neuronal density and weaker β-tubulin-III staining at week 3. The 50 μm microchannel showed significantly higher number of neuronal cells compared to the controls (with * above, *p* values range from 0.0003 to 0.0015) at all time points. The 250 μm microchannel showed significantly higher number of neuronal cells compared to the controls (with * above, *p* values are 0.013 and 0.028

respectively) in the first 2 weeks. The 500 μm microchannel showed significantly more neuronal cells than the control only in week 2 (with * above, p=0.001), but not in week 1 or 3. The 1000 μm and 2000 μm samples, on the other hand, showed comparable or lower level of neuronal cell differentiation compared to the control, as demonstrated by lack of morphological change (images similar to those of the control, not shown) as well as the low number of β-tubulin-III positive cells (**Figure 3.7B**) and a baseline presence of neuronal cells (**Figure 3.7C**). For the 500 μm microchannel, the average neurite length was slightly higher than the control after 1 week of culture (with * above, p= 0.04). The average neurite length (**Figure 3.7D**) was the same for the rest of the test conditions and time points (p values range from 0.09 to 1), except for those lacking observable neurites (with "O" in **Figure 3.7C** and **Figure 3.7D**). The low level of neuronal differentiation limits the data points collected from the tall channels (1000 and 2000 μm), resulting in large standard deviation in **Figure 3.7D**. Samples from different channel heights but the same weeks were further analyzed using ANOVA. Groups with statistical difference among the samples (p<0.05) were marked by brackets and * underneath. For the density of β-tubulin-III positive cells and neurons, the various device heights led to statistically different results at the same time point. For the neurite length comparison, the device

height did not create significant difference at week 1. The significant difference of neurite length observed at week 2 and week 3 (with ** underneath, $p<0.05$) was due exclusively to samples with zero neurite outgrowth in the groups. Thus, the neurite length was comparable among all samples with detectable neurite outgrowth at the same week.

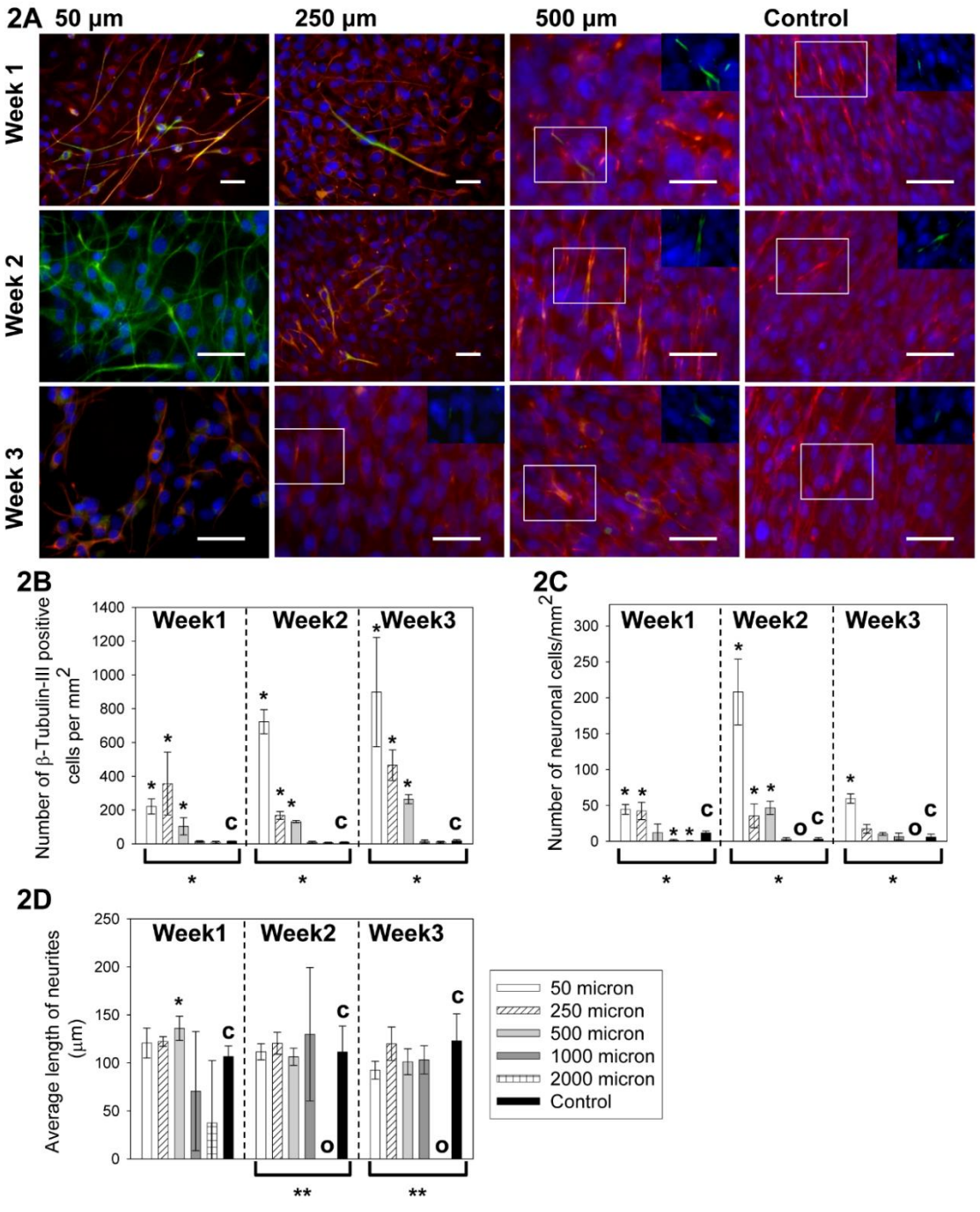

Figure 3.7: Neuronal cell differentiation of C17.2 cells cultured in microchannels with different heights of 50-2000 µm under a 48 hr feeding interval. (A)The cell morphological change over 3 weeks. Images from the 1000 and 2000 micron samples

were not shown since they had similar morphology and staining results as the control for all three weeks. Red: Nestin. Green: β-tubulin-III. Blue: cell nuclei. In some samples, the β-tubulin-III staining was shadowed by the Nestin staining after triple overlay, due to the small number of spontaneously differentiated cells in these samples. In these samples, overlays of the β-tubulin-III and nuclei staining were shown in the inset from the boxed areas. Scale bar=50 μm. The insets were at the same scale as the main images. (B) The β-tubulin-III positive cell counts per mm^2 over time. (C) The neuronal cell counts per mm^2 over time. (D) The average neurite length measurement over time. Bars with "O" in Figure C and Figure D indicated that no cell was identified as a neuronal cell. In Figures B-D, the control (with "c") was C17.2 NSCs seeded at the same surface density in FluoroDishes but without microchannels and fed every 48 hours as in standard subculture protocols. Data were shown as mean ± standard deviation. The * above the bars indicated a statistical difference between the sample and the control by two-tailed Student's t test (p <0.05). The */** below the bars indicated a statistical difference in the group by the one-way ANOVA test (p <0.05). The ** in Figure D indicated a significant difference due exclusively to the samples with no neurite outgrowth. N≥15. Reprinted with permission from *Maintenance and neuronal cell differentiation of neural stem cells C17.2 correlated*

to medium availability sets design criteria in microfluidic systems. [39] Copyright: © 2014 Wang et al.

3.3.6 C17.2 Differentiation in Microchannels with Fixed Geometry but Different Feeding Frequencies

Next, cell behavior was compared for cultures fed under different frequencies but in microchannels with fixed heights. In this case, the *MF* scales linearly with the reverse of the time interval.

The morphological change of cells in 50 μm microchannel over time is shown in Figure **3.8A** and the quantified immunocytochemistry results are shown in **Figure 3.8B-D**. In all the groups, cells began to develop smaller cell bodies and neurite outgrowth after 1 week (**Figure 3.8A**). After 2 weeks more cells showed neural morphology and positive β-tubulin-III staining. At the same time, the β-tubulin-III staining became stronger as Nestin staining weakened. After 3 weeks of culture, the cells with long neurites started to deteriorate. Instead, another population with flattened cell body and relatively short and unbranched processes began to dominate, which co-expressed both Nestin and β-tubulin-III. As shown in **Figure 3.8B**, the cell populations in 12 hr, 24 hr and 48 hr groups all showed significantly higher number of β-tubulin-III positive cells than the control in all 3

weeks (with * above, *p* values range from 0.00006 to 0.009). The β-tubulin-III positive cell number increased constantly over time, indicating a steady population growth in the overall neuronal cell differentiation path. The large error bars for samples in week 3 are caused by non-uniformly distributed cell population mixture associated with neuronal degeneration. The numbers of neuronal cells are shown in **Figure 3.8C**. The initial growth, peak growth and deterioration of neuronal cells were observed in all groups. At initiation and peak stages, all groups showed significantly higher number of neuronal cells compared to the control (with * above, *p* values range from 0.002 to 0.04). At week 3, the difference in neuronal cell number between the microfluidic groups and the control diminished, except for the group with lowest *MF* (with * above, 48 hours, $p = 0.0003$). The average neurite length was comparable for all groups (*p* values range from 0.15 to 1) as shown in **Figure 3.8D**. The large standard deviation of neurite length at week 3 is a result of neuronal degeneration, leaving behind a mixed population of cells with broad distribution of neurite length. The ANOVA test of different feeding conditions at each time point indicated that the feeding intervals significantly impacted the density of β-tubulin-III positive cells and neurons in the 50 μm channels (brackets and * underneath the groups, $p<0.05$), but not the neurite length ($p>0.05$).

The morphology change of cells over time in 250 μm microchannel is shown in Figure **3.9A** and the quantified immunocytochemistry results are shown in **Figure 3.9B-D**. The cell populations in 24 hr and 48 hr groups showed neurite outgrowth (**Figure 3.9A**) and significantly higher number (**Figure 3.9B**) of β-tubulin-III positive cells than the control at all time points (with * above the bars, *p* values range from 0.0003 to 0.03). However, the 12 hr group had minimal morphological change (**Figure 3.9A**) over 3 weeks. The numbers of β-tubulin-III positive cells in the 12 hr group were comparable to the control at all stages (*p* values range from 0.07 to 1). The numbers of neuronal cells are shown in **Figure 3.9C**. The initial growth, peak growth and deterioration of neuronal cells were observed in 24 hr and 48 hr groups. At the peak stage, groups with lower *MF* values, i.e. with 24 hr and 48 hr feeding intervals, showed significantly higher number of neuronal cells than the control (p=0.00004 and 0.028 respectively). The 12 hr group with higher *MF* started with significantly lower number of neuronal cells comparing to the control (with * above, p=0.03), but the difference became insignificant later (p=0.4 at 2 weeks and p=0.3 at 3 weeks). The average neurite length was comparable to the control for all the samples (*p* values range from 0.09 to 0.9) as shown in **Figure 3.9D**. The ANOVA test for the 250 μm samples at each week also indicated that the density of β-tubulin-III

positive cells and neurons changed significantly with the feeding intervals (brackets and * underneath the groups, $p<0.05$), but not the neurite length.

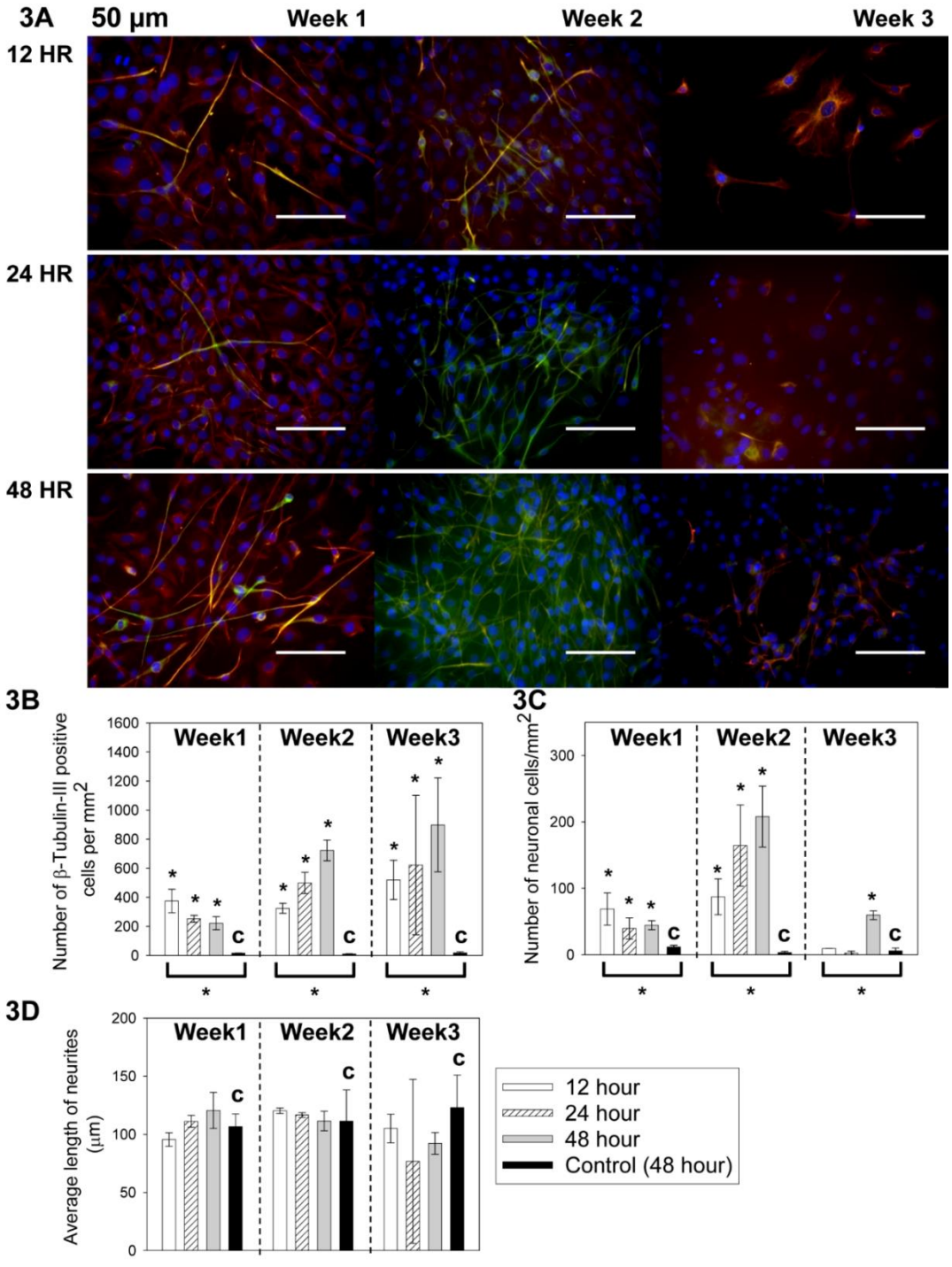

Figure 3.8: Neuronal cell differentiation of C17.2 cells cultured in 50 µm microchannels with 12, 24 and 48 hour feeding intervals. (A) The cell morphological change over 3

weeks. All groups showed biomarker staining and morphological change consistent with neuronal cell differentiation. Red: Nestin. Green: β-tubulin-III. Blue: cell nuclei. Scale bar=100 μm. (B) The β-tubulin-III positive cell counts per mm^2 over time. (C) The neuronal cell counts per mm^2 over time. (D) The average neurite length measurement over time. In Figures B-D, the control (with "c") was C17.2 NSCs seeded at the same surface density in FluoroDishes but without microchannels and fed every 48 hours as in standard subculture protocols. Data were shown as mean ± standard deviation. The * above the bars indicated a statistical difference between the sample and the control by two-tailed Student's t test (p <0.05). The * below the bars indicated a statistical difference in the group by one way ANOVA (p <0.05). N≥15. Reprinted with permission from *Maintenance and neuronal cell differentiation of neural stem cells C17.2 correlated to medium availability sets design criteria in microfluidic systems*. [39] Copyright: © 2014 Wang et al.

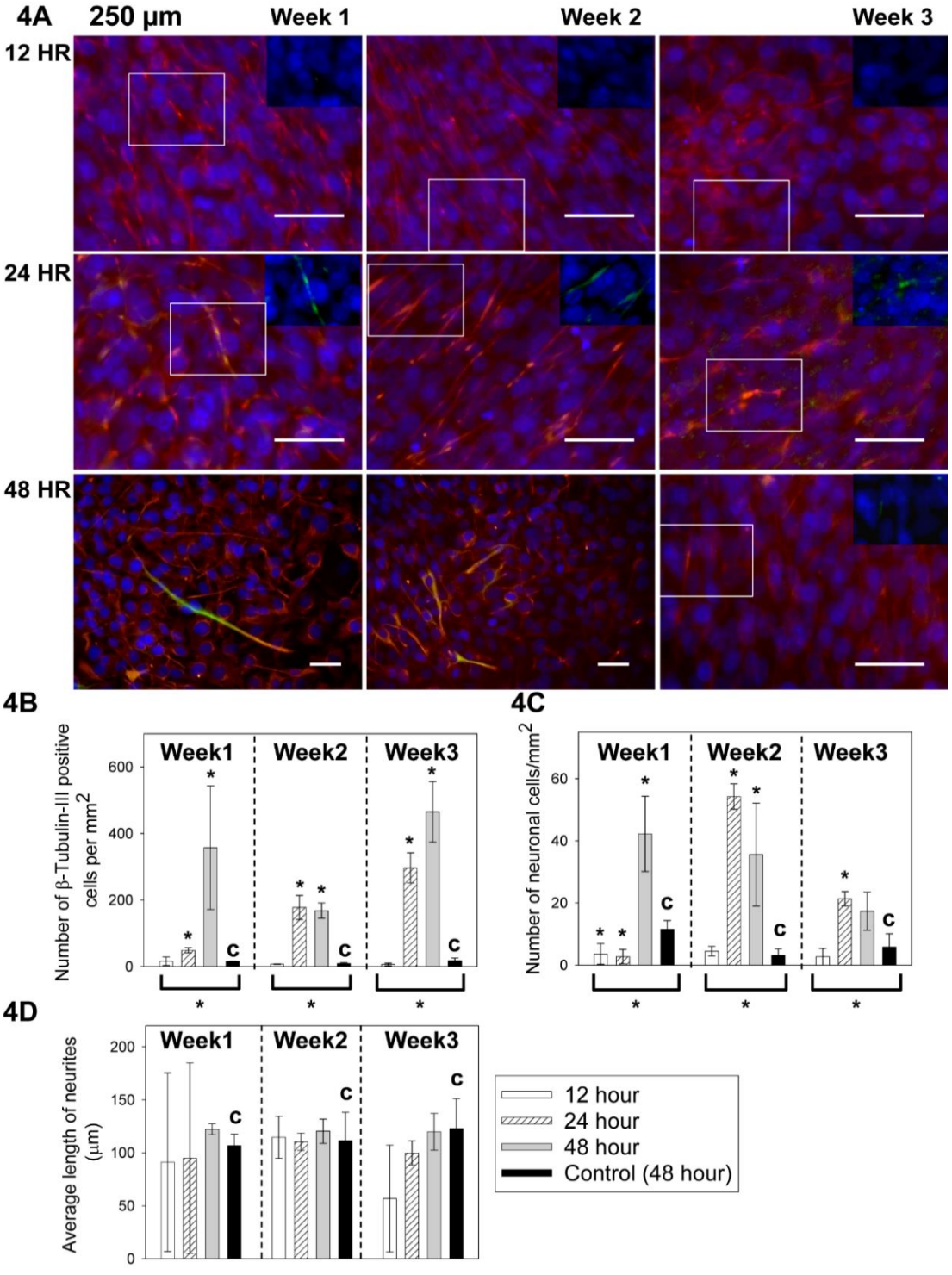

Figure 3.9: Neuronal cell differentiation of C17.2 cells cultured in 250 µm

microchannels with 12, 24 and 48 hour feeding intervals. (A) The cell morphological change over 3 weeks. To better demonstrate the positive β-tubulin-III staining in the 24 hour and 48 hour samples, overlays of the β-tubulin-III and nuclei staining were shown in the inset from the boxed areas. In comparison, insets of β-tubulin-III and nuclei staining were also shown for the 12 hour samples, but β-tubulin-III staining was not visible. Red: Nestin. Green: β-tubulin-III. Blue: cell nuclei. Scale bar=50 μm. The insets were from the boxed region and were at the same scale as the main images. (B) The β-tubulin-III positive cell counts per mm^2 over time. (C) The neuronal cell counts per mm^2 over time. (D) The average neurite length per mm^2 over time. In Figures B-D, the control (with "c") was C17.2 NSCs seeded at the same surface density in FluoroDishes but without microchannels and fed every 48 hours as in standard subculture protocols. Data were shown as mean ± standard deviation. The * above the bars indicated a statistical difference between the sample and the control by two-tailed Student's t test (p <0.05). The * below the bars indicated a statistical difference in the group by one way ANOVA (p <0.05). N≥15. Reprinted with permission from *Maintenance and neuronal cell differentiation of neural stem cells C17.2 correlated to medium availability sets design criteria in microfluidic systems.* [39] Copyright: © 2014 Wang et al.

3.3.7 Confirmation of Differentiation by MAP2 Staining

MAP2 staining was carried out in selected samples to confirm the differentiation characterization by β-tubulin-III staining. Here a MAP2 antibody targeting both MAP2a (expressed constitutively in neuronal cells) and MAP2b (expressed postnatal) isoforms was selected, so it stained differentiated neuronal cells at similar stages as the β-tubulin-III antibody. The selected culture conditions are: 1) a condition in microchannels with the highest level of differentiation, i.e. 50 μm tall microchannel samples under a 48 hr feeding interval, 2) a condition in microchannels with *MF* equivalent to that of the control, i.e. 2 mm tall microchannel samples under a 48 hr feeding interval and 3) the open culture control, i.e. fluorodish samples under a 48 hr feeding interval. The morphology of the cells is shown in **Figure 3.10A** with MAP2 staining (green) overlaid with the phase contrast images. The insets show the overlaid MAP2 and nuclei staining. MAP2 staining was obvious only in the 50 μm samples, but not the other two. The expression of MAP2 peaked at week 2 and decreased at week 3.

The quantitative analysis of MAP2 staining is shown in Figure **3.10B-3.10D** together with that of the β-tubulin-III staining. The 50 μm microchannel samples demonstrated higher level of differentiation than the control (**Figure 3.10B**) marked by MAP2 and β-

tubulin-III expression (with * above, *p* range from 0.0001 to 0.007) while both biomarkers demonstrated cells in the 2000 μm microchannels to be comparable to the control (*p* range from 0.66 to 0.96). When neuronal cells were counted by positive MAP2staining and neurite outgrowth greater than twice of the cell body, the dependence of neuronal cell density on the culture condition were comparable to the findings from β-tubulin-III staining (**Figure 3.10C**). MAP2 staining showed initiation, peak and degeneration of neuronal differentiation in the 50 μm microchannels similar to β-tubulin-III staining. The neurite length determined from MAP2 positive cells was found to be mostly comparable to the control at the same week, consistent with the results from β-tubulin-III staining (**Figure 3.10D**). However, the number of neurites in the MAP2 stained samples was not large enough to carry out ANOVA analysis (groups labeled with NA below brackets). The comparable staining results of MAP2 and β-tubulin-III support our method of identifying differentiated neuronal cells by β-tubulin-III staining.

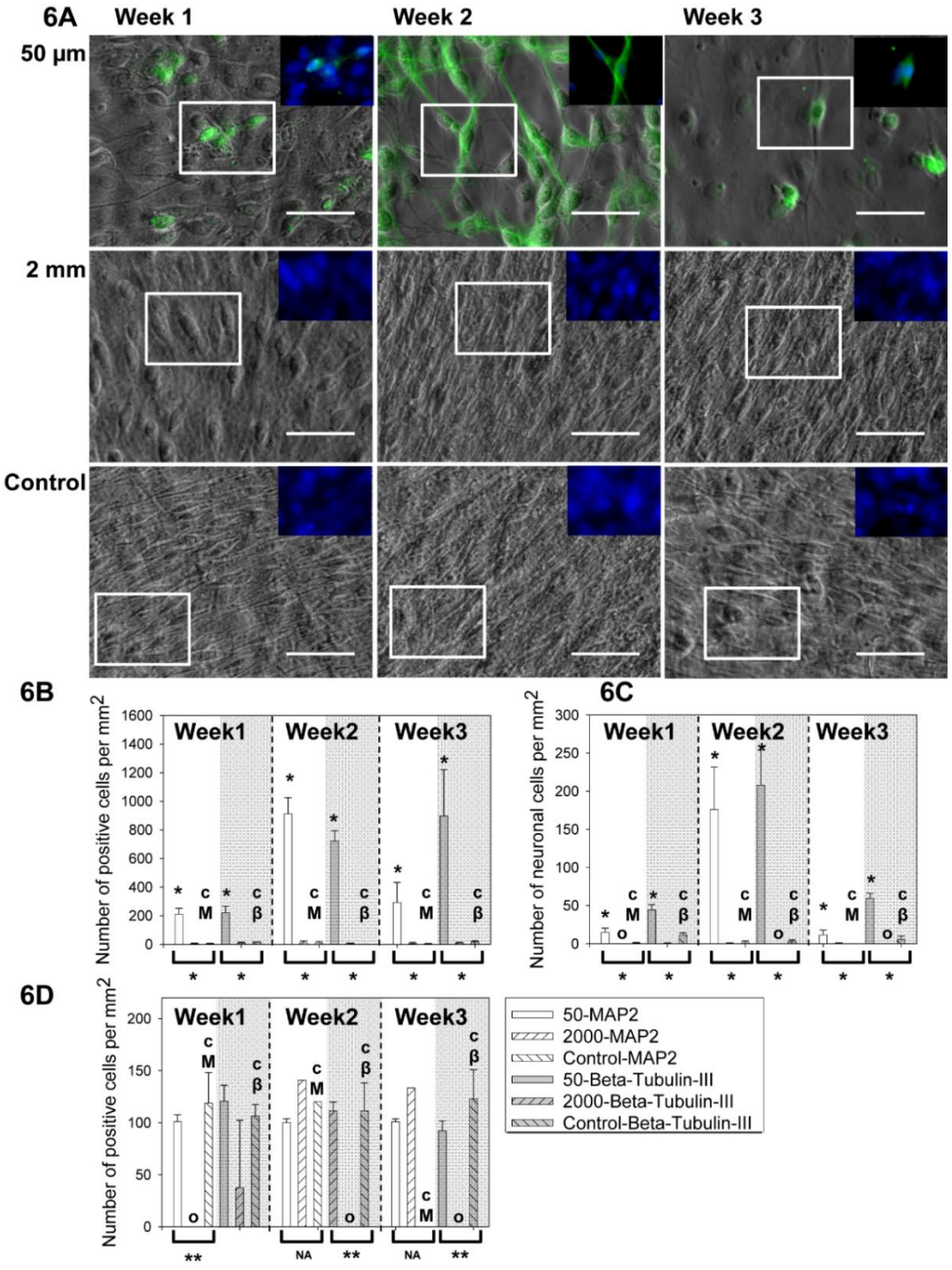

Figure 3.10: C17.2 cells behavior characterized by MAP2 staining. (A) The morphology of cells shown as overlaid phase contrast and MAP2 staining images. Green: MAP2.

Blue: cell nuclei. Scale bar=50 μm. The insets of MAP2 and cell nuclei staining were from the boxed region and were at the same scale as the main images. (B) MAP2 and β-tubulin-III (gray shades) positive cell counts per mm^2 over three weeks. Both staining showed similar trend of cell differentiation versus test conditions. (C) The neuronal cell count per mm^2 over time determined by cell morphology plus MAP2 or β-tubulin-III (gray shades) staining. (D) The average neurite length per mm^2 over time with positive MAP-2 or β-tubulin-III (gray shades) staining. The controls (with "cM" for MAP2 control and "cβ" for β-tubulin-III control) were C17.2 NSCs seeded at the same surface density in FluoroDishes but without microchannels and fed every 48 hours as in standard subculture protocols. Bars with "O" in Figure C and Figure D indicated that no cell was identified as a neuronal cell. Data were shown as mean ± standard deviation. The * above the bars indicated a statistical difference between the sample and the control by two-tailed Student's t test (p <0.05). The */** below the bars indicated a statistical difference in the group by the one-way ANOVA test (p <0.05). The ** in Figure D indicated a significant difference due exclusively to the samples with no neurite outgrowth. The groups labeled with NA below the brackets did not have enough number of neurites for ANOVA analysis. N≥15. Reprinted with permission from *Maintenance and neuronal cell*

differentiation of neural stem cells C17.2 correlated to medium availability sets design criteria in microfluidic systems. [39] Copyright: © 2014 Wang et al.

3.3.8 Correlation of the MF to Neuronal Cell Differentiation

To quantify the average amount of medium available to cells over time, the *MF* was introduced, which is the amount of culture medium available to each cell (cell number from initial seeding) divided by the feeding interval.

As summarized in the heat maps in **Figure 3.11**, experiment groups with low *MF*s (top right corner of each graph) were often associated with more prominent neuronal cell differentiation marked by more cells with positive β-tubulin-III staining (red) and more neuronal cells (green) than groups with high *MF*s (lower left corner of each graph). The neurite length is mostly ~100 μm except for those without observable neurite outgrowth (marked with a cross in the last panel of **Figure 3.11**).

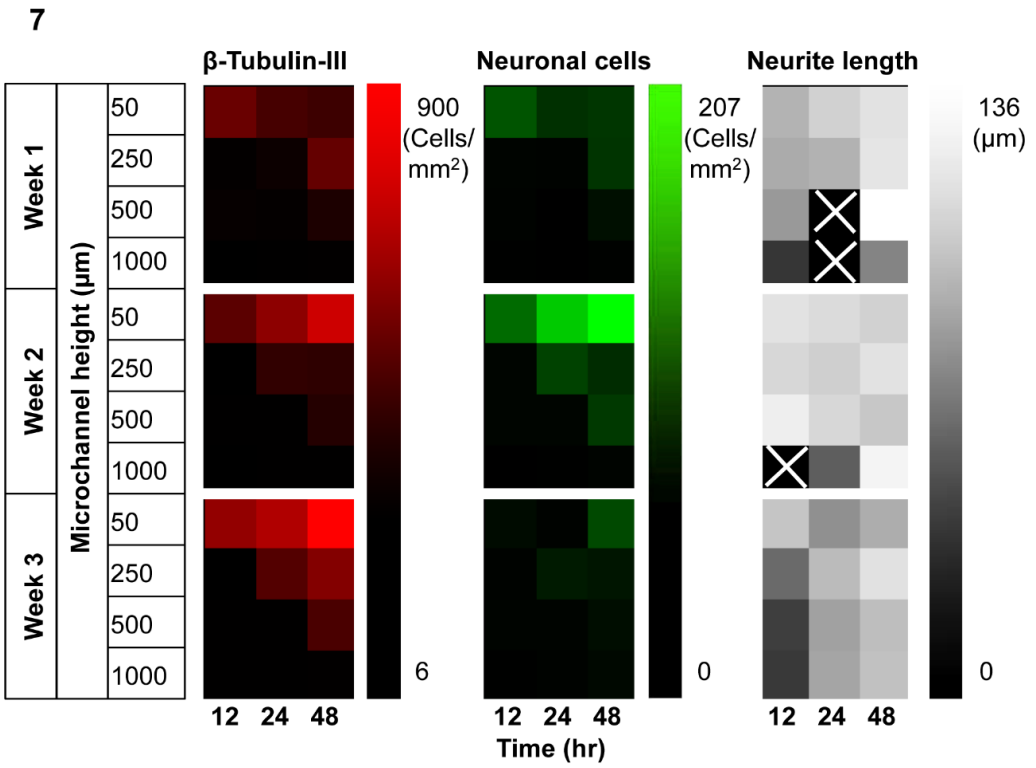

Figure 3.11: Summary of cell phenotypes with microchannel heights of 50 μm to 1000 μm and feeding frequencies of 12 hours to 48 hours. Groups with small *MF*s (towards top right corner of each graph) generally had more obvious neuronal cell differentiation as demonstrated by brighter colors representing higher density of cells with positive β-tubulin-III staining and neural morphology (first and second columns). The neurite length (third column), however, did not seem to have a strong correlation with the *MF*. The samples without noticeable neurite outgrowth were marked with a cross sign. Reprinted with permission from Maintenance and neuronal cell differentiation of neural stem cells

C17.2 correlated to medium availability sets design criteria in microfluidic systems. 32

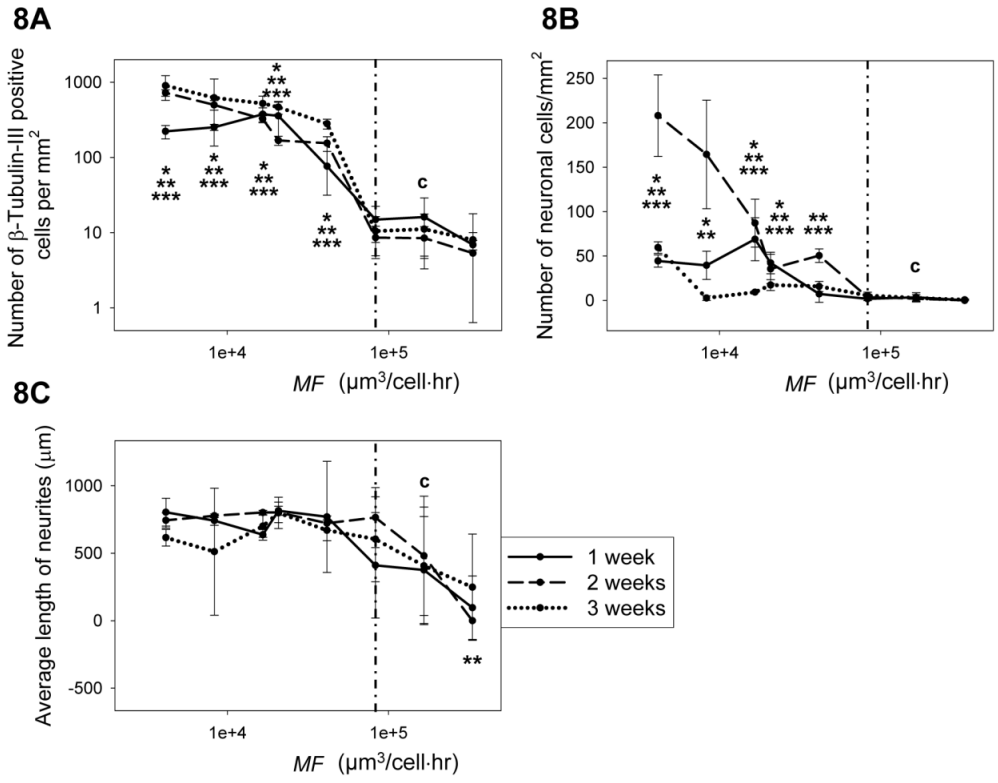

Figure 3.12: Correlation between *MF* and neuronal cell differentiation. (A) Samples with *MF* number smaller than 8.3×10^4 μm^3/cell·hour had significantly higher numbers of β-tubulin-III positive cells than that of the control. Samples with *MF* numbers equal to or larger than 8.3×10^4 μm^3/cell·hour had similar β-tubulin-III positive cell population compared to the control. (B) Samples with *MF*s smaller than 8.3×10^4 μm^3/cell·hour generally had significantly higher numbers of neuronal cells while samples with *MF*s

equal to or larger than 8.3×10^4 μm^3/cell·hour were mostly comparable to the control. (C) The average neurite length had minimal correlation with the *MF*. The control (with "c") was C17.2 NSCs seeded at the same surface density in FluoroDishes but without microchannels and fed every 48 hours as in standard subculture protocols. In all data points, N≥15. * indicates statistical difference compared to the control after 1 week, ** for 2 weeks and *** for 3 weeks ($p < 0.05$). The vertical dash line represents the critical *MF* of 8.3×10^4 μm^3/cell·hour. Reprinted with permission from Maintenance and neuronal cell differentiation of neural stem cells C17.2 correlated to medium availability sets design criteria in microfluidic systems. 32 Copyright: © 2014 Wang et al.

Statistical analysis was carried out to quantitatively investigate the correlation between *MF* and neuronal cell differentiation. *MF* values of all experiment groups were calculated and data sets were re-organized based on their *MF* values. As shown from the relatively tight error bars in most data points in **Figure 3.12**, the parameter *MF* is the dictating factor that controls the behavior of C17.2 in standard culture media. The critical *MF* of 8.3×10^4 μm^3/cell·hr is indicated by the vertical dash line in Figure 8. The control is labeled with "c". Demonstrated in **Figure 3.12A**, samples with *MF* smaller than 8.3×10^4 μm^3/cell·hr had significantly larger numbers of β-tubulin-III positive cells than that of the

control (*p* values range from 7×10^{-15} to 0.0004). Samples with *MF* numbers equal or greater than 8.3×10^4 μm^3/cell·hr had similar β-tubulin-III positive cell population compared to the control (*p* values range from 0.1 to 0.8). This correlation held true over the entire experiment course of 3 weeks (* indicates statistical difference compared to the control after 1 week, ** for 2 weeks and *** for 3 weeks). The number of neuronal cells also correlated well with the *MF* (**Figure 3.12B**). Samples with *MF*s smaller than 8.3×10^4 μm^3/cell·hr generally had significantly higher numbers of neuronal cells (*p* range from 5×10^{-13} to 0.013) while samples with *MF* equal to or greater than 8.3×10^4 μm^3/cell·hr were comparable (*p* values range from 0.1 to 1) to the control. Out of 24 data sets, only 2 fell out of this correlation, i.e. at *MF*=41,500 μm^3/cell·hr at week 1 (*p*=0.28) and *MF*=8,300 μm^3/cell·hr at week 3 (*p*=0.9). These two outliers were likely a result of time-dependent uprising and degeneration of the neuronal cell population over time. When further examining the morphological change of cells over time, an almost pure neuronal cell population of high density was observed at week two for groups with *MF* of 8.3×10^3 μm^3/cell·hr or smaller. On the other hand, the average neurite length mostly remained unchanged with the *MF* (**Figure 3.12C**) regardless of the level of spontaneous differentiation. Thus, the *MF* is a parameter that can be used to predict spontaneous

neuronal cell differentiation in standard culture medium for C17.2 NSCs, while the neurite length is not strongly controlled by the *MF*.

While the microfluidic culture introduced a few differences from conventional culture, including the exposure to shear stress, presence of PDMS and rate of nutrient depletion, the nutrient availability seemed to be the main contributor to the observed spontaneous differentiation. In our preliminary studies of short term culture, we demonstrated that leachant from PDMS, if present, did not induce higher C17.2 differentiation than the control of conventional culture. In addition, the optimal shear stress to maintain C17.2 NSCs was found to be around 0.004 Pa. This shear stress is within the range normally experienced by NSCs *in vivo*. [142] NSCs in their natural physiological environment experience shear stress generated by interstitial flow, which falls into the range of 0.01 to 0.001Pa. [142–144,148–150] Thus the flow condition used in the study is not expected to be detrimental to the NSCs. C17.2 cells cultured in the 2mm-thick channel showed comparable or even lower spontaneous differentiation when compared to the conventional static culture, indicating the shear condition used here did not contribute to the enhanced differentiation in the thinner channels. Thus, the correlation of the cell

phenotype with the *MF* demonstrates that *MF* is the major contributor to the observed high levels of spontaneous differentiation in thin devices or long feeding intervals.

Our observation of spontaneous neuronal cell differentiation under low *MF* is consistent with reports in the literature from *in vivo* studies: in response to nutrient depletion and the resulting damage in the neural network, NSCs go through neuronal cell differentiation in an effort to repair the damage. [86,96,97,124–129] Nutrient depletion by serum withdrawal is also the predominant method to induce neuronal differentiation of C17.2 NSCs *in vitro*. [130–132,141,151]

Although it is difficult to predict or determine the molecular source that contributes to the process, the observed critical *MF* suggests that the key molecules should have been consumed and reached a critically low concentration to induce spontaneous differentiation. For example, epidermal growth factor (EGF) may be an important player in neuronal cell differentiation: stem cell culture medium contains 10 ng/ml EGF while differentiation medium contains no EGF. [95,152–156] Based on the *MF* threshold, the consumption rate of EGF is predicted to be greater than 3.5×10^{-23} mol/s·cell. This prediction is consistent with experimental measurements that places consumption rate of EGF at 3.4×10^{-22} mol/s·cell for a fast EGF consuming cell model A431 epidermoid

carcinoma cells. [157] Thus, the *MF* threshold identified here may offer insight about the consumption rates of key chemicals involved in neuronal cell differentiation.

As observed in all the samples showing NSC differentiation, the neuronal cell population experienced a dynamic process of growth, peak and degeneration over the 3 week culture period. Although neurons are terminally differentiated cells and cannot proliferate, [158–162] primary neurons are capable of surviving *in vitro* culture for weeks. [32,120,147] The fast degeneration of the spontaneously differentiated neuronal cells in the case described herein may be caused by two possible reasons: an unfavorable environment to maintain neuronal cells and lack of an integrated neuronal cell network that is often required for long-term neuronal survival *in vitro*. The culture medium and feeding pattern was optimized for culturing NSCs instead of neuronal cells. Although neuronal cells can differentiate spontaneously from NSCs through nutrient consumption, maintaining them might require medium adjustment as neural apoptosis can be induced by a variety of stimuli such as growth factor concentration change and glucose concentration change. [163–172] Additionally, neurons are much more sensitive to shear stress than NSCs, thus cell feeding through laminar flow may damage the neuronal cells. [32,43,120,156,173–177] The other possible cause is immaturity of neural network. The protocols to induce NSC

differentiation (C17.2 cells and others) and maintain the resulting neuronal cells usually require chemical stimuli concurrent with nutrient depletion. [86,92,130–132,139,141,154,178] These stimuli promote the formation of dopaminergic neurons and neural communication, which are key to their integration in certain areas of the brain. [84–87,92,94,97,161] The neuronal cells formed in this study by nutrient consumption alone may lack the proper cues to integrate into a network, thus degenerate soon after differentiation.

While the cell population and nutrient availability are widely different in this study, the neurite outgrowth length appears consistent in majority of the test conditions. It has been reported that when using the same differentiation method, the length of neurites is characteristic of the physical environment. Curley et al. have reported characteristic neurite length of differentiated C17.2 NSCs on materials of different elasticity. [179] Yang et al. have used complex environmental physical cues to control both the neurite length and orientation of differentiated C17.2 NSCs. [180] The consistency of neurite outgrowth length observed in this study is likely a result of comparable physical exposures in all microfluidic samples, while the biochemical cues from nutrient restriction don't seem to play a key in neurite development after initiating NSC differentiation.

Despite the observed degeneration of differentiated neuronal cells, the β-tubulin-III positive cell population generally maintained a steady growth in our study, even after neuronal degeneration. This was a result of an emerging cell population with flattened morphology and multiple radially extended unbranched short processes in week 3. These morphological characteristics are consistent with those of intermediate cell types between NSCs and neurons. [181,182] While β-tubulin-III is often used an early neural marker, [183–185] any neuron-restricted progenitor cell type between the NSC phase and differentiated post-mitotic neuron phase could express β-tubulin-III. [186–188] The continuous proliferation of the intermediate cells kept the β-tubulin-III positive cell on the rise, [155,181,189–193] however, they were incapable of replacing the degenerated neuronal cells in the culture environment studied here. Our observation suggests different signals and culture environments may be required for the branched differentiation pathways from C17.2 NSCs to neuronal cells and from intermediate cells to neuronal cells.

3.4 Conclusions

The optimum conditions including substrate chemistry and flow conditions to maintain C17.2 NSC culture in microfluids has been determined by short term culture. Exposure to long term periodic shear stress in microfluidics does not induce neural differentiation of

C17.2 NSC. The *MF* successfully predicts the outcome of C17.2 NSCs in standard culture medium. The *MF* smaller than 8.3×10^4 μm^3/cell·hour causes spontaneous neuronal cell differentiation marked by a higher density of cells with positive β-tubulin-III or MAP2 staining and neural morphology than the control. On the other hand, minimal spontaneous neuronal cell differentiation is observed when the *MF* is equal to or larger than 8.3×10^4 μm^3/cell·hour. The average neurite length does not have a strong correlation with the *MF*. The *MF* can be controlled by several experimental factors such as cell density, cell medium volume and feeding time interval to maintain the stem cell status of C17.2 NSCs or to induce various levels of neuronal cell differentiation. Thus, the findings offer guidelines to microfluidic system design for controllable NSC maintenance and differentiation.

Chapter 4

Enhancement of Surface Binding by Laser Heating Induced Mass Transport

4.1. Motivation

Specific and efficient interactions between analyte and an affinity surface are key to the performance of biosensors and microarrays. [194–198] Many microsensors utilize diffusion as the sole transport mechanism and analyte consumption by the surface reaction can dominate diffusive feeding, resulting in diffusion limited reactions. To overcome this limit and improve the rate and equilibrium level of surface binding, various strategies have been devised to improve the mass transport. Continuous feeding is a popular option to replenish analyte near the capture bed when it can be afforded. [55,199,200] For example, Squires *et al.* compared the performance characteristics of biosensors with and without tangential flow and found faster sensor saturation with advection. [201] Yanik *et al.* modeled mass transport by flow to a nanohole based plasmonic sensor and discovered that a 14-fold improvement over diffusive transport would compensate reaction induced depletion zones. [202] However, continuous feeding generally consumes a lot of analyte and is not be applicable for precious samples. Alternatively, Hart *et al.* used AC

electroosmosis to increase mass flux to an IgG detector and observed an enhancement of fluorescent antibody binding up to 6.7 times, along with a reduction of reaction equilibrium time by up to a factor of 6. [203] Sigurdson *et al.* obtained a 7 fold sensitivity increase in an antibody sensor by electrothermal stirring. [204] However, these methods require patterned electrodes and risk potential electrochemical reactions at the electrode-solution interface. Enhanced mass transport and local concentration enhancement has also been achieved using acoustic radiation pressure. This method offers the flexibility of instantly changing the accumulation location, but suffers from the requirement of elaborate device fabrication. [205] Optical tweezers have been shown to enhance analyte concentration next to a biosensor by several orders of magnitude, but biomolecules and nano-vesicles often don't have considerable refractive index difference from the surrounding solution necessary for efficient tweezing. [206,207]

Recently, a number of research papers reported molecular accumulation in a solution driven by a temperature gradient. [208–211] The phenomena has been proposed as plausible mechanism to explain the origin of life, [211] and has been used to study colloid interfacial thermodynamics and biomolecule interactions. [209,212] The temperature gradient generates two transport effects in addition to diffusion: thermophoresis of solutes along or against

the temperature gradient and recirculation by natural advection. Together, the three transport processes create a non-uniform concentration distribution, and the concentration factor is controllable by the Soret coefficient, temperature gradient and reactor geometry. [208] Inspired by these studies, this work explores if a mild temperature gradient can enhance binding of ligand on an affinity surface. Compared to other methods, temperature gradients can be imposed on a reaction chamber remotely, saving the effort to fabricate electrodes and actuators into the reactor. Furthermore, a mild temperature range of 0-37°C is compatible with biological samples. [212,213] Compared to continuous feeding of analyte, temperature gradients induce recirculation and promote mass transport without wasting precious samples.

Various strategies have been implemented to create temperature gradients. Miniaturized vessels are often used to promote a strong gradient with a mild temperature variation. Mao *et al.* generated a linear temperature gradient across microfluidic channels by placing them between hot and cold water reservoirs. [214] Guijt *et al.* used endothermic and exothermic reactions as the heat source and drain. [215] However, the temperature gradient is gentle in these setups due to a significant temperature drop in the vessel walls. It is also challenging to maintain a temporal stability of the gradient in the later setup as the heat

source and sink equilibrate. Joule heating has been shown to offer more precise spatial and temporal control of temperature. [216] For example, Vigolo *et al.* encapsulated silver in the epoxy wall of a microvessel for resistive heating. [217] Although the temperature gradient is stable and adjustable, the device fabrication is complicated. Recently, Braun and Libchaber reported the use of a laser to generate temperature gradients in microchambers. This setup allows remote temperature control with precision spatial and temporal resolution, requires no fabrication in the microchamber itself and is compatible with in situ optical microscopy. [210,216] Given these advantages, we employed laser heating in a microchamber for transport enhancement and studied affinity binding on the functionalized floor. COMSOL simulations and dimensional analysis were used first to reveal the contribution of different transport processes on the surface binding kinetics and steady state surface concentration. Afterwards, the binding of biotinylated nanoparticles to NeutrAvidin-immobilized substrates were studied experimentally to validate the improvement predicted by the computational analysis. [218,219]

4.2. Materials and Methods

4.2.1 Simulation of Surface Binding

Two-dimensional simulations were performed using COMSOL Multiphysics software, a commercial finite element package (COMSOL Inc., Burlington, MA). The dimension of the microwell and the starting bulk concentration of nanoparticles were varied as listed in Table 4.1.

Starting bulk concentration (nM)	0.05, 0.5, 5
Width of microwell (μm)	100, 200, 300, 400, 500
Height of microwell (μm)	5, 15, 50, 150, 300, 500

Table 4.1. List of variables used in the COMSOL simulation

For the simple case of surface reactions without a temperature gradient, the analyte diffusivity was set to be $1.4 \times 10^{-12}\ m^2/s$, corresponding to diffusivity of nanoparticles used in the experiments (Supplemental I). The density and viscosity parameters of water at 293 K were selected from the COMSOL materials library. Using the *Surface Reactions* module, surface binding was stimulated as a second-order reaction with a forward rate constant $k_f = 2 \times 10^5\ m^3/mol \cdot s$, a value corresponding to the biotin and NeutrAvidin interaction. [220] The reverse rate constant for the NeutrAvidin-Biotin interaction is $4 \times 10^{-4}\ /s$, which is small and was neglected. [220] A lower $k_f = 1\ m^3/mol \cdot s$ was used in

a few cases to demonstrate slow surface reactions and these cases are noted in the paper. The bulk concentration of analyte at t = 0 was varied from 0.05 nM to 5 nM (consistent with the detection range of most ELISA kits), and the density of surface binding sites at t = 0 was fixed at $1 \times 10^{-8}\ mol/m^2$. [221]

To simulate surface binding in microwells with a temperature gradient, the *Heat Transfer in Solids* module was used and temperature at the top center of the microwell was set at 303 K. The sidewalls and floor of the microwell were set at room temperature of 293 K. Thermophoresis was simulated using codes from Braun *et al.* with the *Coefficient Form PDE* module. [210] The thermodiffusion coefficient for the analyte, D_T, was set at $7 \times 10^{-13}\ m^2/s \cdot K$ according to the literature for polystyrene beads. [208] The *Laminar Flow* module was used to simulate heat induced advection. Parameters (density, heat capacity, viscosity and thermal conductivity) of water were selected from the COMSOL materials library. The surface reaction was set up the same way as described above using the *Surface Reactions* module.

In both simulation setups, mass flux at the boundaries were set to be zero except for the reaction surface where reacted bulk species became surface species.

4.2.2 Dimensional Analysis

Dimensional analysis was carried out to understand relationships between different transport processes and their contributions to the surface reaction. The dominant transport mechanism among diffusion, advection and thermophoresis was analyzed first as a function of microwell dimension and analyte concentration. Afterwards, the transport flux to the reactive surface was compared to drain from the surface reaction. It was assumed in the analysis that surface reaction equilibrated slowly enough that bulk depletion evolved quasi-steadily, i.e. the mass transport could be described by a steady-state flux.

4.2.2.1 Dimensional Analysis of Transport Processes: Three mass transport processes were considered in this work in the presence of a temperature gradient: normal diffusion, natural advection and thermophoresis. The diffusive flux is defined as $J_D = -D\nabla C$. For scaling purposes, the gradient ∇C was approximated as a change in concentration divided by the distance *d* over which it changed. As the floor was uniformly reactive and the microwell height *H* was much less than the width *W* in most cases, *d* was on the order of *H.* Assuming that the targets were instantly captured upon encountering the surface and remained bound indefinitely, the concentration change was from C_0 in the bulk to a

near-surface concentration of 0. Thus, we obtained the diffusive flux $J_D \sim C_0 D/H$ and characteristic diffusion time $\delta_D \sim H^2/D$.

For natural advection driven by the temperature gradient, the advective flux $J_A \sim C_0 u$, where u is the average magnitude of velocity of natural advection. The value u was extracted from COMSOL simulation in this work. The characteristic advection time was calculated as $\delta_A \sim H/u$, since microwell height *H* was much less than the width *W* in most cases, and was used as the characteristic length.

The thermophoretic flux is defined as $J_T = CD_T \nabla T$. With the shallow and relatively wide microchamber dimension, the temperature difference of ΔT dropped over a length scale on the order of H, so that the initial thermophoretic flux $J_T \sim C_0 D_T \Delta T/H$ and the characteristic thermophoresis time $\delta_T \sim H^2/D_T \Delta T$.

Three non-dimensional parameters comparing the transport processes were defined as below:

$$Pe_{adv/diff} = \frac{Advective\ Transport\ Rate}{Diffusive\ Transport\ Rate} = \frac{\delta_D}{\delta_A} = Hu/D$$

$$R_{therm/diff} = \frac{Thermophoretic\ Transport\ Rate}{Diffusive\ Transport\ Rate} = \frac{\delta_D}{\delta_T} = D_T \Delta T/D$$

$$R_{adv/therm} = \frac{Advective\ Transport\ Rate}{Thermophoretic\ Transport\ Rate} = \frac{\delta_T}{\delta_A} = Hu/D_T \Delta T$$

In the absence of a temperature gradient, analyte were transported to the reactive surface by diffusion only. The enhanced transport in the presence of a temperature gradient was expressed as:

$$R_{(therm+adv)/diff} = \frac{Thermophoretic\ Transport\ Rate + Advective\ Transport\ Rate}{Diffusive\ Transport\ Rate}$$

$$= \frac{\delta_D}{\delta_A} + \frac{\delta_D}{\delta_T} = (Hu + D_T \Delta T)/D$$

4.2.2.3 Dimensional Analysis of Transports and Surface Reactions: For the reaction of analyte binding to an affinity surface, the reactive flux can be written as:

$$J_R = k_f bC - k_r C_S$$

where the forward rate constant is k_f, reverse rate constant is k_r, concentration of unreacted surface binding sites is b, bulk concentration is C and the concentration of surface species is C_S. Given the high affinity of the simulated receptor-ligand pair, desorption was neglected. The reactive flux was simplified to $J_R = k_f bC$. For scaling purposes, the initial reactive flux $J_R \sim k_f b_0 C_0$ and the characteristic reaction time $\delta_R \sim H/k_f b_0$.

In the microwell with a uniform temperature, the Damköhler number was calculated as:

$$Da = \frac{Reaction\ Rate}{Diffusive\ Transport\ Rate} = \frac{\delta_D}{\delta_R} = k_f b_0 H/D$$

In the microwell with a temperature gradient:

$$Da = \frac{Reaction\ Rate}{Combined\ Transport\ Rate} = \frac{1}{\delta_R(1/\delta_D+1/\delta_A+1/\delta_T)} = k_f b_0 H/(D + Hu + D_T\Delta T)$$

4.2.3 Experimental Setup

The experiments were carried out on a modified confocal microscope (Olympus, PA). The microchamber has a dimension of 50 μm × 5 mm × 5 mm. An IR laser (1064 nm) was introduced above the sample and was focused on the ceiling. The temperature gradient was calibrated using 50 mM 2',7'-bis-(2-carboxyethyl)-5-(and-6)-carboxyfluorescein (BCECF, Life Technologies, CA) in a 10 mM Tris buffer (Sigma Aldrich, WI). The fluorescence intensity of BCECF drops by 2.8% in response to an increase of 1 K in temperature. [208,211,222] The temperature calibration was carried out by changing the input laser power and recording the corresponding fluorescence intensity on the ceiling as shown in Supplementary II: Temperature calibration. Images in all experiments were processed by software FV-10-ASW (Olympus, PA) and analyzed by ImageJ (National Institutes of Health).

4.2.3.1 Microwell Fabrication and Surface Treatment

A mixture of PDMS prepolymer and curing agent at a weight ratio of 10:1 (Sylgard 184, Dow-Corning, MI) was spin-coated on a coverslip (2" × 3", thickness #1, Ted Pella, CA) at 500 rpm for 5 min. The resulting PDMS film of 50 μm thickness was cured on the coverslips at 65-75 ℃ overnight, and a square hole was cut in PDMS to create a 50 μm × 5 mm × 5 mm reaction chamber.

To functionalize the floor of the microwell, the devices were activated by oxygen plasma and submerged sequentially in the following solutions: 4% (v/v) solution of 3-mercaptopropyl trimethoxysilane (Gelest, PA) in ethanol for 1 hour at room temperature, 0.01 μmol/mL N-gamma-Maleimidobutyryl-oxysulfosuccinimide ester (GMBS, Pierce Protein, IL) in ethanol for 1 hour at room temperature, and finally 10 μg/mL NeutrAvidin (Pierce Protein, IL) in phosphate buffered saline (PBS, Sigma Aldrich, WI) for at least 1 h at 4 ^{o}C. Immediately before use, the microwells were blocked by 1% (w/v) bovine serum albumin (BSA, Sigma Aldrich, WI) in PBS for at least 15 min and blot dry. The control devices were functionalized similarly except for 0 μg/mL NeutrAvidin in PBS.

4.2.3.2 Calibration of Fluorescence Intensity from Surface Binding

AF488- biotin -labeled polystyrene nanoparticles (Life Technologies, CA) 200 nm in diameter were suspended in deionized water, sonicated for 20 min in an ice water bath

and used immediately. To yield a proper range of surface nanoparticles density for calibration, nanoparticles suspensions of 0.004, 0.013, 0.04, 0.13 and 0.4 nM were used. Two microliter of nanoparticles suspension was pipetted into the functionalized microwell, and the microwell was capped with a coverslip (1" × 1", Fisher Scientific, PA). The surface of the coverslip in contact with the suspension was coated with 200 nm chromium to mimic the condition used in the temperature gradient experiments. The nanoparticle suspension was allowed to react in the microwell for 75 minutes and the fluorescence intensity on the microwell floor was recorded using a confocal microscope. Afterwards the microwell was washed 3 times with deionized water, air dried and coated with iridium for scanning electron microscope (SEM) imaging. The number of nanoparticles per unit area (100 μm^2) was counted from the SEM images. Non-specific binding was characterized using BSA passivated microwells without NeutrAvidin and nanoparticles at a concentration of 0.04 nM. For each condition, 3 samples were used for repeats; for each sample, 3 images were taken at random locations for both the fluorescence and SEM measurements. All data sets in graphs are presented as average ± standard deviation from 9 data points.

4.2.3.3 Kinetics of Surface Binding without Temperature Gradients

To monitor the kinetics of surface binding without a temperature gradient, 2 μL of the nanoparticle suspension at 0.04 nM was allowed to react in a microwell covered by a chromium coated coverslip. The fluorescence intensity at the microwell floor was recorded every 5 minutes until the reaction reached a steady state. Then the average fluorescence intensity in each frame was converted to a surface concentration using the calibration curve described above. For each condition, 3 samples were used for repeats. All data sets in graphs are presented as average ± standard deviation from 3 repeats.

4.2.3.4 Kinetics of Surface Binding with Temperature Gradients

To record the kinetics of surface binding with a temperature gradient, 2 μL of the nanoparticle suspension at 0.04 nM was pipetted into a functionalized microwell. Immediately after capping the microwell with a chromium-coated coverslip, an IR laser (1064nm) was focused on the chromium ceiling to generate local heating 10K above room temperature. The fluorescence intensity on the microwell floor was recorded every 5 min until the reaction reached a steady state. To analyze the resulting accumulation ring, the radially distributed fluorescence intensity was measured. Since the highest intensity usually occurred at 20-30 μm from the center, fluorescence intensity from this region was averaged to obtain maximum surface binding. To verify that the accumulation

ring was from surface binding rather than physical accumulation in the bulk, the heating laser was turned off after the reaction completed. The fluorescence intensity profile showed a minimal change, which confirmed that the particles were not free to diffuse anymore and were surface-bound. For each condition, 3-5 samples were used for repeats. All data sets in graphs are presented as average ± standard deviation from more than 3 repeats.

4.3. Results and Discussion

Figure 4.1 shows the COMSOL simulation result of a microwell with 5 mm × 5 mm footprint and various well heights (5 μm, 15 μm, 50 μm, 150 μm, 300 μm to 500 μm) used for the capture of 200 nm nanoparticles. The bulk concentration of nanoparticles and surface concentration of receptors are the same in all cases at t=0, and the surface receptor concentration is sufficient to deplete all nanoparticles even in the deepest microwell studied here of 500 μm. Reaction rate constants corresponding to the NeutrAvidin-biotin pair are used. **Figure 4.1A** demonstrates the binding kinetics on the surface: to account for the difference in the total amount of analyte available, the surface concentration is normalized to the height of microwells. As the reverse rate constant is negligible for the NeutrAvidin-biotin reaction, all reactions reach equilibrium when the

analyte is exhausted in the microwells. The height normalized surface concentration thus all plateaus at the same level. The reaction half-life (time required for the surface concentration to reach half of the equilibrium concentration) is then extracted and plotted against the microwell heights in **Figure 4.1B** (dots). As the height of the microwells increases stepwise from 5 μm to 500 μm, the reaction half-life increases significantly from 6 s to 12 hrs. The half-life scales with the square of the microwell heights (line in **Figure 4.1B**), and the prefactor is on the same order as $1/2D$, with D being the diffusion coefficient of the analyte. Since the microwell height is the characteristic length in most geometries studied here (wide and shallow wells), this relationship suggests that surface binding is diffusion limited despite microscale reactions. Diffusion limited reactions are also confirmed by dimensional analysis of the Damköhler number, which is on the order of 10^3 to 10^5 for the different chamber heights studied here.

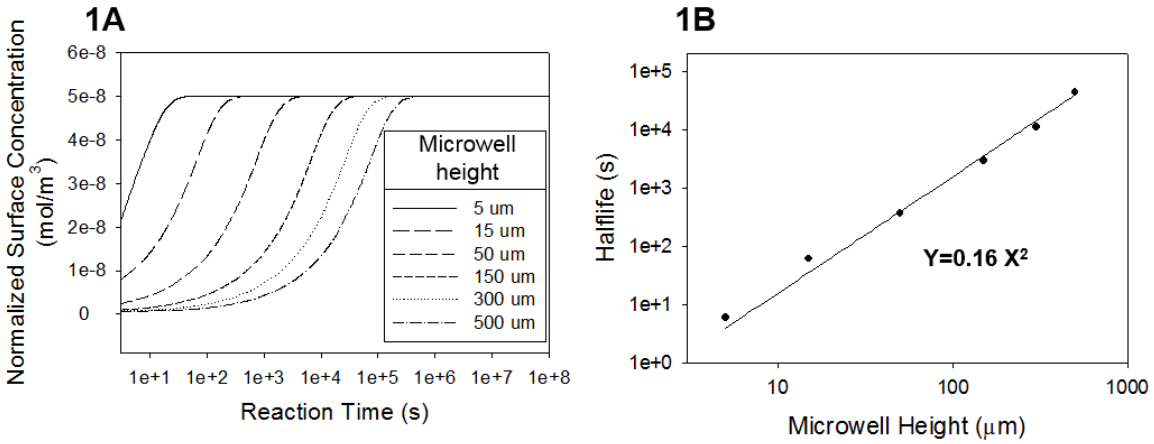

Figure 4.1: COMSOL simulation of binding of biotinylated 200 nm nanoparticles to surface immobilized NeutrAvidin in microwells with footprints of 500 μm × 500 μm and heights of 5 μm, 15 μm, 50 μm, 150 μm, 300 μm and 500 μm respectively. *(A)* Surface binding kinetics normalized to the height of microwells show a red shift with the depth of the microwells. *(B)* The reaction half-life (time required for the surface concentration to reach half of the equilibrium concentration, plotted as dots) scales with the square of the microwell height (solid line), suggesting the reactions are diffusion limited.

To overcome the diffusion limit, we introduce a temperature gradient to the reaction reservoir, which creates two additional transport processes, thermophoretic migration of the analyte and natural advection. In the COMSOL simulation, temperature at the center of the microwell ceiling is set at 303 K, 10 K higher than the ambient of 293 K. We first examined the dependence of natural advection on the microwell heights (5 μm, 15 μm, 50 μm, 150 μm, 300 μm and 500 μm while the width is fixed at 500 μm) and widths (100 μm, 200 μm, 300 μm, 400 μm and 500 μm while the height is fixed at 50 μm). As shown in **Figure 4.2A**, the average velocity of advection increases mildly from 5.3×10^{-8} m/s to 1.9×10^{-7} m/s as the width of the microwells increases from 100 μm to 500 μm, indicating limited benefit to mass transport. On the other hand, the average velocity

changes dramatically from 1.2 × 10^{-11} m/s to 1.3 × 10^{-5} m/s as the height of the microwells increase from 5 μm to 500 μm (**Figure 4.2B**). This is understandable since the Rayleigh number scales with the cube of the characteristic length. In our study where the height of the microwell is never larger than the width of the microwell, the characteristic length is mostly controlled by the height.

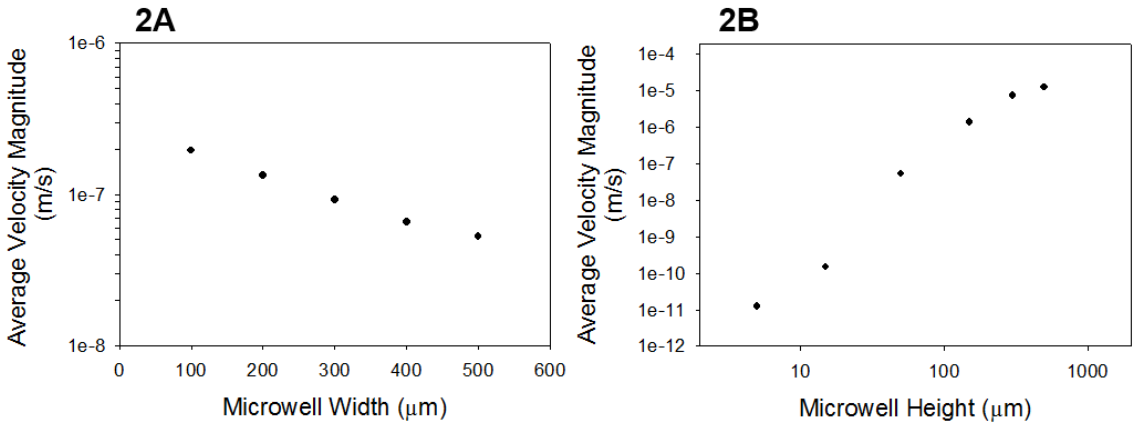

Figure 4.2: COMSOL simulation of average velocity in microwells with various widths and heights. *(A)* The average velocity in microwells with a fixed height of 50 μm, but varied footprint widths of 100 μm, 200 μm, 300 μm, 400 μm and 500 μm respectively. Mild increases in velocity indicate limited benefits to mass transport. *(B)* The average velocity in microwell with a fixed footprint width of 500 μm but varied heights of 5 μm, 15 μm, 50 μm, 150 μm, 300 μm and 500 μm. Significant changes in velocity indicate a pronounced benefit to convective mass transport.

In addition to controlling the magnitude of natural advection, the microwell height also influences the temperature gradient, which drives thermophoresis of analyte to the reactive surface. Since the microwell height is much less than the width in most cases, and the glass floor has much higher heat conductivity than water, the microwell height is considered the characteristic length for temperature gradient scaling. The thermophoretic flux to the reactive surface scales linearly with the temperature gradient, while the later decreases with the chamber height. Thus, the thermophoretic and advective fluxes have opposite dependence on the chamber height.

To compute the relative contribution of the three transport processes, ratios of the transport rates are calculated and shown in **Figure 4.3A** as a function of microwell heights and average advective velocities. $Pe_{adv/diff}$ represents the ratio of advective transport rate relative to diffusive transport rate; $R_{adv/therm}$ represents advective transport rate relative to thermophoretic rate; $R_{therm/diff}$ represents thermophoretic rate relative to diffusive transport rate. $R_{(therm+adv)/diff}$ represents the combined transport rate driven by the temperature gradient (thermophoresis and natural advection) relative to diffusive on transport rate. The temperature gradient is found to promote transport in all geometries ($R_{(therm+adv)/diff} > 1$). The enhanced transport is initially contributed

predominantly by thermophoresis ($R_{adv/therm} < 1$ when $H < 60$ μm) and later by natural advection ($R_{adv/therm} \geq 1$ when $H \geq 60$ μm). In the advection dominant region, $R_{(therm+adv)/diff}$ increases dramatically from 151.1 to 4535.7 when the microwell height increases from 60 to 500 μm. On the other hand, it remained relatively constant (5.0 – 6.9) in the thermophoresis dominated region.

To compare the reactive flux against the combined transport flux, Damköhler number (Da) is presented as a function of microwell heights and advection velocities (**Figure 4.3B**). In the absence of the temperature gradient, Da increases continuously with the microwell height (empty circles). On the other hand, the plot of Da versus the microwell height demonstrates a bell shape curve when the temperature gradient is present (solid dots). This can be interpreted by inspecting the equation derived in the section of *Dimensional Analysis of Transports and Surface Reactions*:

$$Da = k_f b_0 H/(D + Hu + D_T \Delta T)$$

As the microwell height increases, diffusive and thermophoretic fluxes go down but the advective flux increases. In the region where thermophoresis dominates or $R_{adv/therm} < 1$ (left of the dash line in **Figure 4.3B**), the combined fluxes by diffusion and thermophoresis (relating to term $C_0(D/H + D_T \Delta T/H)$) decreases faster than the increase

of the advective flux (relating to term $C_0 u$). Therefore a net increase of Da is observed. In the advection dominated region where $R_{adv/therm} > 1$, the opposite is true, leading to a rapid drop of Da. In all cases, $Da \gg 1$, so the reaction is transport limited even with the temperature gradient, but Da is reduced by 1 – 4 orders of magnitude compared to the uniform temperature reactions (**Figure 4.3B**, empty dots).

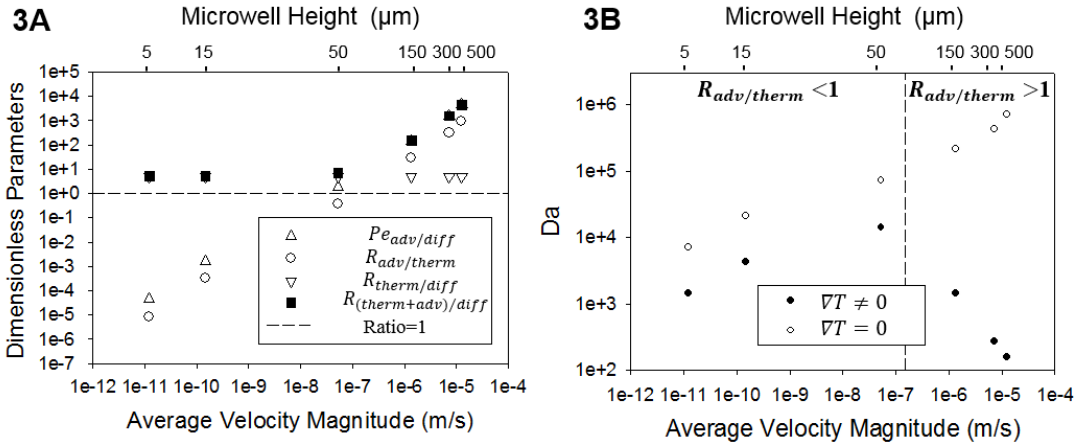

Figure 4.3: Dimensional analysis of transport and reaction fluxes as a function of microwell height (top axis) and average advection velocity (bottom axis). *(A)* Dimensionless groups characterizing the transport processes. $Pe_{adv/diff}$ is the ratio of advective transport rate relative to diffusion transport rate; $R_{adv/therm}$ is the advective transport rate relative to thermophoretic transport rate; $R_{therm/diff}$ is the thermophoretic transport rate relative to diffusion transport rate; $R_{(therm+adv)/diff}$ is the combined transport rate driven by the temperature gradient (thermophoresis and natural

advection) relative to diffusion transport rate. The dash line indicates a ratio of 1. *(B)* The Damköhler number Da measuring the reaction rate relative to the combined transport rate. In the presence of the temperature gradient, a bell shape curve is observed, while a monotonic increase of Da with the microwell height is seen without the temperature gradient.

As a result of transport enhancement by the temperature gradient, the reaction rate and maximum surface binding are improved (**Figure 4.4**). When thermophoresis is the dominating transport mechanism ($R_{adv/therm} < 1,\ H < 60\mu m$), the half-life is reduced by ~50% compared to reactions with a homogeneous temperature (**Figure 4.4A** and **Figure 4.4B**). This is a result of comparable fluxes by thermophoresis and diffusion. In the advection dominated region ($R_{adv/therm} \geq 1,\ H \geq 60\mu m$), the half-life of reactions with temperature gradients still increases with the chamber height, but at a much slower rate than that at a homogeneous temperature. Thus the half-life ratio decreases with the chamber height. In the 500 μm tall microwell, the half-life is drastically reduced from 12 hrs to 36 min. Such an improvement of reaction rate is not surprising, since velocity of natural convection scales with higher power of the chamber height than diffusion does, which significantly reduces the diffusion limit.

Furthermore, the temperature gradient leads to uneven distribution of the surface bound analyte and an accumulation ring is observed. **Figure 4.4C** demonstrates a snapshot of the simulated concentration distribution in bulk (top of **Figure 4.4C**) and on the surface (bottom of **Figure 4.4C**) in a 50 μm tall microwell 2 min after the reaction. The color corresponds to the concentration. The non-uniform concentration results from a combined effect of thermophoresis and advection: (1) Thermophoresis pushes nanoparticles away from the heat source and towards the sides and bottom of the microwell. (2) Vortices generated by natural convection sweep nanoparticles on the microwell floor towards the center. While the fluid recirculates up near the center, the particles experience thermophoretic repulsion against the temperature gradient and accumulate on the floor. Bulk accumulation of DNA into a ring shape has been observed by Braun *et al.* [210] using a similar setup but no affinity substrate. Such non-uniform bulk distribution further translates into analyte enrichment on the surface.

When the maximum surface concentration at the steady state is normalized to the chamber height (**Figure 4.4D**), the accumulation is found to increase with the chamber height in the presence of the temperature gradient. In the absence of the temperature gradient, the normalized equilibrium surface concentration remains constant due to

uniform surface coverage. As a result, enhancement of surface binding, represented by the ratio of maximum surface concentration at the steady state with to without temperature gradients (**Figure 4.4E**), increases steadily with the chamber height.

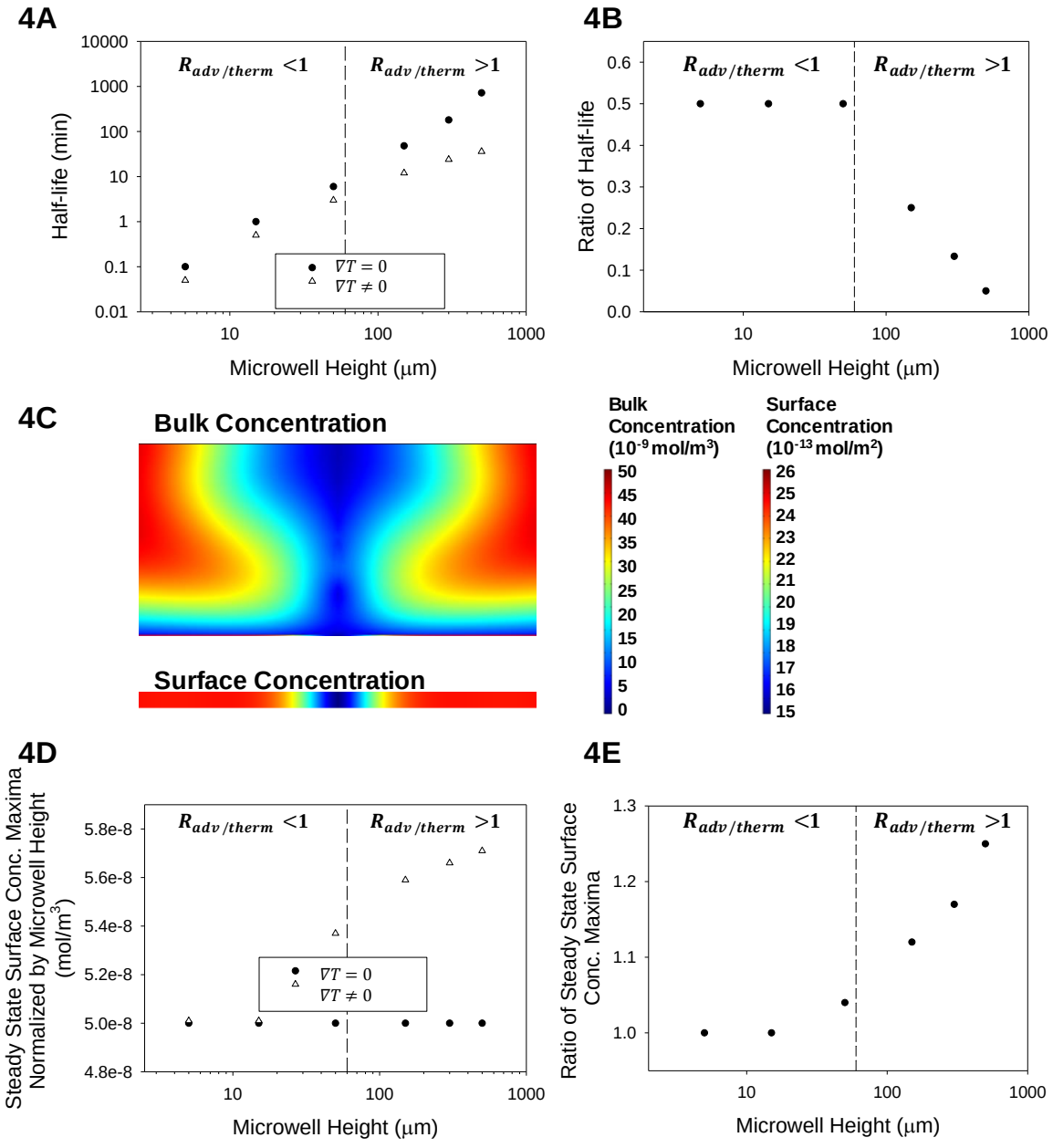

Figure 4.4: Simulated improvements of the reaction rate and steady state surface binding by superposing temperature gradients on microwells of various heights. Reaction constants corresponding to the NeutrAvidin-biotin pair were used. *(A)* Half-life of 200nm nanobeads reacting with affinity surfaces in microwell with ($\nabla T \neq 0$) and without ($\nabla T = 0$) temperature gradients. *(B)* The ratio of half-lives (half-lives of reactions with the temperature gradient divided by those without the temperature gradient) shows 50% reduction in the thermophoresis dominated region ($R_{adv/therm} < 1$). The ratio decreases with the chamber height in the advection dominated region ($R_{adv/therm} > 1$). *(C)* Simulated bulk concentration and surface concentration in a 50 μm tall microwell with a 10 K temperature elevation at the top center. A warmer color indicates a higher concentration. *(D)* Maximum surface concentration at the steady state normalized by microwell heights in microwells with ($\nabla T \neq 0$) and without ($\nabla T = 0$) temperature gradients. *(E)* Ratio of the steady state surface concentration maxima with a temperature gradient to those without a temperature gradient. Enhancement of steady-state surface accumulation is observed with the microwell height. In all graphs, the dashed line represents $R_{adv/therm} = 1$.

This surface accumulation becomes even more pronounced when the forward reaction rate constant is dropped from 2×10^5 $m^3/mol \cdot s$, a value corresponding to the NeutrAvidin-biotin interaction, to 1 $m^3/mol \cdot s$. The reverse reaction constant is neglected for simplicity and Da is 0.045, thus the reaction rate is the limiting step. **Figure 4.5A** and **Figure 4.5B** show the time course of surface concentration profile in the fast and slow reactions, respectively, and the same temperature gradient is present. The fast reaction generates an accumulation ring of binding. The depleted center is a result of thermophoretic repulsion pushing analyte outwards and fast depletion of analyte before it is convected to the center. On the other hand, the slower reaction produces peak accumulation in the center and the tight accumulation zone produces significantly higher surface accumulation. **Figure 54.C** shows the kinetic change of the peak surface concentration. The surface accumulation initially builds up slower with lower k_f but reaches a much higher level at the steady state. The ratio of the peak surface concentration with $\nabla T \neq 0$ to that with $\nabla T = 0$ at each time point is shown in Figure 5D for both slow and fast reactions. The ratio first increases with time in both reactions until the reaction with the temperature gradient approaches steady state. Afterwards, the surface concentration continues to increase in the microwell with a homogenous

temperature and the ratio starts to decrease. At the steady state, the ratio is > 4 times with the slow reaction in contrast to a mere 1.04 with the fast reaction. The much more enhanced surface accumulation in the slow reaction is not surprising: the analyte is less consumed out of the accumulation zone and natural convection continuous feed unreacted analyte to the center. In fact, Braun *et al.* [210] observed a 13-fold bulk accumulation at the steady state when DNA molecules were subjected to a temperature gradient of ~0.6K/μm (3 times higher than the value used here), with the thermodiffusion coefficient (D_T) and Soret coefficient (S_T) of DNA being comparable to the value used here.

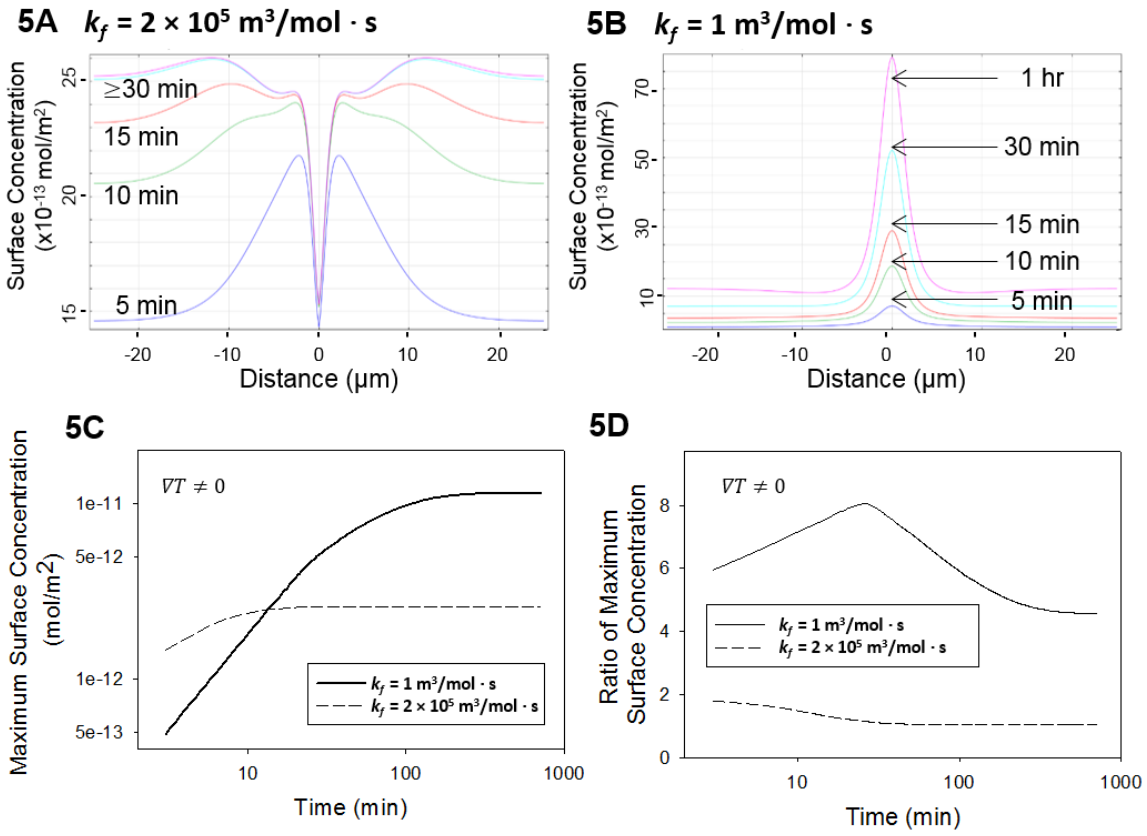

Figure 4.5: COMSOL simulation of surface binding with a fast ($k_f = 2 \times 10^5\ m^3/mol \cdot s$) and a slow ($k_f = 1\ m^3/mol \cdot s$) reaction. *(A)* Radially distributed concentration profile using the fast reaction model (k_f =2 × 10^5 m^3/mol · s) at different time points. *(B)* Radially distributed concentration profile using the slow reaction model (k_f =1 m^3/mol · s) at different time points. The depletion zone in the center disappears in the slow reaction *(B)* leading to greater accumulation. *(C)* Kinetic change of the peak surface concentration corresponding to the two forward reaction rate constants under the same

temperature gradient. *(D)* ∇T enhanced surface binding relative to that under a homogeneous temperature. The greatest improvement occurs when the reaction with the temperature gradient reaches a steady state.

The simulation results demonstrate that temperature gradient improves both the surface binding rate and maximum surface concentration through enhanced transport. To verify the simulated findings, we next carried out experiments using 200 nm biotinylated nanoparticles and microwells with a dimension of $5\ \text{mm} \times 5\ \text{mm} \times 50\ \mu\text{m}$ and a NeutrAvidin treated floor.

To quantify the concentration of surface bound species dynamically, fluorescence intensity was measured in real time on the floor of microwells using confocal microscopy. [210,223–225] The intensity was converted to a surface concentration through a calibration curve in **Figure 4.6**. The calibration curve was generated by allowing nanoparticles of various concentrations (0.004, 0.013, 0.04, 0.13 and 0.4 nM) to react in functionalized microwells for 75 min without laser heating, followed with measurements of fluorescence intensity on the microwell floor and SEM imaging of surface bound nanoparticle density. The reaction time is long enough to reach steady state in 50μm tall chambers. Control samples using 0.04 nM nanoparticles and BSA passivated microwells

without NeutrAvidin was also tested to estimate nonspecific binding on the floor. As shown in **Figure 4.6A**, NeutrAvidin functionalized substrates promotes specific targets binding, which leads to a measurable increase of the fluorescence intensity. **In Figure 4.6B**, the fluorescence intensity shows a linear regression towards the surface concentration of nanoparticles with good correlation ($R^2 = 0.9915$). For later experiments, 0.04 nM nanoparticles were used to make sure the density of surface bound targets is well within the linear detection range.

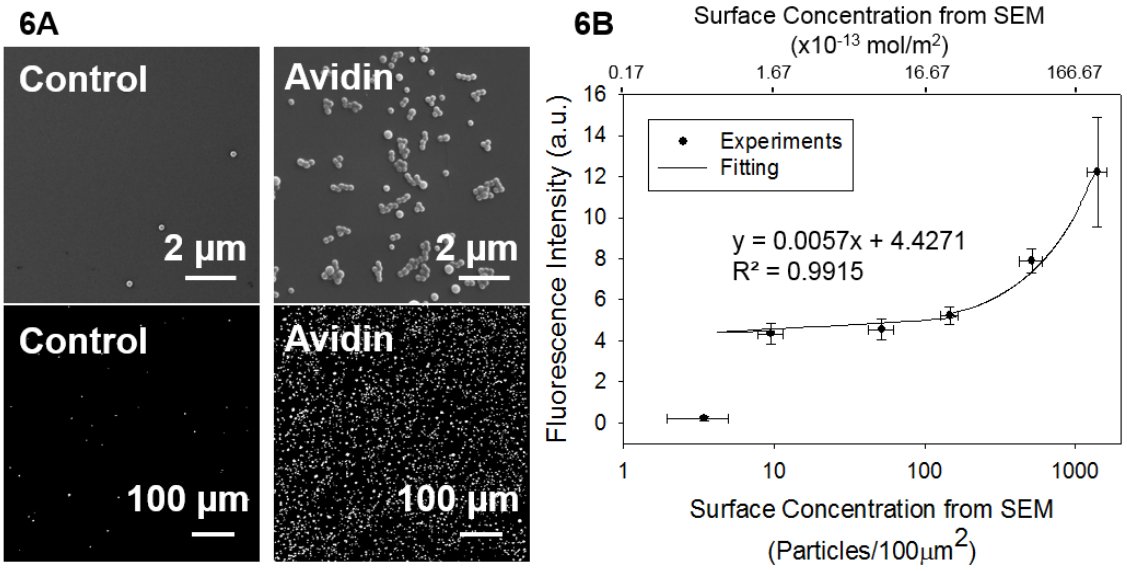

Figure 4.6: Calibration of the fluorescence intensity. A range of surface concentrations of nanoparticles were produced by reactions of nanoparticles at various concentrations with NeutrAvidin treated surfaces in microwells. The control was microwells with BSA passivation but no NeutrAvidin treatment. *(A)* Considerable difference is observed in

both SEM images (top panel) and fluorescence intensity (bottom panel) when 0.04 nM nanoparticles react in a control microwell versus a NeutrAvidin-treated microwell. *(B)* The fluorescence intensity shows a linear regression towards the surface concentration of nanoparticles with $R^2 = 0.9915$. The error bars represent one standard deviation (n=9).

Next we examined the surface binding kinetics in NeutrAvidin-functionalized microwells with and without laser heating. The laser generated a temperature 10 K higher than the ambient, confirmed ahead by BCECF fluorescence intensity measurements. The fluorescence intensity on the microwell floor due to nanoparticle binding was recorded every 5 min. The calibration curve in **Figure 4.6** was used to convert the intensity to a surface concentration. As shown in **Figure 4.7A**, the temperature gradient produces an accumulation ring on the microwell floor, consistent with the simulation prediction in **Figure 4.4C**. The radially distributed fluorescence intensity was extracted (**Figure 4.7B**) and the intensity from the peak location ± 5 μm was averaged to obtain the surface concentration in the accumulation zone with the temperature gradient. For comparison, the dynamic change of the surface fluorescence was also measured in microchambers without a temperature gradient. As shown in **Figure 4.7C**, the measured surface concentration (dots) well matches the simulated kinetics (lines). Initially, temperature

gradients generate higher surface binding in the accumulation zone than homogeneous temperature. The surface concentration in the laser heated chambers plateaus within 25 min, while the reaction under a homogeneous temperature continues and diminishes the difference between the two groups. This is consistent with the COMSOL simulation of reactions in a 50 μm tall microwell where the reaction half-life is reduced by half but the maximum surface binding is only enhanced 4% at the steady state (**Figure 4.4**).

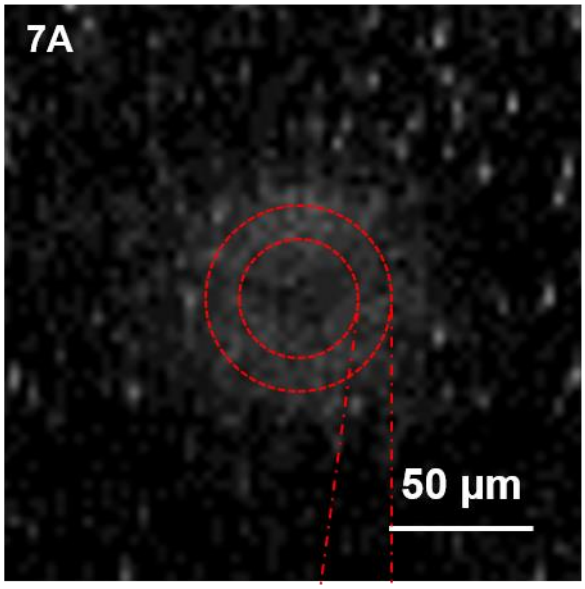
7A
50 µm

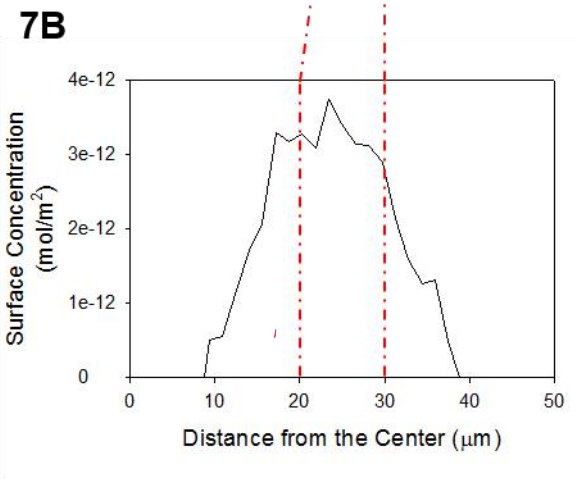
7B
Surface Concentration (mol/m2)
4e-12
3e-12
2e-12
1e-12
0
0
10
20
30
40
50
Distance from the Center (µm)

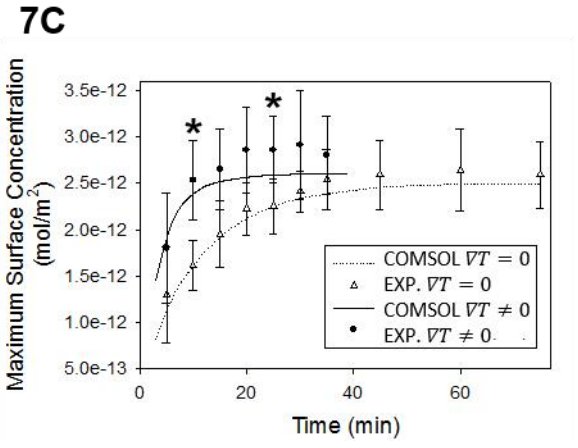
7C
Maximum Surface Concentration (mol/m2)
3.5e-12
3.0e-12
2.5e-12
2.0e-12
1.5e-12
1.0e-12
5.0e-13
0
20
40
60
Time (min)
COMSOL ∇T = 0
EXP. ∇T = 0
COMSOL ∇T ≠ 0
EXP. ∇T ≠ 0

Figure 4.7: Experimental measurements of surface binding with a temperature gradient or under a homogenous temperature. *(A)* A typical fluorescence intensity image 10 min after the reaction on the microwell floor when ∇T is present. *(B)* Radially averaged fluorescence intensity profile of Figure 4.7A. The average fluorescence intensity from the accumulation zone (peak location ± 5 μm, e.g. between the two circles in Figure 4.7A) was used to calculate maximum surface concentration. *(C)* Kinetics of peak surface concentration with (black dot) and without (empty triangle) temperature gradients. In the presence of a temperature gradient, the fluorescence intensity in the accumulation zone was averaged every 5 min from 3-5 different samples, and the error bars represent one standard deviation (n≥3). The solid line is from simulated reactions with a temperature gradient and dash line from simulated reactions with a uniform temperature. The experimental results are in good agreement with the prediction from COMSOL simulation. Statistically different data points in reactions with and without temperature gradients are labeled with "*" ($p < 0.05$ by two-tailed student *t* test).

While a mild temperature gradient has been shown to create non-uniform bulk accumulation, [208,210] we demonstrate here that both the binding kinetics and surface concentration can also be enhanced by the temperature gradient. Although the

improvement of steady-state surface binding appears only moderate using the fast NeutrAvidin and biotin interaction, combining a temperature gradient with a patterned affinity substrate is expected to limit analyte depletion out of the affinity region and promote much elevated local binding on a timely fashion. This is especially appealing for micro- and nanosensors where diffusive transport of analyte to a miniaturized binding area can be unrealistically long in a dilute solution.[201,226] As a moderate temperature gradient is biocompatible and can be superposed on a microchamber, it has the potential to be integrated with micro- and nanosensors without added complexity to the sensors themselves. It is also highly plausible to array the heating source for microarray applications.

Conclusions

In conclusion, introducing a mild temperature gradient to a microwell reactor enhances mass transport and promotes surface binding. COMSOL simulation and dimensional analysis show that the enhanced transport is due to combined effects of thermophoresis and natural advection, and the relative contribution of each process is dependent on the microwell dimension. The benefits to the binding kinetics increases with the microchamber height. The steady state surface binding is non-uniform in the presence of

the temperature gradient, and the accumulation is more obvious for slow reactions. The simulation prediction is confirmed experimentally with one selected microwell geometry. The strategy to enhance surface binding through a temperature gradient can be applied to improve the sensitivity and time response of biosensors and microarrays.

Chapter 5

Concluding Remarks and Future Outlooks

5.1 Concluding Remarks

This dissertation delivers solutions to *in vitr*o isolation, culture, differentiation of cells and biomolecule detection in microfluidics. It improves state-of-the-art understanding of microfluidic systems in 1) utilizing nanotography for cell isolation using flatbed immunoaffinity devices; 2) maintaining and controllably differentiating stem cells; and 3) employing a mild temperature to enhance immunoaffinity detection of cell secretion molecules.

In *Chapter 2*, it was demonstrated cell isolation in microfluidics can be achieved and further enhanced by systematically studying the relationship between capture efficiency and surface roughness using carefully controlled surface nanotopography with the Jurkat cells as a model system. The conditions to significantly enhance immunoaffinity cell capture under continuous flow were identified. The potential mechanisms of the non-monotonic relationships between the capture efficiency and surface roughness were examined. This work will enable more rational design of cell capture devices.

In *Chapter 3*, it was demonstrated stem cells can be successfully maintained and differentiated in a controllable manner in microfluidics using the neural stem cell line C17.2 as a model system. The optimum conditions including substrate chemistry and flow conditions to maintain C17.2 NSC culture in microfluids has been determined by short term culture. Long term culture revealed that neural differentiation of C17.2 NSCs was not influenced by shear stress generated by feeding in microfluidics, but was influenced by the nutrient depletion level. A medium factor (*MF*) was used to characterize the relationship between neural differentiation and the amount of medium available to cells over time. The findings in this chapter offer guidelines to microfluidic system design.

In *Chapter 4*, enhancing the detection of molecules secreted by cells has been successfully achieved using the biotin-avidin pair as a model system. Introducing a mild temperature gradient to a microwell reactor enhances mass transpot to facilitate reactions that are often limited by diffusion. The enhanced mass transport coming from a mild temperature gradient that induced thermophoresis and convection was demonstrated by COMSOL simulation, dimensional analysis and verified by experiments in 50 μm tall microwells with and without temperature gradient. The findings in this chapter will enable better design of microwell reaction chambers. The temperature gradient could potentially be

paired with other additional microfluidic features to further enhance the device's performance.

With the work in this dissertation, it has been demonstrated that an *in vitro* microfluidic cell analysis system can be developed with the patient's body fluids as input and the patient's health information as output. Research of important functions of the system including isolating cells of interest from patent's sample, maintaining the sample, further inducing differentiation of the cell sample and molecular analysis of the sample has been carried out. All functions have been successfully achieved and optimized in microfluidics. It is hoped with research in this dissertation, an easy, portable, low cost POC (point of care) microfluidic system can be developed and made available to people in need.

5.2 Future Outlooks

Further integration and automation. Current microfluidic systems often involve off-chip sample preparation and/or analysis. Through further integration and automation of microfluidics involved in each step, one would hope to obtain one system capable of taking patient samples, isolating target cells of interest, preparing cells for analysis and performing DNA or molecular analysis. This would save time, reduce the risk of sample

loss or contamination, eliminate the need for bulky expensive equipment and significantly reduce the need for trained professionals to operate the device and enable microfluidics to be commercialized as potentially OTC (over-the-counter) products.

Bridging the gap between microfluidics and current research tools. Microfluidics, as the emerging technology, has found itself highly compatible with certain existing research tools such as SPR (surface plasmon resonance), time of flight imaging and AFM (atomic force microscopy) that benefit from small scales and a better controlled microenvironment. More research tools that have been developed for traditional larger scale studies, such as fluorescence microscopy, ELISA (enzyme-linked immunosorbent assay and flow cytometry, do not often match with microfluidic systems. Effort to adapt these technologies would further empower and offer more variety in microfluidics.

Chapter 6

References

(1) TELL, F.; BRADLEY, R. M. *J. Neurophysiol.* **1994**, *71*, 479–492.

(2) SPRINGER, T. A. *Cell* **1994**, *76*, 301–314.

(3) Levine, A. J. *Cell* **1997**, *88*, 323–331.

(4) Liu, X. S.; Kim, C. N.; Yang, J.; Jemmerson, R.; Wang, X. D. *Cell* **1996**, *86*, 147–157.

(5) Anderson, R. G. W. *Annu. Rev. Biochem.* **1998**, *67*, 199–225.

(6) STEARNS, T.; KIRSCHNER, M. *Cell* **1994**, *76*, 623–637.

(7) Cua, D. J.; Sherlock, J.; Chen, Y.; Murphy, C. a; Joyce, B.; Seymour, B.; Lucian, L.; To, W.; Kwan, S.; Churakova, T.; Zurawski, S.; Wiekowski, M.; Lira, S. a; Gorman, D.; Kastelein, R. a; Sedgwick, J. D. *Nature* **2003**, *421*, 744–748.

(8) Reubi, J. C. *Endocr. Rev.* **2003**, *24*, 389–427.

(9) Kalos, M.; Levine, B. L.; Porter, D. L.; Katz, S.; Grupp, S. A.; Bagg, A.; June, C. H. *Sci. Transl. Med.* **2011**, *3*.

(10) Wootton, R. C. R.; Fortt, R.; de Mello, A. J. *Org. Process Res. Dev.* **2002**, *6*, 187–189.

(11) Jahnisch, K.; Hessel, V.; Lowe, H.; Baerns, M. *Angew. CHEMIE-INTERNATIONAL Ed.* **2004**, *43*, 406–446.

(12) Sia, S. K.; Whitesides, G. M. *Electrophoresis* **2003**, *24*, 3563–3576.

(13) Hong, J. W.; Studer, V.; Hang, G.; Anderson, W. F.; Quake, S. R. *Nat. Biotechnol.* **2004**, *22*, 435–439.

(14) Vilkner, T.; Janasek, D.; Manz, A. *Anal. Chem.* **2004**, *76*, 3373–3385.

(15) Aoki, J.; Serruys, P. W.; van Beusekom, H.; Ong, A. T. L.; McFadden, E. P.; Sianos, G.; van der Giessen, W. J.; Regar, E.; de Feyter, P. J.; Davis, H. R.; Rowland, S.; Kutryk, M. J. B. *J. Am. Coll. Cardiol.* **2005**, *45*, 1574–1579.

(16) Dharmasiri, U.; Balamurugan, S.; Adams, A. A.; Okagbare, P. I.; Obubuafo, A.; Soper, S. A. *Electrophoresis* **2009**, *30*, 3289–3300.

(17) Wang, S.; Wang, H.; Jiao, J.; Chen, K.-J.; Owens, G. E.; Kamei, K.; Sun, J.; Sherman, D. J.; Behrenbruch, C. P.; Wu, H.; Tseng, H.-R. *Angew. CHEMIE-INTERNATIONAL Ed.* **2009**, *48*, 8970–8973.

(18) Hughes, A. D.; King, M. R. *LANGMUIR* **2010**, *26*, 12155–12164.

(19) Han, W.; Allio, B. A.; Foster, D. G.; King, M. R. *ACS Nano* **2010**, *4*, 174–180.

(20) Scheper, T.; Kumar, A.; Galaev, I. Y.; Mattiasson, B. *Cell Separation: Fundamentals, Analytical and Preparative Methods*; 2008; Vol. 106.

(21) Sethu, P.; Sin, A.; Toner, M. *Lab Chip* **2006**, *6*, 83–89.

(22) Pratt, E. D.; Huang, C.; Hawkins, B. G.; Gleghorn, J. P.; Kirby, B. J. *Chem. Eng. Sci.* **2011**, *66*, 1508–1522.

(23) Kuntaegowdanahalli, S. S.; Bhagat, A. A. S.; Kumar, G.; Papautsky, I. *Lab Chip* **2009**, *9*, 2973–2980.

(24) Chien, Y. S.; Lin, C. H.; Kao, F. J.; Ko, C. W. In *PROGRESS ON ADVANCED MANUFACTURE FOR MICRO/NANO TECHNOLOGY 2005, PT 1 AND 2*; Jywe, W and Chen, CL and Fan, KC and Fung, RF and Hanson, SG and Hsieh, WH and Hsu, CL and Huang, YM and Hwang, YL and Jager, G and Jeng, YR and Li, W and Liao, YS and Lin,, CC and Lin, ZC and Sung, CK and Tzeng, CH, Ed.; MATERIALS SCIENCE FORUM; TRANS TECH PUBLICATIONS LTD: BRANDRAIN 6, CH-8707 ZURICH-UETIKON, SWITZERLAND, 2006; Vol. 505-507, pp. 643–648.

(25) Applegate, R. W.; Squier, J.; Vestad, T.; Oakey, J.; Marr, D. W. M.; Bado, P.; Dugan, M. A.; Said, A. A. *Lab Chip* **2006**, *6*, 422–426.

(26) Qu, B.-Y.; Wu, Z.-Y.; Fang, F.; Bai, Z.-M.; Yang, D.-Z.; Xu, S.-K. *Anal. Bioanal. Chem.* **2008**, *392*, 1317–1324.

(27) Kim, H. J.; Huh, D.; Hamilton, G.; Ingber, D. E. *Lab Chip* **2012**, *12*, 2165–2174.

(28) Huh, D.; Fujioka, H.; Tung, Y.-C.; Futai, N.; Paine, R.; Grotberg III, J. B.; Takayama, S. *Proc. Natl. Acad. Sci. U. S. A.* **2007**, *104*, 18886–18891.

(29) Wang, P.-Y.; Tsai, W.-B.; Voelcker, N. H. *ACTA Biomater.* **2012**, *8*, 519–530.

(30) Chung, B. G.; Choo, J. *Electrophoresis* **2010**, *31*, 3014–3027.

(31) Lin, F.; Nguyen, C. M. C.; Wang, S. J.; Saadi, W.; Gross, S. P.; Jeon, N. L. *Ann. Biomed. Eng.* **2005**, *33*, 475–482.

(32) Chung, B. G.; Flanagan, L. A.; Rhee, S. W.; Schwartz, P. H.; Lee, A. P.; Monuki, E. S.; Jeon, N. L. *Lab Chip* **2005**, *5*, 401–406.

(33) Shin, H.; Mahto, S. K.; Kim, J.-H.; Rhee, S. W. *BIOCHIP J.* **2011**, *5*, 214–219.

(34) Halldorsson, S.; Lucumi, E.; Gómez-Sjöberg, R.; Fleming, R. M. T. *Biosens. Bioelectron.* **2015**, *63*, 218–231.

(35) Van Midwoud, P. M.; Janse, A.; Merema, M. T.; Groothuis, G. M. M.; Verpoorte, E. *Anal. Chem.* **2012**, *84*, 3938–3944.

(36) Wang, L.; Murthy, S. K.; Barabino, G. A.; Carrier, R. L. *Biomaterials* **2010**, *31*, 7586–7598.

(37) Freshney, R. I. In *Culture of Animal Cells: A Manual of Basic Technique and Specialized Applications*; 2010.

(38) Kim, L.; Toh, Y.-C.; Voldman, J.; Yu, H. *Lab Chip* **2007**, *7*, 681–694.

(39) Wang, B.; Jedlicka, S.; Cheng, X. *PLoS One* **2014**, *9*.

(40) Kapur, S.; Baylink, D. J.; Lau, K. H. W. *Bone* **2003**, *32*, 241–251.

(41) Park, J. Y.; Kim, S. K.; Woo, D. H.; Lee, E. J.; Kim, J. H.; Lee, S. H. *Stem Cells* **2009**, *27*, 2646–2654.

(42) Yim, E. K. F.; Pang, S. W.; Leong, K. W. *Exp. Cell Res.* **2007**, *313*, 1820–1829.

(43) Yang, F.; Murugan, R.; Wang, S.; Ramakrishna, S. *Biomaterials* **2005**, *26*, 2603–2610.

(44) Rivet, C.; Lee, H.; Hirsch, A.; Hamilton, S.; Lu, H. *Chem. Eng. Sci.* **2011**, *66*, 1490–1507.

(45) Huebner, A.; Srisa-Art, M.; Holt, D.; Abell, C.; Hollfelder, F.; deMello, A. J.; Edel, J. B. *Chem. Commun.* **2007**, 1218–1220.

(46) Agrawal, A.; Zhang, C. Y.; Byassee, T.; Tripp, R. A.; Nie, S. M. *Anal. Chem.* **2006**, *78*, 1061–1070.

(47) Shi, M.; Peng, Y.; Zhou, J.; Liu, B.; Huang, Y.; Kong, J. *Biosens. Bioelectron.* **2006**, *21*, 2210–2216.

(48) Tsukagoshi, K.; Jinno, N.; Nakajima, R. *Anal. Chem.* **2005**, *77*, 1684–1688.

(49) Tai, L.-W.; Tseng, K.-Y.; Wang, S.-T.; Chiu, C.-C.; Kow, C. H.; Chang, P.; Chen, C.; Wang, J.-Y.; Webster, J. R. *Anal. Biochem.* **2009**, *391*, 98–105.

(50) Lee, K.-H.; Su, Y.-D.; Chen, S.-J.; Tseng, F.-G.; Lee, G.-B. *Biosens. Bioelectron.* **2007**, *23*, 466–472.

(51) Kurita, R.; Yokota, Y.; Sato, Y.; Mizutani, F.; Niwa, O. *Anal. Chem.* **2006**, *78*, 5525–5531.

(52) Hu, J.; Wang, T.; Wang, S.; Chen, M.; Wang, M.; Mu, L.; Chen, H.; Hu, X.; Liang, H.; Zhu, J.; Jiang, M. *PLoS One* **2014**, *9*.

(53) Yang, C. Y.; Brooks, E.; Li, Y.; Denny, P.; Ho, C. M.; Qi, F. X.; Shi, W. Y.; Wolinsky, L.; Wu, B.; Wong, D. T. W.; Montemagno, C. D. *Lab Chip* **2005**, *5*, 1017–1023.

(54) He, B.; Morrow, T. J.; Keating, C. D. *Curr. Opin. Chem. Biol.* **2008**, *12*, 522–528.

(55) Wang, B.; Weldon, A. L.; Kumnorkaew, P.; Xu, B.; Gilchrist, J. F.; Cheng, X. *LANGMUIR* **2011**, *27*, 11229–11237.

(56) Plouffe, B. D.; Radisic, M.; Murthy, S. K. *Lab Chip* **2008**, *8*, 462–472.

(57) Gomez-Sjoberg, R.; Morisette, D. T.; Bashir, R. *J. MICROELECTROMECHANICAL Syst.* **2005**, *14*, 829–838.

(58) Nagrath, S.; Sequist, L. V; Maheswaran, S.; Bell, D. W.; Irimia, D.; Ulkus, L.; Smith, M. R.; Kwak, E. L.; Digumarthy, S.; Muzikansky, A.; Ryan, P.; Balis, U. J.; Tompkins, R. G.; Haber, D. A.; Toner, M. *Nature* **2007**, *450*, 1235–U10.

(59) Du, Z.; Colls, N.; Cheng, K. H.; Vaughn, M. W.; Gollahon, L. *Biosens. Bioelectron.* **2006**, *21*, 1991–1995.

(60) Liu, Y.-J.; Guo, S.-S.; Zhang, Z.-L.; Huang, W.-H.; Baigl, D.; Xie, M.; Chen, Y.; Pang, D.-W. *Electrophoresis* **2007**, *28*, 4713–4722.

(61) Faley, S.; Seale, K.; Hughey, J.; Schaffer, D. K.; VanCornpernolle, S.; McKinney, B.; Baudenbacher, F.; Unutmaz, D.; Wikswo, J. P. *Lab Chip* **2008**, *8*, 1700–1712.

(62) Kotz, K. T.; Xiao, W.; Miller-Graziano, C.; Qian, W.-J.; Russom, A.; Warner, E. A.; Moldawer, L. L.; De, A.; Bankey, P. E.; Petritis, B. O.; Camp II, D. G.; Rosenbach, A. E.; Goverman, J.; Fagan, S. P.; Brownstein, B. H.; Irimia, D.; Xu, W.; Wilhelmy, J.; Mindrinos, M. N.; Smith, R. D.; Davis, R. W.; Tompkins, R. G.; Toner, M.; Injury, I. H. R. *Nat. Med.* **2010**, *16*, 1042–U142.

(63) Stott, S. L.; Hsu, C.-H.; Tsukrov, D. I.; Yu, M.; Miyamoto, D. T.; Waltman, B. A.; Rothenberg, S. M.; Shah, A. M.; Smas, M. E.; Korir, G. K.; Floyd Jr., F. P.; Gilman, A. J.; Lord, J. B.; Winokur, D.; Springer, S.; Irimia, D.; Nagrath, S.;

Sequist, L. V; Lee, R. J.; Isselbacher, K. J.; Maheswaran, S.; Haber, D. A.; Toner, M. *Proc. Natl. Acad. Sci. U. S. A.* **2010**, *107*, 18392–18397.

(64) Neurauter, A. A. Springer-Verlag Berlin, 2007.

(65) Hashimoto, M.; Kaji, H.; Nishizawa, M. *Biosens. Bioelectron.* **2009**, *24*, 2892–2897.

(66) Cheng, X.; Irimia, D.; Dixon, M.; Sekine, K.; Demirci, U.; Zamir, L.; Tompkins, R. G.; Rodriguez, W.; Toner, M. *Lab Chip* **2007**, *7*, 170–178.

(67) Tuttle IV, P. V; Rundell, A. E.; Webster, T. J. *Int. J. Nanomedicine* **2006**, *1*, 497–505.

(68) Kalasin, S.; Martwiset, S.; Coughlin, E. B.; Santore, M. M. *LANGMUIR* **2010**, *26*, 16865–16870.

(69) Kalasin, S.; Santore, M. M. *LANGMUIR* **2010**, *26*, 2317–2324.

(70) Santore, M. M.; Kozlova, N. *LANGMUIR* **2007**, *23*, 4782–4791.

(71) Wang, W.; Gu, B. H.; Liang, L. Y.; Hamilton, W. *J. Phys. Chem. B* **2003**, *107*, 3400–3404.

(72) Zhang, J. H.; Zhan, P.; Wang, Z. L.; Zhang, W. Y.; Ming, N. B. *J. Mater. Res.* **2003**, *18*, 649–653.

(73) Jiang, S. Recipes for St€ober Silica Particles http://mit.edu/sjiang2/www/Resources/stober_recipes.pdf.

(74) Kumnorkaew, P.; Ee, Y.-K.; Tansu, N.; Gilchrist, J. F. *LANGMUIR* **2008**, *24*, 12150–12157.

(75) S Tabatabaei, A Shukohfar, R. A. and A. M. In *Journal of Physics: Conference Series*; 2006.

(76) Huang, J.; Hu, G.; Orkoulas, G.; Christofides, P. D. *Chem. Eng. Sci.* **2010**, *65*, 6101–6111.

(77) Deng, J. D.; Schoenbach, K. H.; Buescher, E. S.; Hair, P. S.; Fox, P. M.; Beebe, S. J. *Biophys. J.* **2003**, *84*, 2709–2714.

(78) Lulevich, V.; Zink, T.; Chen, H.-Y.; Liu, F.-T.; Liu, G. *LANGMUIR* **2006**, *22*, 8151–8155.

(79) Majstoravich, S.; Zhang, J. Y.; Nicholson-Dykstra, S.; Linder, S.; Friedrich, W.; Siminovitch, K. A.; Higgs, H. N. *Blood* **2004**, *104*, 1396–1403.

(80) Singer, I. I.; Scott, S.; Kawka, D. W.; Chin, J.; Daugherty, B. L.; DeMartino, J. A.; DiSalvo, J.; Gould, S. L.; Lineberger, J. E.; Malkowitz, L.; Miller, M. D.; Mitnaul, L.; Siciliano, S. J.; Staruch, M. J.; Williams, H. R.; Zweerink, H. J.; Springer, M. S. *J. Virol.* **2001**, *75*, 3779–3790.

(81) AMIEVA, M. R.; FURTHMAYR, H. *Exp. Cell Res.* **1995**, *219*, 180–196.

(82) Pospieszalska, M. K.; Ley, K. *Cell. Mol. Bioeng.* **2009**, *2*, 207–217.

(83) Zhao, C. M.; Deng, W.; Gage, F. H. *Cell* **2008**, *132*, 645–660.

(84) Bjorklund, L. M.; Sanchez-Pernaute, R.; Chung, S. M.; Andersson, T.; Chen, I. Y. C.; McNaught, K. S.; Brownell, A. L.; Jenkins, B. G.; Wahlestedt, C.; Kim, K. S.; Isacson, O. *Proc. Natl. Acad. Sci. U. S. A.* **2002**, *99*, 2344–2349.

(85) Kim, J. H.; Auerbach, J. M.; Rodriguez-Gomez, J. A.; Velasco, I.; Gavin, D.; Lumelsky, N.; Lee, S. H.; Nguyen, J.; Sanchez-Pernaute, R.; Bankiewicz, K.; McKay, R. *Nature* **2002**, *418*, 50–56.

(86) Bjorklund, A.; Lindvall, O. *Nat. Neurosci.* **2000**, *3*, 537–544.

(87) Wernig, M.; Zhao, J. P.; Pruszak, J.; Hedlund, E.; Fu, D. D.; Soldner, F.; Broccoli, V.; Constantine-Paton, M.; Isacson, O.; Jaenisch, R. *Proc. Natl. Acad. Sci. U. S. A.* **2008**, *105*, 5856–5861.

(88) Nakatomi, H.; Kuriu, T.; Okabe, S.; Yamamoto, S.; Hatano, O.; Kawahara, N.; Tamura, A.; Kirino, T.; Nakafuku, M. *Cell* **2002**, *110*, 429–441.

(89) Chen, J. L.; Li, Y.; Wang, L.; Zhang, Z. G.; Lu, D. Y.; Lu, M.; Chopp, M. *Stroke* **2001**, *32*, 1005–1011.

(90) Arvidsson, A.; Collin, T.; Kirik, D.; Kokaia, Z.; Lindvall, O. *Nat. Med.* **2002**, *8*, 963–970.

(91) Snyder, E. Y.; Deitcher, D. L.; Walsh, C.; Arnoldaldea, S.; Hartwieg, E. A.; Cepko, C. L. *Cell* **1992**, *68*, 33–51.

(92) Liu, W. G.; Lu, G. Q.; Li, B. A.; Chen, S. D. *Parkinsonism Relat. Disord.* **2007**, *13*, 77–88.

(93) Yang, M.; Stull, N. D.; Berk, M. A.; Snyder, E. Y.; Iacovitti, L. *Exp. Neurol.* **2002**, *177*, 50–60.

(94) Ryu, M. Y.; Lee, M. A.; Ahn, Y. H.; Kim, K. S.; Yoon, S. H.; Snyder, E. Y.; Cho, K. G.; Kim, S. U. *Cell Transplant.* **2005**, *14*, 193–202.

(95) Akerud, P.; Canals, J. M.; Snyder, E. Y.; Arenas, E. *J. Neurosci.* **2001**, *21*, 8108–8118.

(96) Sinden, J. D.; RashidDoubell, F.; Kershaw, T. R.; Nelson, A.; Chadwick, A.; Jat, P. S.; Noble, M. D.; Hodges, H.; Gray, J. A. *Neuroscience* **1997**, *81*, 599–608.

(97) Zhu, J. M.; Zhao, Y. Y.; Chen, S. D.; Zhang, W. H.; Lou, L.; Jin, X. *J. Int. Med. Res.* **2011**, *39*, 488–498.

(98) Singh, A.; Suri, S.; Lee, T.; Chilton, J. M.; Cooke, M. T.; Chen, W. Q.; Fu, J. P.; Stice, S. L.; Lu, H.; McDevitt, T. C.; Garcia, A. J. *Nat. Methods* **2013**, *10*, 438 – +.

(99) Loewke, K. E.; Camarillo, D. B.; Piyawattanametha, W.; Mandella, M. J.; Contag, C. H.; Thrun, S.; Salisbury, J. K. *Ieee Trans. Biomed. Eng.* **2011**, *58*, 159–171.

(100) Solanki, A.; Chueng, S. T. D.; Yin, P. T.; Kappera, R.; Chhowalla, M.; Lee, K. B. *Adv. Mater.* **2013**, *25*, 5477–5482.

(101) Jung, D. J.; Minami, I.; Patel, S.; Lee, J.; Jiang, B.; Yuan, Q. H.; Li, L.; Kobayashi, S.; Chen, Y.; Lee, K. B.; Nakatsuji, N. *J. Nanobiotechnology* **2012**, *10*, 10.

(102) Cimetta, E.; Figallo, E.; Cannizzaro, C.; Elvassore, N.; Vunjak-Novakovic, G. *Methods* **2009**, *47*, 81–89.

(103) Park, J. Y.; Takayama, S.; Lee, S. H. *Integr. Biol.* **2010**, *2*, 229–240.

(104) Yu, H. M.; Meyvantsson, I.; Shkel, I. A.; Beebe, D. J. *Lab Chip* **2005**, *5*, 1089–1095.

(105) Cai, L.; Friedman, N.; Xie, X. S. *Nature* **2006**, *440*, 358–362.

(106) Warren, L.; Bryder, D.; Weissman, I. L.; Quake, S. R. *Proc. Natl. Acad. Sci. U. S. A.* **2006**, *103*, 17807–17812.

(107) Zhong, J. F.; Chen, Y.; Marcus, J. S.; Scherer, A.; Quake, S. R.; Taylor, C. R.; Weiner, L. P. *Lab Chip* **2008**, *8*, 68–74.

(108) Rajaraman, S.; Choi, S. O.; Shafer, R. H.; Ross, J. D.; Vukasinovic, J.; Choi, Y.; DeWeerth, S. P.; Glezer, A.; Allen, M. G. *J. Micromechanics Microengineering* **2007**, *17*, 163–171.

(109) Ellison, D.; Munden, A.; Levchenko, A. *Mol. Biosyst.* **2009**, *5*, 1004–1012.

(110) Hemmingsen, M.; Vedel, S.; Skafte-Pedersen, P.; Sabourin, D.; Collas, P.; Bruus, H.; Dufva, M. *PLoS One* **2013**, *8*, 14.

(111) Khetani, S. R.; Bhatia, S. N. *Curr. Opin. Biotechnol.* **2006**, *17*, 524–531.

(112) Trkov, S.; Eng, G.; Di Liddo, R.; Parnigotto, P. P.; Vunjak-Novakovic, G. *J. Tissue Eng. Regen. Med.* **2010**, *4*, 205–215.

(113) Zhong, W. L.; Tian, K.; Zheng, X. F.; Li, L. N.; Zhang, W. G.; Wang, S. Y.; Qin, J. H. *Stem Cells Dev.* **2013**, *22*, 2083–2093.

(114) Huang, C. P.; Lu, J.; Seon, H.; Lee, A. P.; Flanagan, L. A.; Kim, H.-Y.; Putnam, A. J.; Jeon, N. L. *Lab Chip* **2009**, *9*, 1740–1748.

(115) King, K. R.; Wang, S. H.; Irimia, D.; Jayaraman, A.; Toner, M.; Yarmush, M. L. *Lab Chip* **2007**, *7*, 77–85.

(116) Huang, N. F.; Dewi, R. E.; Okogbaa, J.; Lee, J. C.; JalilRufaihah, A.; Heilshorn, S. C.; Cooke, J. P. *Am. J. Transl. Res.* **2013**, *5*, 510–U96.

(117) Shamloo, A.; Manchandia, M.; Ferreira, M.; Mani, M.; Nguyen, C.; Jahn, T.; Weinberg, K.; Heilshorn, S. *Integr. Biol.* **2013**, *5*, 1076–1085.

(118) Chung, C.; Pruitt, B. L.; Heilshorn, S. C. *Biomater. Sci.* **2013**, *1*, 1082–1090.

(119) Keenan, T. M.; Grinager, J. R.; Procak, A. A.; Svendsen, C. N. *Integr. Biol.* **2012**, *4*, 1522–1531.

(120) Wang, J. Y.; Ren, L.; Li, L.; Liu, W. M.; Zhou, J.; Yu, W. H.; Tong, D. W.; Chen, S. L. *Lab Chip* **2009**, *9*, 644–652.

(121) Blagovic, K.; Kim, L. L. Y.; Voldman, J. *PLoS One* **2011**, *6*, 11.

(122) Lanfer, B.; Hermann, A.; Kirsch, M.; Freudenberg, U.; Reuner, U.; Werner, C.; Storch, A. *Tissue Eng. Part A* **2010**, *16*, 1103–1113.

(123) Chang, Y. J.; Tsai, C. J.; Tseng, F. G.; Chen, T. J.; Wang, T. W. *Nanomedicine-Nanotechnology Biol. Med.* **2013**, *9*, 345–355.

(124) Jin, K. L.; Peel, A. L.; Mao, X. O.; Xie, L.; Cottrell, B. A.; Henshall, D. C.; Greenberg, D. A. *Proc. Natl. Acad. Sci. U. S. A.* **2004**, *101*, 343–347.

(125) Liu, J. L.; Solway, K.; Messing, R. O.; Sharp, F. R. *J. Neurosci.* **1998**, *18*, 7768–7778.

(126) Zhang, R. L.; Zhang, Z. G.; Zhang, L.; Chopp, M. *Neuroscience* **2001**, *105*, 33–41.

(127) Horie, N.; So, K.; Moriya, T.; Kitagawa, N.; Tsutsumi, K.; Nagata, I.; Shinohara, K. *Cell. Mol. Neurobiol.* **2008**, *28*, 833–845.

(128) Iwai, M.; Sato, K.; Omori, N.; Nagano, I.; Manabe, Y.; Shoji, M.; Abe, K. *J. Cereb. Blood Flow Metab.* **2002**, *22*, 411–419.

(129) Sun, J. Q.; Zhou, W. H.; Sha, B.; Yang, Y. *Brain Dev.* **2010**, *32*, 191–200.

(130) Kim, S. J.; Son, T. G.; Kim, K.; Park, H. R.; Mattson, M. P.; Lee, J. *Neurochem. Res.* **2007**, *32*, 1399–1406.

(131) Li, M.; Tsang, K. S.; Choi, S. T.; Li, K.; Shaw, P. C.; Lau, K. F. *Chembiochem* **2011**, *12*, 449–456.

(132) Lu, W.; Wang, J.; Wen, T. Q. *Mol. Cell. Biochem.* **2008**, *311*, 233–240.

(133) Obi, S.; Yamamoto, K.; Shimizu, N.; Kumagaya, S.; Masumura, T.; Sokabe, T.; Asahara, T.; Ando, J. *J. Appl. Physiol.* **2009**, *106*, 203–211.

(134) Wang, H.; Riha, G. M.; Yan, S. Y.; Li, M.; Chai, H.; Yang, H.; Yao, Q. Z.; Chen, C. Y. *Arterioscler. Thromb. Vasc. Biol.* **2005**, *25*, 1817–1823.

(135) Yamamoto, K.; Sokabe, T.; Watabe, T.; Miyazono, K.; Yamashita, J. K.; Obi, S.; Ohura, N.; Matsushita, A.; Kamiya, A.; Ando, J. *Am. J. Physiol. Circ. Physiol.* **2005**, *288*, H1915–H1924.

(136) Wang, H.; Li, M.; Lin, P. H.; Yao, Q.; Chen, C. *J. Surg. Res.* **2008**, *150*, 266–270.

(137) Bai, K.; Huang, Y.; Jia, X.; Fan, Y.; Wang, W. *J. Biomech.* **2010**, *43*, 1176–1181.

(138) S. Higgins, J. L., and J. L. In *Biomedical Engineering Conference*; 2011.

(139) Bechara, S.; Wadman, L.; Popat, K. C. *Acta Biomater.* **2011**, *7*, 2892–2901.

(140) Lundqvist, J.; El Andaloussi-Lilja, J.; Svensson, C.; Dorfh, H. G.; Forsby, A. *Toxicol. Vitr.* **2013**, *27*, 1565–1569.

(141) Oh, J. E.; Bae, G. U.; Yang, Y. J.; Yi, M. J.; Lee, H. J.; Kim, B. G.; Krauss, R. S.; Kang, J. S. *Faseb J.* **2009**, *23*, 2088–2099.

(142) Qazi, H.; Shi, Z. D.; Tarbell, J. M. *PLoS One* **2011**, *6*, 13.

(143) Kurbel, S. *Med. Hypotheses* **2005**, *64*, 375–379.

(144) Deguchi, Y.; Inabe, K.; Tomiyasu, K.; Nozawa, K.; Yamada, S.; Kimura, R. *Pharm. Res.* **1995**, *12*, 1838–1844.

(145) Curtis, A. S. G.; Forrester, J. V; McInnes, C.; Lawrie, F. *J. Cell Biol.* **1983**, *97*, 1500–1506.

(146) Lee, J. N.; Jiang, X.; Ryan, D.; Whitesides, G. M. *Langmuir* **2004**, *20*, 11684–11691.

(147) Millet, L. J.; Stewart, M. E.; Sweedler, J. V; Nuzzo, R. G.; Gillette, M. U. *Lab Chip* **2007**, *7*, 987–994.

(148) Basser, P. J. *Microvasc. Res.* **1992**, *44*, 143–165.

(149) Abbott, N. J. *Neurochem. Int.* **2004**, *45*, 545–552.

(150) Geer, C. P.; Grossman, S. A. *J. Neurooncol.* **1997**, *32*, 193–201.

(151) Sharma, R.; Ottenhof, T.; Rzeczkowska, P. A.; Niles, L. P. *J. Pineal Res.* **2008**, *45*, 277–284.

(152) Pineda, J. R.; Rubio, N.; Akerud, P.; Urban, N.; Badimon, L.; Arenas, E.; Alberch, J.; Blanco, J.; Canals, J. M. *Gene Ther.* **2007**, *14*, 118–128.

(153) Kitchens, D. L.; Snyder, E. Y.; Gottlieb, D. I. *J. Neurobiol.* **1994**, *25*, 797–807.

(154) Garcez, R. C.; Teixeira, B. L.; Schmitt, S. D.; Alvarez-Silva, M.; Trentin, A. G. *Cell. Mol. Neurobiol.* **2009**, *29*, 1087–1091.

(155) Schwindt, T. T.; Motta, F. L.; Barnabe, G. F.; Massant, C. G.; Guimaraes, A. O.; Calcagnotto, M. E.; Pesquero, J. B.; Mello, L. E. *An. Acad. Bras. Cienc.* **2009**, *81*, 443–452.

(156) Trinh, N. T. N.; Prive, A.; Kheir, L.; Bourret, J. C.; Hijazi, T.; Amraei, M. G.; Noel, J.; Brochiero, E. *Am. J. Physiol. Cell. Mol. Physiol.* **2007**, *293*, L870–L882.

(157) Masui, H.; Castro, L.; Mendelsohn, J. *J. Cell Biol.* **1993**, *120*, 85–93.

(158) Zhao, C. M.; Deng, W.; Gage, F. H. *Cell* **2008**, *132*, 645–660.

(159) Schmetsdorf, S.; Gartner, U.; Arendt, T. *Int. J. Dev. Neurosci.* **2005**, *23*, 101–112.

(160) Yang, Y.; Herrup, K. *Biochim. Biophys. Acta-Molecular Basis Dis.* **2007**, *1772*, 457–466.

(161) Abrous, D. N.; Koehl, M.; Le Moal, M. *Physiol. Rev.* **2005**, *85*, 523–569.

(162) Alvarez-Buylla, A.; Garcia-Verdugo, J. M.; Tramontin, A. D. *Nat. Rev. Neurosci.* **2001**, *2*, 287–293.

(163) Deckwerth, T. L.; Johnson, E. M. *J. Cell Biol.* **1993**, *123*, 1207–1222.

(164) Dirnagl, U.; Iadecola, C.; Moskowitz, M. A. *Trends Neurosci.* **1999**, *22*, 391–397.

(165) Dugan, L. L.; Turetsky, D. M.; Du, C.; Lobner, D.; Wheeler, M.; Almli, C. R.; Shen, C. K. F.; Luh, T. Y.; Choi, D. W.; Lin, T. S. *Proc. Natl. Acad. Sci. U. S. A.* **1997**, *94*, 9434–9439.

(166) Liu, X. Z.; Xu, X. M.; Hu, R.; Du, C.; Zhang, S. X.; McDonald, J. W.; Dong, H. X.; Wu, Y. J.; Fan, G. S.; Jacquin, M. F.; Hsu, C. Y.; Choi, D. W. *J. Neurosci.* **1997**, *17*, 5395–5406.

(167) Yu, Z. F.; Luo, H.; Fu, W. M.; Mattson, M. P. *Exp. Neurol.* **1999**, *155*, 302–314.

(168) Loo, D. T.; Copani, A.; Pike, C. J.; Whittemore, E. R.; Walencewicz, A. J.; Cotman, C. W. *Proc. Natl. Acad. Sci. U. S. A.* **1993**, *90*, 7951–7955.

(169) Raff, M. C.; Barres, B. A.; Burne, J. F.; Coles, H. S.; Ishizaki, Y.; Jacobson, M. D. *Science (80-.).* **1993**, *262*, 695–700.

(170) Xia, Z. G.; Dickens, M.; Raingeaud, J.; Davis, R. J.; Greenberg, M. E. *Science (80-.).* **1995**, *270*, 1326–1331.

(171) Yao, R. J.; Cooper, G. M. *Science (80-.).* **1995**, *267*, 2003–2006.

(172) Yuan, J. Y.; Yankner, B. A. *Nature* **2000**, *407*, 802–809.

(173) Colleen T. Curley1 and Sabrina S. Jedlicka, K. F. *Mater. Res. Soc. Symp. Proc.* **2012**, *1498*.

(174) King, J. A.; Miller, W. M. *Curr. Opin. Chem. Biol.* **2007**, *11*, 394–398.

(175) Fan, Y. W.; Cui, F. Z.; Hou, S. P.; Xu, Q. Y.; Chen, L. N.; Lee, I. S. *J. Neurosci. Methods* **2002**, *120*, 17–23.

(176) Henley, J.; Poo, M. *Trends Cell Biol.* **2004**, *14*, 320–330.

(177) Tang, F. J.; Kalil, K. *J. Neurosci.* **2005**, *25*, 6702–6715.

(178) Yang, Y.; Ren, W. W.; Chen, F. X. *Neuroreport* **2006**, *17*, 235–238.

(179) Pearce, T. M.; Wilson, J. A.; Oakes, S. G.; Chiu, S. Y.; Williams, J. C. *Lab Chip* **2005**, *5*, 97–101.

(180) Cullen, D. K.; Vukasinovic, J.; Glezer, A.; LaPlaca, M. C. *J. Neural Eng.* **2007**, *4*, 159–172.

(181) Culican, S. M.; Baumrind, N. L.; Yamamoto, M.; Pearlman, A. L. *J. Neurosci.* **1990**, *10*, 684–692.

(182) Gierdalski, M.; Juliano, S. L. *Cereb. Cortex* **2003**, *13*, 572–579.

(183) Fanarraga, M. L.; Avila, J.; Zabala, J. C. *Eur. J. Neurosci.* **1999**, *11*, 517–527.

(184) Katsetos, C. D.; Nakahara, C.; Agamanolis, D. P.; Karkavelas, G.; Lebenthal, E.; Frankfurter, A. *Arch. Pathol. Lab. Med.* **1994**, *118*, 1002–1006.

(185) Roskams, A. J. I.; Cai, X.; Ronnett, G. V. *Neuroscience* **1998**, *83*, 191–200.

(186) Bain, G.; Kitchens, D.; Yao, M.; Huettner, J. E.; Gottlieb, D. I. *Dev. Biol.* **1995**, *168*, 342–357.

(187) Ginis, I.; Luo, Y. Q.; Miura, T.; Thies, S.; Brandenberger, R.; Gerecht-Nir, S.; Amit, M.; Hoke, A.; Carpenter, M. K.; Itskovitz-Eldor, J.; Rao, M. S. *Dev. Biol.* **2004**, *269*, 360–380.

(188) Roy, N. S.; Wang, S.; Jiang, L.; Kang, J.; Benraiss, A.; Harrison-Restelli, C.; Fraser, R. A. R.; Couldwell, W. T.; Kawaguchi, A.; Okano, H.; Nedergaard, M.; Goldman, S. A. *Nat. Med.* **2000**, *6*, 271–277.

(189) Anton, E. S.; Marchionni, M. A.; Lee, K. F.; Rakic, P. *Development* **1997**, *124*, 3501–3510.

(190) Diers-Fenger, M.; Kirchhoff, F.; Kettenmann, H.; Levine, J. M.; Trotter, J. *Glia* **2001**, *34*, 213–228.

(191) Bultje, R. S.; Castaneda-Castellanos, D. R.; Jan, L. Y.; Jan, Y. N.; Kriegstein, A. R.; Shi, S. H. *Neuron* **2009**, *63*, 189–202.

(192) Sevc, J.; Daxnerova, Z.; Miklosova, M. *Cell. Mol. Neurobiol.* **2009**, *29*, 927–936.

(193) Zhang, Y.; Niu, B. H.; Yu, D. M.; Cheng, X. S.; Liu, B.; Deng, J. B. *Brain Struct. Funct.* **2010**, *215*, 115–122.

(194) Sato, K.; Hibara, A.; Tokeshi, M.; Hisamoto, H.; Kitamori, T. *Adv. Drug Deliv. Rev.* **2003**, *55*, 379–391.

(195) Mehta, G.; Mehta, K.; Sud, D.; Song, J. W.; Bersano-Begey, T.; Futai, N.; Heo, Y. S.; Mycek, M. A.; Linderman, J. J.; Takayama, S. *Biomed. Microdevices* **2007**, *9*, 123–134.

(196) Bange, A.; Halsall, H. B.; Heineman, W. R. *Biosens. Bioelectron.* **2005**, *20*, 2488–2503.

(197) Kusnezow, W.; Syagailo, Y. V; Goychuk, I.; Hoheisel, J. D.; Wild, D. G. *Expert Rev. Mol. Diagn.* **2006**, *6*, 111–124.

(198) PORSTMANN, T.; KIESSIG, S. T. *J. Immunol. Methods* **1992**, *150*, 5–21.

(199) Lin, C.-C.; Wang, J.-H.; Wu, H.-W.; Lee, G.-B. *J. Assoc. Lab. Autom.* **2010**, *15*, 253–274.

(200) Brennan, D.; Justice, J.; Corbett, B.; McCarthy, T.; Galvin, P. *Anal. Bioanal. Chem.* **2009**, *395*, 621–636.

(201) Squires, T. M.; Messinger, R. J.; Manalis, S. R. *Nat. Biotechnol.* **2008**, *26*, 417–426.

(202) Yanik, A. A.; Huang, M.; Artar, A.; Chang, T.-Y.; Altug, H. *Appl. Phys. Lett.* **2010**, *96*.

(203) Hart, R.; Lec, R.; Noh, H. M. *SENSORS AND ACTUATORS B-CHEMICAL* **2010**, *147*, 366–375.

(204) Sigurdson, M.; Wang, D. Z.; Meinhart, C. D. *Lab Chip* **2005**, *5*, 1366–1373.

(205) Kozuka, T.; Tuziuti, T.; Mitome, H.; Fukuda, T. *JAPANESE J. Appl. Phys. PART 1-REGULAR Pap. SHORT NOTES Rev. Pap.* **1998**, *37*, 2974–2978.

(206) Jonas, A.; Zemanek, P. *Electrophoresis* **2008**, *29*, 4813–4851.

(207) Hu, Y.; Cheng, X.; Ou-Yang, H. D. *Biomed. Opt. Express* **2013**, *4*, 1646–1653.

(208) Duhr, S.; Braun, D. *Proc. Natl. Acad. Sci. U. S. A.* **2006**, *103*, 19678–19682.

(209) Duhr, S.; Braun, D. *Phys. Rev. Lett.* **2006**, *96*.

(210) Braun, D.; Libchaber, A. *Phys. Rev. Lett.* **2002**, *89*.

(211) Baaske, P.; Weinert, F. M.; Duhr, S.; Lemke, K. H.; Russell, M. J.; Braun, D. *Proc. Natl. Acad. Sci. U. S. A.* **2007**, *104*, 9346–9351.

(212) Gaffarogullari, E. C.; Krause, A.; Balbo, J.; Herten, D.-P.; Jaeschke, A. *RNA Biol.* **2013**, *10*, 1815–1821.

(213) Wienken, C. J.; Baaske, P.; Rothbauer, U.; Braun, D.; Duhr, S. *Nat. Commun.* **2010**, *1*.

(214) Mao, H. B.; Yang, T. L.; Cremer, P. S. *J. Am. Chem. Soc.* **2002**, *124*, 4432–4435.

(215) Guijt, R. M.; Dodge, A.; van Dedem, G. W. K.; de Rooij, N. F.; Verpoorte, E. *Lab Chip* **2003**, *3*, 1–4.

(216) Miralles, V.; Huerre, A.; Malloggi, F.; Jullien, M.-C. *Diagnostics* **2013**, *3*, 33–67.

(217) Vigolo, D.; Rusconi, R.; Piazza, R.; Stone, H. A. *Lab Chip* **2010**, *10*, 795–798.

(218) Sato, K.; Sawayanagi, M.; Hosokawa, K.; Maeda, M. *Anal. Sci.* **2004**, *20*, 893–894.

(219) Zhong, W. *Anal. Bioanal. Chem.* **2009**, *394*, 47–59.

(220) Wayment, J. R.; Harris, J. M. *Anal. Chem.* **2009**, *81*, 336–342.

(221) Jhon J. Figueroa. *Grad. Theses Diss.* **2013**.

(222) Zhao, C.; Fu, J.; Oztekin, A.; Cheng, X. *J. NANOPARTICLE Res.* **2014**, *16*.

(223) Wang, L. Y.; Kan, X. W.; Zhang, M. C.; Zhu, C. Q.; Wang, L. *Analyst* **2002**, *127*, 1531–1534.

(224) Jiang, Z. L.; Yuan, W. E.; Pan, H. C. *Spectrochim. ACTA PART A-MOLECULAR Biomol. Spectrosc.* **2005**, *61*, 2488–2494.

(225) Wang, H.; Li, Y.; Slavik, M. *J. RAPID METHODS Autom. Microbiol.* **2007**, *15*, 67–76.

(226) Sheehan, P. E.; Whitman, L. J. *NANO Lett.* **2005**, *5*, 803–807.

Bu Wang

530 Montclair Ave, Bethlehem, PA 18015 | 1-610-844-6656 | buw007@gmail.com

RESEARCH INTEREST

- Biomedical microfluidic system design, modeling, optimization, fabrication and performance evaluation (bioaffinity assays, FACS, biomarker identification and surface characterization).
- POC (point of care) diagnostics, stem cell research and multifunction microfluidic system integration.

EDUCATION

PhD in Materials Science and Engineering
Lehigh University, Bethlehem, PA, USA
Bachelor of Science in Chemistry
Nankai University, Tianjin, China
Honors Student Exchange Program
National University of Singapore, Singapore

PUBLICATIONS

1. **Bu Wang**, Alex L. Weldon, Pisist Kumnorkaew, Bu Xu, James F. Gilchrist, and Xuanhong Cheng. Effect of Surface Nanotopography on Immunoaffinity Cell Capture in Microfluidic Devices. Langmuir, 2011, 27 (17), pp 11229–11237
2. **Bu Wang**, Sabrina Jedlicka, and Xuanhong Cheng. Maintenance and Neuronal Cell Differentiation of Neural Stem Cells C17.2 Correlated to Medium Availability Sets Design Criteria in Microfluidic Systems. PLoS One, October 13, 2014. DOI: 10.1371/journal.pone.0109815
3. Alaxander L. Weldon, Pisist Kumnorkaew, **Bu Wang**, Xuanhong Cheng, and James F. Gilchrist. Fabrication of Macroporous Polymeric Membranes through Binary Convective Deposition. ACS Appl. Mater. Interfaces, 2012, 4 (9), pp 4532–4540

AWARDS/RECOGNITIONS

Libsch Research Award | Lehigh University
CMMI Engineering Research and Innovation Student Fellowship | National Science Foundation
Honorary Scholarship for Talented Students | Ministry of Education of China